STOCLER

DOE/ER-0046/23

Damage Analysis and Fundamental Studies

Quarterly Progress Report
July-September 1985

November 1985

U.S. Department of Energy
Office of Energy Research
Office of Fusion Energy
Washington, DC 20545

B&R NO. AT-1502-03-04

Hanford Engineering Development Laboratory

Operated by
Westinghouse
Hanford Company
for the U.S. DOE

A Subsidiary of
Westinghouse Electric
Corporation

Contract No.
DE-AC06-76FF02170

P.O. Box 1970
Richland, WA 99352

DISCLAIMER

Printed in the United States of America
Available from
U.S. Department of Commerce
National Technical Information Service
5285 Port Royal Road
Springfield, VA 22161

NTIS price codes
Printed copy: A05
Microfiched copy: A01

DOE/ER-0046/23
uc-20-2oc

Damage Analysis and Fundamental Studies

Quarterly Progress Report
July-September 1985

November 1985

U.S. Department of Energy
Office of Energy Research
Office of Fusion Energy
Washington, DC 20545

B&R No. AT-15-02-03-04

FOREWORD

This report is the thirty-first in a series of Quarterly Technical Progress Reports on ***Damage Analysis and Fundamental Studies*** (DAFS), which is one element of the Fusion Reactor Materials Program, conducted in support of the Magnetic Fusion Energy Program of the U.S. Department of Energy (DOE). The first eight reports in this series were numbered DOE/ET-0065/1 through 8. Other elements of the Fusion Materials Program are:

- Alloy Development for Irradiation Performance (ADIP)
- Plasma-Materials Interaction (PMI)
- Special Purpose Materials (SPM).

The DAFS program element is a national effort composed of contributions from a number of National Laboratories and other government laboratories, universities, and industrial laboratories. It was organized by the Materials and Radiation Effects Branch, DOE/Office of Fusion Energy, and a Task Group on ***Damage Analysis and Fundamental Studies,*** which operates under the auspices of that branch. The purpose of this series of reports is to provide a working technical record of that effort for the use of the program participants, the fusion energy program in general, and the DOE.

This report is organized along topical lines in parallel to a Program Plan of the same title so that activities and accomplishments may be followed readily, relative to that Program Plan. Thus, the work of a given laboratory may appear throughout the report. A chapter has been added on Reduced Activation Materials to accommodate work on a topic not included in the early program plan. The Contents is annotated for the convenience of the reader.

This report has been compiled and edited by N. E. Kenny under the guidance of the Chairman of the Task Group on ***Damage Analysis and Fundamental Studies,*** D. G. Doran, Hanford Engineering Development Laboratory (HEDL). Their efforts, those of the supporting staff of HEDL, and the many persons who made technical contributions are gratefully acknowledged. T. C. Reuther, Fusion Technologies Branch, is the DOE counterpart to the Task Group Chairman and has responsibility for the DAFS program within DOE.

G. M. Haas, Chief
Fusion Technologies Branch
Office of Fusion Energy

CONTENTS

CHAPTER 1

IRRADIATION TEST FACILITIES

RTNS-II IRRADIATIONS AND OPERATIONS

D. W. Short and D. W. Heikkinen
Lawrence Livermore National Laboratory

1.0 Objective

The objectives of this work are operation of RTNS-II (a 14-MeV neutron source facility), machine development, and support of the experimental program that utilizes this facility. Experimenter services include dosimetry, handling, scheduling, coordination, and reporting. RTNS-II is supported jointly by the U.S. and Japan and is dedicated to materials research for the fusion power program. Its primary use is to aid in the development of models of high-energy neutron effects. Such models are needed in interpreting and projecting to the fusion environment, engineering data obtained in other spectra.

2.0 Summary

Irradiations were performed on 7 different experiments during this quarter. Japanese furnace was installed in the right target roan. Terminal turbo's were reworked. Terminal water flow panel was upgraded. Suction hood was installed in the right target room to reduce tritium gas quantity during target removal. Target removal procedures were also changed to reduce exposure time to personnel. Ion source development continues.

3.0 Program

Title: RTNS-II operations (WZJ-16)
Principal Investigator: D. W. Short
Affiliation: Lawrence Livermore National Laboratory

4.0 Relevant DAFS Program Plan Task/Subtask

TASK II,A,2,3,4,
TASK II,B,3,4
TASK II,C,1,2,6,11,18,

5.0 Irradiation

During this quarter, irradiations (both dedicated and add-on) were done for the following people.

Experimenter	P or A*	Sample Irradiated
D. Heikkinen (LLNL)	A	Nb -dosimetry calibration
H. Heinisch (HEDL) G. Pells (Harwell) F. Clinard (LANL) M. Kiritani (Hokkaido) R. Ohshima (Osaka) H. Yoshida (Kyoto) K. Abe (Tohoku) H. Matsui (Tohoku) H. Kayano (Tohoku)	P	Metals - displacement damage & mechanical properties. Ceramics - neutron damage - irradiated at 90°C and 290°C

Experimenter	P or A*	Sample Irradiated
HEDL (Cont'd)		
H. Kawanishi (Tokyo) N. Igata (Tokyo) Y. Shimomura (Hiroshima) N. Yoshida (Kyushu)		
A. Kohyama (Tokyo) S. Nanao (Tokyo) H. Kawanishi (Tokyo) K. Miyahara (Tokyo) M. Kiritani (Hokkaido) H. Takahashi (Hokkaido) K. Abe (Tohoku) Y. Higasiguchi (Tohoku) H. Kayano (Tohoku) K. Okamura (Tohoku) H. Matsui (Tohoku) M. Hasegawa (Tohoku) K. Ono (Hiroshima) N. Yoshida (Kyushu)	P	**Metals** - displacement damage & mechanical properties. Ceramics - neutron damage - irradiated at roan temperature.
K. Kawamura	A	$Pd_{80}Si_{20}$ - Property change
M. Kiritani/T. Yoshiie (Hokkaido)	P	Ni, Au, Ag, Cu & Fe - **cascade** damage
S. Iwasaki (Tohoku)	A	$^{27}Al(n,2n)$ - cross section
S. Iwasaki (Tohoku)	A	SS & Ni alloy - tensile

* P = primary, A = add-on

5.1 RTNS-II Status - W. Short and D. W. Heikkinen

Diode string repaired on the left mchine.

Terminal turbo pump replaced on the left mchine.

Ion source development continues.

Japanese furnace installed in the right target roan.

Terminal water flow panel changed on the right machine.

Suction hood installed in right target roan.

6.0 Future Work

Irradiations will be continued for D. Heikkinen (LLNL), H. Heinisch et al., S. Iwasaki (Tohoku), A. Kohyama et al., M. Kiritani/T. Yoshiie (Hokkaido). Also during this period, irradiations for M. Kiritani (Hokkaido, T. Yoshiie (Hokkaido) and H. Kawanishi (Tokyo) et al., will be initiated.

CHAPTER 2

DOSIMETRY AND DAMAGE PARAMETERS

DOSIMETRY MEASUREMENTS FOR THE ORR 6J PROTOTYPE EXPERIMENT

L. R. G r e e d (Argonne National Laboratory)

1.0 Objective

To characterize neutron irradiation experiments in terms of neutron fluence, spectra, and damage parameters (dpa, gas production, transmutation).

2.0 Summary

Results are reported for a test of the 6J Japanese experiment in the oak Ridge Research Reactor. Maximum fast fluxes above 0.1 MeV were 2.0×10^{14} n/cm^2-s producing about 4.5 dpa per year in 316 stainless steel.

The status of all dosimetry experiments is summarized in Table 1.

Table 1. Status of Dosimetry Experiments

Facility/Experiment		Status/Comments
ORR	- MFE 1	completed 12/79
	- MFE 2	Completed 06/81
	- MFE 4A1	Completed 12/81
	- MFE 4A2	Completed 11/82
	- MFE 4B	completed 04/84
	- TBC 07	Completed 07/80
	- THIO-Test	Completed 07/82
	- THIO-1	completed 12/83
	- HP Test	Completed 03/84
	- J6 Test	Completed 07/85
	- J6, 57	Irradiations In Progress
HFIR	- CTR 32	completed 04/82
	- CTR 31, 34, 35	completed 04/83
	- T2, RB1	completed 09/83
	- T1, CTR 39	completed 01/84
	- CTR 40-45	completed 09/84
	- CTR 30, 36, 46	Completed 03/85
	- RB2	completed 06/85
	- CTR 47-56	Irradiations in Progress
	- JP I	Samples received 06/85
	- JP 2-8	Irradiations In Progress
	- BE Test	Completed 09/85
Omega West	- spectral Analysis	completed 10/80
	- HEDL1	completed 05/81
	- HEDL2	Samples sent 04/85
	- LANL 1	Completed 08/84
EBR II	- X287	Completed 09/81
IYNS	- Spectral Analysis	Completed 01/82
	- LANL 1 (Hurley)	completed 06/82
	- Hurley	completed 02/83
	- Coltman	Completed 08/83

3.0 Program

Title: Dosimetry and Damage Analysis
Principal Investigator: L. R. G r e e d
Affiliation, Argonne National Laboratory

4.0 Relevant DAFS Program Plan Task/Subtask

Task II.A.l Fission Reactor Dosimetry

5.0 Accomplishments and status

Analysis has been completed for the prototype 6J Japanese experiment in the Oak Ridge Research Reactor. The experiment was conducted in the C7 position from September 6, 1984 to January 21, 1985 for a net exposure of 82,096 MWH. The experiment contained specimens at two different temperatures, 60°C and 200°C and four dosimetry tubes were located in each temperature region. These two temperature regions were concentric. the 200°C being on the inside of the 60°C region and the regions extended from about 2.4 cm above midplane to -17.9 cm below midplane.

Each dosimetry tube contained four wires of 0.1%Co-Al, Fe, Ti, and Ni. Each wire was segmented into eight 1" pieces for gamma counting. Selected vertical gradients are shown in Pig. 1. All of the vertical gradients were fit by a simple polynomial function,

$$F(z) = a(1 + bz + cz^2) \qquad (1)$$

where a is the midplane value and e is the height above midplane (in centimeters). The b and c coefficients were determined by least-squares analysis. All of the data is well-described by eq. (1) using $b = -8.31 \times 10^{-3}$ and $c = -8.85 \times 10^{-4}$. There may be a small difference between the thermal and fast vertical flux gradients; however, this effect is at most only a few percent and no significant spectral difference is indicated.

The maximum flux position was determined to be at -4.7 cm below mid-plane. The activity rates at this location are listed in Table 2. These rates were then used as input to the STAY'SL computer code to adjust the neutron flux spectrum at each location. These adjusted fluxes are listed in Table 3. Flux gradients can be determined using the data in Table 1-3 and Equation (1); however, we should note that since the maximum flux position is at -4.7 cm below midplane. the "a" terms in Equation (1) are actually 21 less than the values listed in Tables 2 or 3.

The horizontal flux gradients are in all cases less than 20%. The fast flux gradients are less than 141; however, there is a drop in thermal flux of about 10-20% between the two different temperature regions presumably due to absorption in the extra material. If we consider the two temperature regions separately. then the horizontal flux gradients are only about 10% in each region. In all cases the flux is higher in the north and east sides and lowest on the west side.

Damage and gas production rates were computed using the SPECTER computer code. Results are listed for the highest flux position (east side, 60°C, -4.7 cm below midplane) in Table 4. These values correspond to a total fluence of 5.88×10^{21} n/cm^2 and 1.99×10^{21} n/cm^2 above 0.1 MeV. Since most of the damage terms are linear with the fluence, damage rates at any other location can be determined by scaling with the fast fluence (>.1 MeV) in Table 3 followed by the use of Equation (1). In any case, the results would be within about 301 of the values in Table 4. The only emption to this is for the thermal helium production in nickel which roughly scales with the square of the thermal fluence.

similar dosimetry experiments are nor) in progress for the 56 and 57 irradiations in ORR. Samples are nor) being analyzed for the JPl irradiation in WIR.

Table 2. Maximum Activation Rate for ORR-6J-Test

values at -4.7 cm below midplane normalized to 30 MW; data corrected for burnup; accuracy ±2%

Wire #	Location	Temp., °C	Activation Rate (atom/atom-s) $^{59}Co(n,\gamma)^{60}Co$ *10^{-9}	$^{58}Fe(n,\gamma)^{59}Fe$ *10^{-10}	$^{54}Fe(n,p)^{54}Mn$ *10^{-11}	$^{46}Ti(n,p)^{46}Sc$ *10^{-12}
1	E	60°	6.84	1.98	1.20	1.57
2	N	60°	6.78	1.90	1.26	1.67
3	N	60°	6.31	1.73	1.14	1.47
4	S	60°	6.72	1.88	1.17	1.50
5	N	200°	5.65	1.63	1.14	1.46
6	S	200°	5.86	1.69	1.13	1.46
7	E	200°	5.69	1.72	1.18	1.55
8	N	200°	5.72	1.65	1.21	1.55

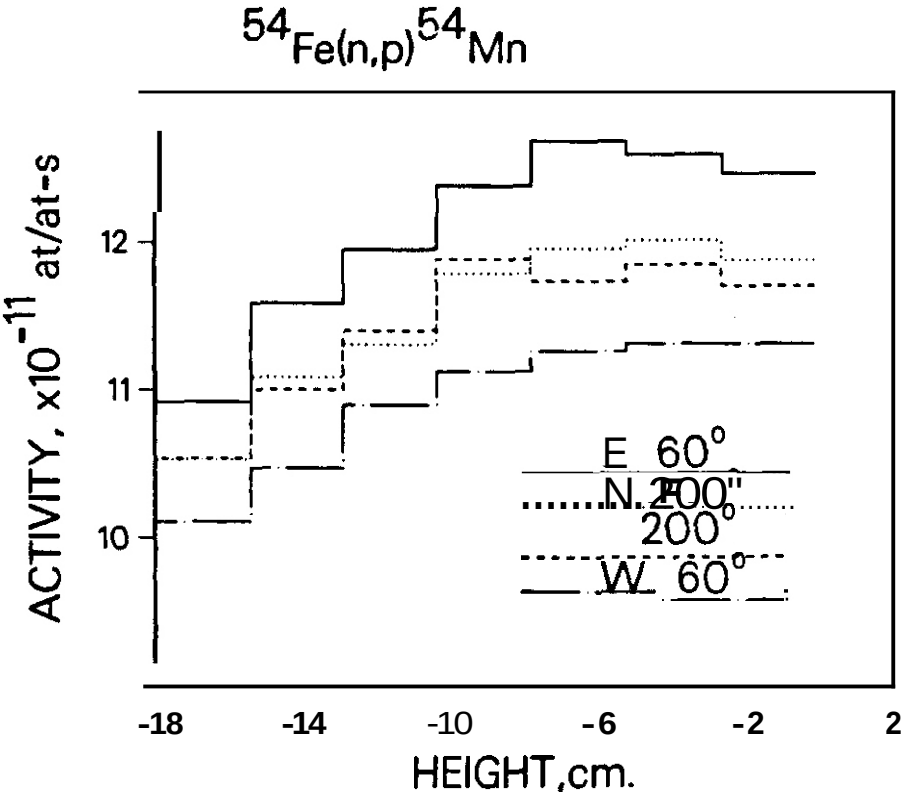

Fig. 1. vertical Activity Gradients Measured for the $^{54}Fe(n,p)^{54}Mn$ Reaction Indicative of the Fast Neutron F l u (>0.1 MeV). Gradients at all Other Locations Pall within the Range of Data Displayed.

Table 3. Flux Values for ORR-6J-Test

values at maximum, 5 cm below midplane;
accuracy ±10%

			Flux, x10^{14} n/cm^2-s		
Wire #	Location	Temp, °C	Thermal[a]	>0.1 MeV	Total
1	E	60	2.01	1.99	5.97
2	N	60	1.97	2.03	5.99
3	W	60	1.82	1.85	5.49
4	S	60	1.95	1.93	5.80
5	W	200	1.65	1.79	5.14
6	S	200	1.71	1.80	5.26
7	E	200	1.60	1.85	5.27
8	N	200	1.66	1.86	5.27

[a]Thermal flux <.5 eV for maxwellian at 95°C.

Table 4. Damage Parameters for ORR-6J-Test

Maximum values at east side, 60°C, 4.7 cm below midplane. Other locations scale with fast flux in Table 1-3 and Eq. (1). Values correspond to a fast fluence of 1.99×10^{21} n/cm^2.

Element		DPA	He, appm,
Al		2.68	1.22
Ti		1.71	0.92
V		1.90	0.044
Cr		1.70	0.30
Mn		1.82	0.25
Pe		1.51	0.52
Co		1.74	0.25
	Fast	1.59	7.34
Ni	Thermal	.10	56.03
	Total	1.69	63.37
Cu		1.46	0.45
Nb		1.45	0.097
Mo		1.07	-
316 SS[a]		1.56	8.63

[a]316 SS: Fe(.645), Ni(.13), Cr(.18), Mn(.019), Mo(.026)

6.0 References

None

7.0 Future Work

The J6 and J7 experiments are now being irradiated in ORR.

HAFNIUM SHIELDING TESTS IN HFIR-RB POSITIONS AND REANALYSIS OF THE HFIR-RB1, -RB2 EXPERIMENT!

I,. R. Greenwood (Argonne National Laboratory)

1.0 Objective

To characterize neutron irradiation experiments in terms of neutron fluence, spectra, and damage parameters.

2.0 Summary

Analysis has been completed tor the hafnium shield tests in the removable beryllium positions of the High Flux Isotopes Reactor (ORNL). The shield reduces the thermal flux by 90%, the epithermal flux by 50%, and the fast flux by only 5%. Yearly helium production in 316 stainless steel is thus reduced by a factor of 26 with little effect on displacement damage production. These new spectral analyses have been used to reanalyze previously reported results from the RB1 and RB2 materials irradiations in HFIR; the damage rates have been increased by 20-30%.

3. Program

Title: Dosimetry and Damage Analysis
Principal Investigator: L. R. Greenwood
Affiliation: Argonne National Laboratory

4.0 Relevant DAFS Program Plan Task/Subtask

Task II.A.1 Fission Reactor Dosimetry

5.0 Accomplishments and Status

Hafnium-shielding experiments have been completed in the removable beryllium (REI) positions in the High Flux Isotopes Reactor (HFIR) at ORNL. The purpose of these tests is to validate the design of a hafnium core piece for the REI positions. Hafnium is used to reduce the thermal/ epithermal flux ("spectrum tailoring") in order to reduce helium production in nickel-bearing materials (stainless Steel) during lengthy fusion materials irradiations. Without the hafnium, the helium-to-displacement ratio will surpass the fusion first-wall value within a year. Thus, the idea is to first irradiate without hafnium, building up the helium content, and then to switch to the hafnium liner so that more damage can be accumulated without excessive helium. Similar experiments have been successfully Conducted in the Oak Ridge Research Reactor.' Two fusion experiments (RB1 and RB2) have also been reported in HFIR.[1,2]

The experiments were conducted in several different RB positions both with and without hafnium liners on August 3, 1985 for I-hour at a reduced power level of 11 MW. Twelve different dosimetry materials were irradiated at six different vertical positions in each experimental assembly. These dosimeters were encapsulated in an aluminum tube measuring 1/8" OD by 21 7/8" in length. These tubes were inserted into the center of each hafnium and/or aluminum assembly which measured 1.24" OD. The reduced power level permitted us to use fissionable monitors and reduced the gamma heating. A full-parer (100 MW) test is now in progress for one reactor cycle (22 days).

Two separate 1-hour irradiations were conducted. First, only aluminum assemblies were irradiated at 10.8 MW in positions RB-1 and RB-5; then an aluminum assembly was irradiated at 11.0 MW in RE5 along with a hafnium assembly in position RB1. me first irradiation provided a normal baseline operating condition for HFIR, whereas the second allowed us to measure the hafnium effect and to observe any tilting of the flux gradients due to the presence of the hafnium. Unfortunately one of the dosimetry tubes was not fully inserted into the aluminum capsule (RB5), and hence, one of the two baseline runs was lost. However, there does not appear to be any significant difference between the two positions (RB1 and RB5) so that one baseline measurement is adequate for this comparison.

The measured activities are listed in Table 1. As can be seen, there are only small differences between the two aluminum capsules and all of the fast (threshold) reaction rates, as expected. The presence of the hafnium depresees the thermal/epithermal reactions by factors of 3-10, depending on the energy response of each reaction.

The measured reaction rates were used to adjust the neutron flux spectra at each location as calculated by R. Lillie (ORNL) using the least-squares adjustment code STAY'S L. uncertainties in the reaction rates are listed in Table 1, the neutron fluxes were assumed to have a uncertainty of 201, and cross-section variances are taken from ENDF/B-V. Gaussian covariances were assumed in all cases. The adjusted fluxes are listed in Table 2. In both cases the adjusted flux spectra agree rather well with the Calculations. Some caution is, however, required in the hafnium-shielded case since the calculated group structure was too coarse in the resonance region. For example, the 197 Au (n, y) resonance does not coincide with those in hafnium and thus, the resonance shielding is not very large for this reaction. unless finer group calculations are performed, very large errors will occur for this reaction. Consequently, some modifications were required in the input calculated spectrum to avoid these resonance pitfalls. However, these have no effect on the fast flux or dosage.

The bare and hafnium-shielded flux spectra are shown in Figure 1. The deep valleys centered around 1 eV and 300 eV are due to resonances in hafnium. The thermal flux is depressed about a factor of 8, while the fast flux is only depressed about 51. Comparison of the two aluminum irradiations (no hafnium) show that the fast flux agrees within 1.5: and that the thermal/epithermal flux differs by about 5:. This difference is presumably due to a slight tilting of the flux gradients due to the presence of hafnium. In other words, the reactor power must be slightly increased overall to compensate for the depression near the hafnium assembly in order to maintain a net power level of 100 MW. Vertical flux gradients were measured at all three RB positions at 6 different vertical heights. Selected results are shown in Figs. 2 and 3. In all cases the data can be described by a single polynomial as follows:

$$f(z) = a(1 + bz + cz^2) \qquad (1)$$

where E = height in cm, f is the value of the flux or damage rate at height z, and a is the midplane value (Table 2 or 3). The best fit to the bare (no-Hf) data gives $b = 1.975 \times 10^{-3}$ and $c = -1.083 \times 10^{-3}$ for the fast reactions and $b = -1.625 \times 10^{-3}$ and $c = -1.280 \times 10^{-3}$ for the theml reactions. In the hafnium case, the theml effect is quite striking and we can see in Fig. 2 that the flux rises near the end (~30 cm) as we emerge from the hafnium shield. For this case, the fitting procedure gives $b = 3.00 \times 10^{-4}$ and $c = -1.18 \times 10^{-3}$. A11 of these parameter sets are similar and the differences are negligible between -20 cm to +10 cm above midplane.

At larger distances there is clearly a spectral shift since the thermal flux falls more rapidly than the fast flux. At 20 cm above midplane the theml to fast ratio is about 30 lower than at midplane. Within the hafnium shield the theml vertical gradient is slightly shallower than without the shield; however, the fast flux gradient is about the same either way.

Damage and gas production rates were calculated with the SPECTER[3] computer code and the results are listed in Table 3. Both calculations are for position RB1 and the differences are mainly due to the difference in the fast flux of about 1.51. The calculations in Table 3 were done for a 1 year (365 FPD) irradiation. The hafnium shield reduces the helium production in stainless steel from 688 appm to 26.1 appm, a factor of about 26. Of Course. this is only valid for the above conditions and must be done for each case considering possible burnout of the hafnium as well. In any case, it is evident that the hafnium, indeed, reduces the thermal helium effect without sacrificing the fast damage production as desired.

5.1 Hf, RB Tests

5.2 Reanalysis of the HFIR-RB1, RB2 Experiments
L. R. Greenwood (Argonne National Laboratory)

The hafnium tests in the removable beryllium (RB) positions of HFIR described in section 5.1 allowed us to perform detailed spectral measurements using short-lived activities, fissionable materials, and thermal shields. These techniques cannot be used in long materiale irradiations and we must rely on a select number of dosimeters to adjust a previously determined neutron spectrum. Furthermore, new calculations of the neutron flux spectrum in the RB positions have recently been performed by D. Lillie (ORNL). Upon consideration of all of this new data, it was apparent that our previous measurements for the RB1[2] and RB2[3] experiments in HFIR should be reanalyzed. The results of this reanalysis are given below.

Table 4 lists revised neutron fluences and damage parameters for the RB1 and RB2 experiments. The flux and damage gradients can be determined by the following polynomial equation:

$$f(z) = a(1+bz+cz^2) \qquad (1)$$

where a = midplane value in Table 4, $b = -2.48 \times 10^{-3}$, $c = -9.76 \times 10^{-4}$, and z is the height in cm. This equation cannot be used to describe damage and helium production in copper, nickel, or stainless steel and calculations for the latter are given in Table 5.

Table 1. Measured Reaction Rates for HFIR-RB-Hf Tests

Values normalized to 11.0 MW parer level; accuracy ±2%

Reaction	Activation Rate, at/at-s		
	Al-RB1	Hf-RB1	Al-RB5
Thermal Reactions:			
$^{58}Fe(n,\gamma)^{59}Fe(10^{-11})$	9.75	1.14	10.50
$^{59}Co(n,\gamma)^{60}Co(10^{-9})$*	3.12	0.490	3.2'7
$^{63}Cu(n,\gamma)^{64}Cu(10^{-10})$	3.37	0.392	3.68
$^{64}Zn(n,\gamma)^{65}Zn(10^{-11})$	6.19	1.15	6.61
$^{176}Lu(n,\gamma)^{177}Lu(10^{-7})$*	3.22	0.390	3.45
$^{197}Au(n,\gamma)^{198}Au(10^{-8})$*	1.74	0.493	1.85
$^{238}U(n,\gamma)^{239}Np(10^{-10})$	7.28	2.69	8.36
$^{237}Np(n,\gamma)^{238}Np(10^{-8})$	1.63	0.265	1.73
Fast Reactions:			
$^{46}Ti(n,p)^{46}Sc(10^{-13})$	2.38	2.25	2.37
$^{47}Ti(n,p)^{47}Sc(10^{-13})$	3.74	3.53	3.81
$^{48}Ti(n,p)^{48}Sc(10^{-15})$	5.98	5.75	6.03
$^{54}Fe(n,p)^{54}Mn(10^{-12})$	1.72	1.58	1.73
$^{58}Ni(n,p)^{58}Co(10^{-12})$	2.32	2.16	2.36
$^{55}Mn(n,2n)^{54}Mn(10^{-15})$	5.31	4.99	5.29
$^{93}Nb(n,2n)^{92m}Nb(10^{-14})$	1.04	0.966	1.08
$^{237}Np(n,fission)(10^{-11})$	5.43	4.60	5.75
$^{238}U(n,fission)(10^{-12})$	7.88	7.65	8.15

*Dilute elements alloyed with aluminum.

Table 2. Adjusted Neutron Fluxes €or HFIR-RB-Hf Test

Midplane Values Normalized to 100 MW

energy	Neutron Flux, x 10^{14} n/cm^2-s		
	RB1	RB1 (Hf)	RB5
Total	23.4	10.2	24.5
Thermal (2.5 eV)[a]	9.44	1.10	9.90
Intermediate	8.75	4.03	9.09
Fast (>.1 MeV)	5.27	5.02	5.35

[a]Thermal maxwellian at 120°C.

Table 3. Damage Parameters for HFIR-RB-Hf Test

Midplane values in RB1 at 100 MW

Element		Damage/year[a] Bare DPA	Bare He, appm	Hf covered DPA	Hf covered He, appm
Al		19.3	4.67	18.5	4.49
Ti		11.3	4.19	10.3	4.00
V		13.1	0.16	12.0	0.15
Cr		11.0	1.17	10.3	1.11
Mn[b]		12.9	0.97	11.1	0.94
Fe		9.7	2.06	9.2	1.97
Co[b]		13.5	0.97	10.3	0.94
Ni	Past	11.0	31.0	10.1	29.0
	^{59}Ni	9.2	5247.0	0.3	
	Total	20.2	5278.0	10.4	189.0
Cu	Past	9.8	1.75	9.2	1.69
	^{65}Zn		5.31		
	mtal	9.8	7.06	9.2	1.71
Nb		9.8	0.39	9.4	0.37
Mo		7.7	--	7.2	--
316SS[c]		11.3	688.0	9.5	26.1

[a] 365 FPD assuming no burnout of Hf.
[b] Thermal neutron self-shielding may reduce damage in Mn, Co.
[c] 316SS: Fe(0.645), Ni(0.13), Cr(0.18), Mn(0.019), Mo(0.026).

Table 4. Revised Fluence and Damage Parameters for HFIR-RB1 and RB2 Experiments

Values at midplane; use eqn (1) for gradients

Energy	neutron Fluence, x 10^{22} n/cm^2-s RB1	RB2
Total	4.62	9.30
Thermal (<.5 eV)[a]	2.15	4.19
Intermediate	1.56	3.21
Fast (>.1 MeV)	0.91	1.90

Element		RB1 DPA	RB1 He, appm	RB2 DPA	RB2 He, appm
Al		11.07	2.93	23.1	5.84
Ti		6.48	2.41	13.5	4.92
V		7.52	0.10	15.7	0.20
Cr		6.31	0.71	13.2	1.42
Mn[b]		7.51	0.61	15.6	1.21
Fe		5.52	1.27	11.5	2.52
Co[b]		8.37	0.61	17.1	1.20
Ni	Fast	6.30	18.	13.1	36.
	^{59}Ni	6.53	3705.	17.4	9868.
	mtal	12.83	3723.	30.5	9904.
	Fast	5.57	1.09	11.6	2.2
	^{65}Zn	<.01	3.33	0.04	18.6
	mtal	5.57	4.42	11.6	20.8
Nb		5.50	0.24	11.5	0.47
Mo		4.30	-	9.0	-
316 SS[c]		6.62	485.	14.3	1289.

[a] Thermal maxwellian at 60°C.
[b] Thermal self-shielding may reduce damage for Mn, Co.
[c] 316 SS = Fe (.645), Ni (.13), Cr (.18), Mn (.019), Mo (.026).

Table 5. Revised Helium and DPA Rates for 316 SS for HFIR-RB1 and RB2 Experiments

Helium includes ^{59}Ni and fast reactions
Damage includes extra thermal kick (He/567)

Height, cm	RB1 He, appm	RB1 DPA	RB2 He, appm	RB2 DPA
0	485	6.62	1289	14.3
3	478	6.55	1274	14.2
6	459	6.36	1232	13.7
9	427	6.05	1161	13.1
12	383	5.62	1059	12.2
15	328	5.07	931	11.0
18	265	4.40	776	9.6
21	196	3.63	596	7.9
24	124	2.74	399	6.0

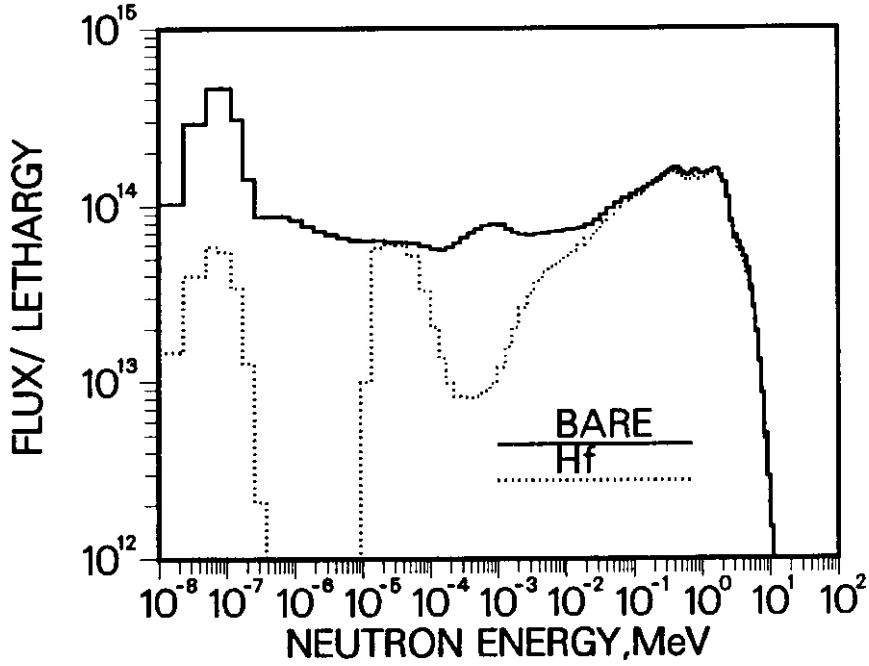

rig. 1. Comparison of STAY'SL-Adjusted Bare and Hafnium-Shielded Neutron Flux spectra Measured in the RB1 Position of HFIR. The Large Dips around 1 and 30 eV *are* Caused by Hafnium Resonances.

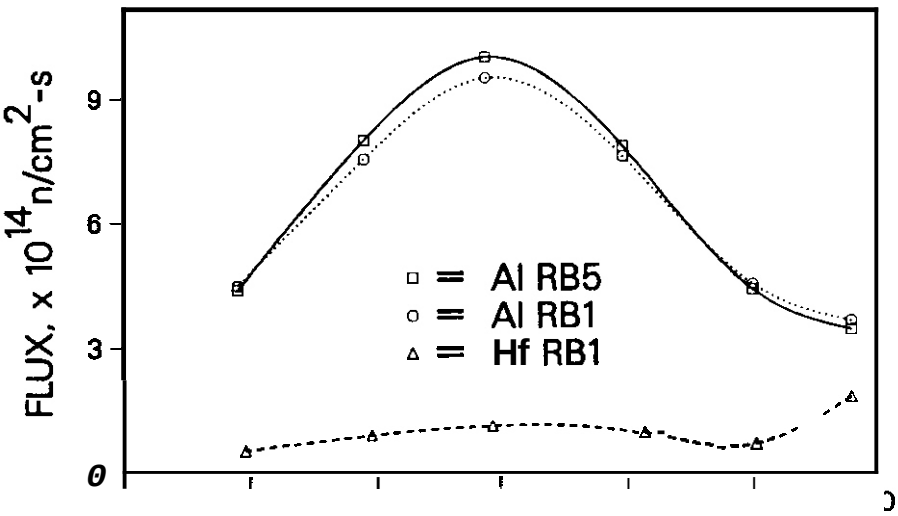

Fig. 2. Vertical Gradients are Shown for the Thermal Neutron Flux Measured With and Without Hafnium in Positions RB1 and RB5 of WIR.

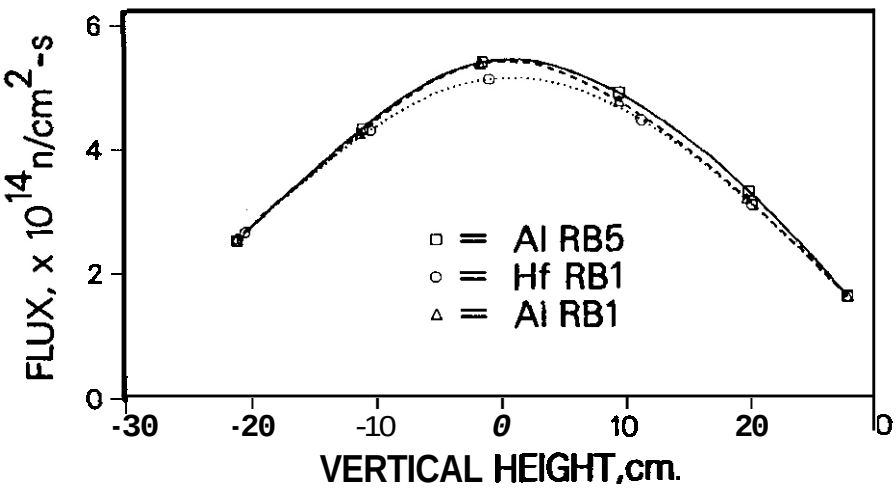

Fig. 3. Vertical Fast Flux (>,1 MeV) Gradients are Shown for Positions RB1 and RE5 of HFIR. clearly, the Hafnium Shield has Little Effect on the Fast Flux.

The present results indicate a substantial increase in the fast flux and damage rates for both experiments. The flux above 0.1 MeV has been increased by about 30% for RB1 and 80% for RB2; however, the thermal flux and flux above about 1-2 MeV are not very different than before. In other words, most of the flux increase has occurred between about 0.1 to 1 MeV where our monitore are not very sensitive. If we compare damage rates this spectral change becomes more apparent since damage for 316 SS has only increased by 17t for RB1 and 33% for RB2. Helium rates actually show a decline since the very fast flux (r5 MeV) which produces helium by (n,α) rections is actually less than before. For iron, the helium has been reduced by 23t for RB1 and 106 for RB2. For nickel and stainless steel, the thermal helium effect has also been reduced primarily due to differences in the epithermal energy region.

6.0 References

1. L. R. Greenwood and R. K. Smither, Hafnium Core Piece Test in ORR-MFE4, Damage Analysis and Fundamental Studies Quarterly Progress Report, DOE/ER-0046/17, pp. 5–10, May 1984.

2. L. R. Greenwood, Fission Reactor Dosimetry-HFIR-RB2, ibid., DOE/ER-0046/22, pp. 5-7, August 1985.

3. L. R. Greenwood and R. K. Smither, ANL/FPP/TM-197, SPECTER: Neutron Damage Calculations for materials Irradiations, January 1985.

7.0 Future Work

Analysis is in progress for the JP1 experiment in HFIR. We expect to receive samples shortly from the full cycle hafnium test in HFIR and from the JP3 experiment.

SPECTRAL ANALYSIS FOR THE REAL84 PROJECT

L. R. Greed (Argonne National Laboratory)

1.0 Objective

To establish standardized dosimetry procedures in order to reduce uncertainties in damage analysis and correlation studies.

2.0 S

Results of our spectral analyses for seven differunt neutron fields have been submitted to the REAL84 Project. an international intercomparison of neutron spectral adjustment procedures and damage calculations. Our results will be compared with those from about 20 different laboratories by the International Atomic Energy Agency in Vienna.

3.0 r

Title: Dosimetry and Damage Analysis
Principal Investigator: L. R. Greenwood
Affiliation: Argonne National Laboratory

4.0 Relevant DAFS Program Plan Tasks/Subtasks

Task II.A.6 Dosimetry Standardizaion
Subtask II.A.6.1 Interlaboratory Calibration Programs

5.0 Accomplishments and Status

Analysis has been completed for five test cases aS part of the REAL84 Project, an international intercomparison of data and procedures used to adjust neutron spectra and predict damage in materials. I was part of an international committee which planned this exercise at several recent meetings. This project is a follow-up to the REAL80 Project which we participated in previously.[1] In this exercise data sets were provided for seven different test cases. Each participant was then asked to analyze the data by performing a spectral adjustment necessitating critical judgments regarding the data provided and then calculating selected damage parameters.

Two of the data sets were provided by us, namely a Be(d,n) spectrum measured at a deuteron energy of 16 MeV at the Argonne Tandem Accelerator, and a fusion-like 14-MeV spectrum with room-return neutrons measured at RTNSII. Analysis was performed for five other spectra, namely a reactor cavity spectrum in a commercial reactor (Arkansas Nuclear One), two pressure vessel simulator spectra measured in the poolside facility of the Oak Ridge Research Reactor, the coupled Fast Reactivity Measurement Facility at the Idaho National Engineering Laboratory, and a ^{235}U standard neutron field.

The results of our analysis have been sent to W. L. Zijp at ECN, Petten, The Netherlande and to R. Cullen at the IAEA in Vienna, Austria. Over 20 different laboratories are expected to participate in the exercise. The plan is to complete the comparisons for presentation at the Sixth ASTM-EURATOM Symposium on Reactor Dosimetry in April 1987.

6.0 References

1. W. L. eijp et al., Final Report on the REAL80 Exercise, ECN-128, INDC(NED)-7, February 1983.

7.0 Future work

We will assist the IAEA in the analysis of the data. The ultimate goal is to establish Standardized inter national data files and procedures.

CHAPTER 3

REDUCED ACTIVATION MATERIALS

NEUTRON-INDUCED SWELLING AND MICROSTRUCTURAL DEVELOPMENT OF SIMPLE Fe-Mn and Fe-Cr-Mn ALLOYS IN FFTF

F. A. Garner and H. R. Brager (Hanford Engineering Development Laboratory)

1.0 Objective

The object of this effort is to determine those factors which control the swelling of alloy systems which have the potential for reduced activation.

2.0 Summary

Three binary Fe-Mn and six Fe-Mn-Cr ternary alloys have been irradiated in FFTF at temperatures of 420, 500 and 600°C to exposures ranging from 9-14 dpa. In contrast to the behavior of Fe-Cr-Ni alloys irradiated under comparable conditions there is essentially no dependence of void swelling on chromium or manganese content, and there also appears to be no dependence on irradiation temperature. Like Fe-Cr-Ni alloys, however, Fe-Cr-Mn and Fe-Mn alloys do swell at ~1%/dpa after the transient regime.

While density change data indicate an apparent weak dependence of swelling on manganese level, microscopy shows that radiation-induced second phases that form may be responsible for a densification of the matrix. This densification approaches 2.2% at 35% manganese.

3.0 Program

Title: Irradiation Effects Analysis (AKJ)
Principal Investigator: D. G. Doran
Affiliation: Hanford Engineering Development Laboratory

4.0 Relevant DAFS Program Plan Task/Subtask

Subtask II.C.1 Effects of Material Parameters on Microstructure

5.0 Accomplishments and Status

5.1 Introduction

In previous reports[1,2] it was shown that the swelling of simple Fe-Mn binary and Fe-Mn-Cr ternary alloys in FFTF-MOTA at 520°C and ~14 dpa is remarkably insensitive to the chromium level and only weakly dependent on the manganese level as shown in Figure 1a. Figure 1b shows that this behavior is quite different from that of Fe-Cr-Ni alloys which are strongly sensitive to both chromium and nickel for comparable irradiation conditions.

Additional immersion density data are now becoming available for this irradiation series. The portion of the data matrix that is now complete leads us to revise somewhat our earlier conception of the parametric dependence of swelling in the Fe-Cr-Mn system.

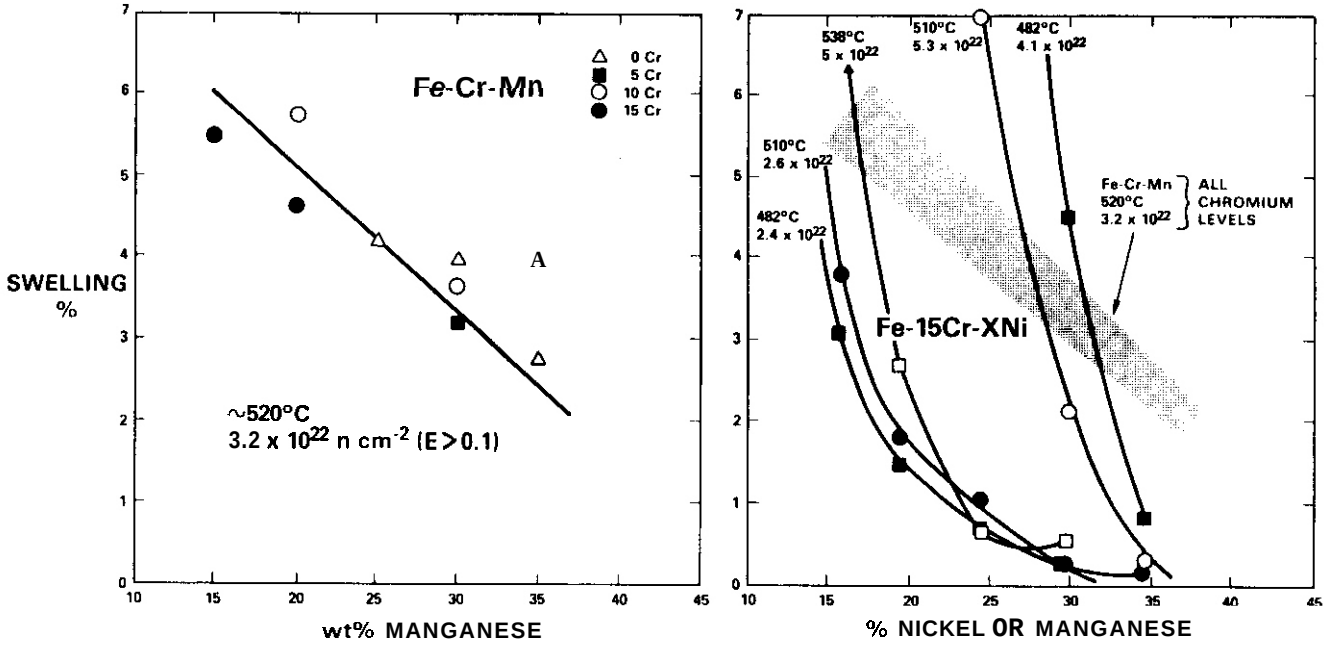

FIGURE 1. Comparison between neutron-induced swelling in Fe-Cr-Mn and Fe-Cr-Ni alloys.[1]

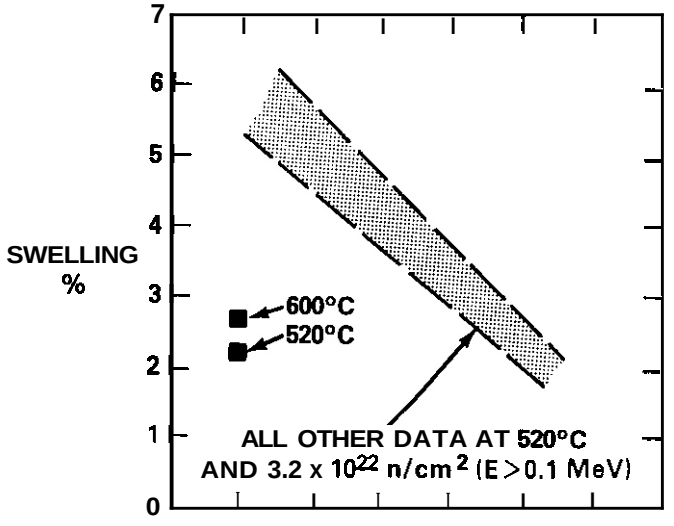

FIGURE 2. Comparison of additional data on swelling of Fe-5Cr-15Mn at 14 dpa and the trend of previously published data for other Fe-Cr-Mn alloys at 520°C and 14 dpa.[2]

5.2 New Data

Figure 2 shows that the swelling data of one alloy, Fe-5Cr-15Mn, does not fit the behavior typical of the other previously reported alloys irradiated at 520°C and 14 dpa. At 600°C and 14 dpa essentially the same swelling is observed for this alloy, however, which leads us to speculate that irradiation above 500°C has caused some relatively temperature-independent phase evolution for this alloy that is different from that of the others. Figure 3 shows that, with the exception of Fe-5Cr-15Mn, all other alloys exhibit after irradiation at 600°C and 14 dpa essentially the same swelling as observed at 520°C and 14 dpa. The scatter at 600°C is somewhat larger, however. This implies that there is little or no dependence of swelling on temperature in the range 520-600°C. It is desired to determine whether the independence of

temperature extends as low as 420°C but unfortunately the data at 420°C exist only at 9 dpa, as is also shown in Figure 3. Note that at 420°C most alloys not only densify but that rather large densifications are exhibited at the higher manganese levels.

At this point we can borrow from our experience on Fe-Cr-Ni alloys and remember that at low temperatures there is usually no temperature dependence of swelling and thus we can often plot the data ignoring the temperature.[3,4] Note in Figure 4 that we can draw lines between (420°C, 9 dpa) data and (520°C, 14 dpa) data for each alloy and that each line exhibits a slope of ~1%/dpa. This apparent swelling rate is identical to that observed for all other austenitic alloys in the post-transient regime.[3]

The densification shown in Figures 3 and 4 tends to imply that much of the previously observed composition dependence of post-irradiation density change is a reflection of a process other than void swelling. Therefore the composition dependence of swelling in the Fe-Cr-Mn system appears to be even less than previously reported.[1]

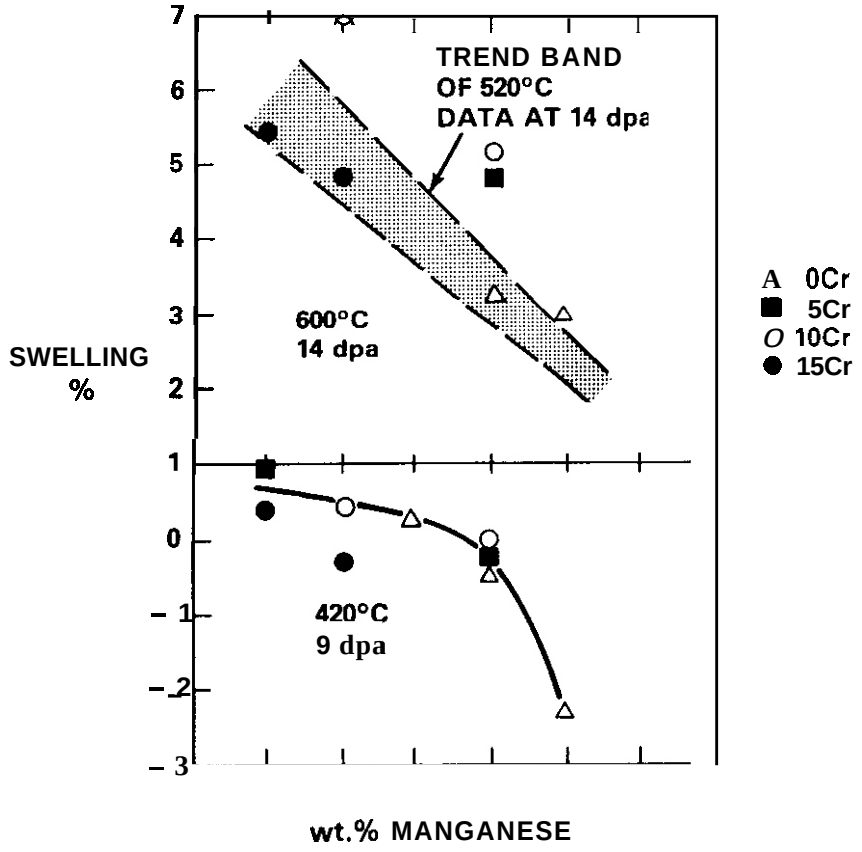

FIGURE 3. New data showing swelling of Fe-Cr-Mn alloys at 420°C and 600°C. Some alloys densify at 420°C.

5.3 Microstructural Oevelopment

Examination of these alloys by electron microscopy is now in progress. Two alloys irradiated at 520°C have been examined. These are Fe-10Cr-30Mn and Fe-10Cr-20Mn. Both contained large voids (~100 nm) and comparable dislocation densities (~3 x 10^{10} cm^{-2}). There were two distinct differences in microstructure, however. First, the 20% manganese alloy had a moderate density (~3 x 10^{13} cm^{-3}) of large (200-500 nm) and sometimes elongated precipitates which are as yet unidentified. Similar precipitates existed at much lower densities in the 30% manganese alloy. Second, the 20% manganese alloy contained a higher density of voids, ~2 X 10^{14} cm^{-3} as compared to ~5 X 10^{13} cm^{-3} for the 30% manganese alloy. This difference in void density was the major cause of the difference in local swelling (8% vs. 3%) of the two alloys. Typical micrographs are shown in Figure 5.

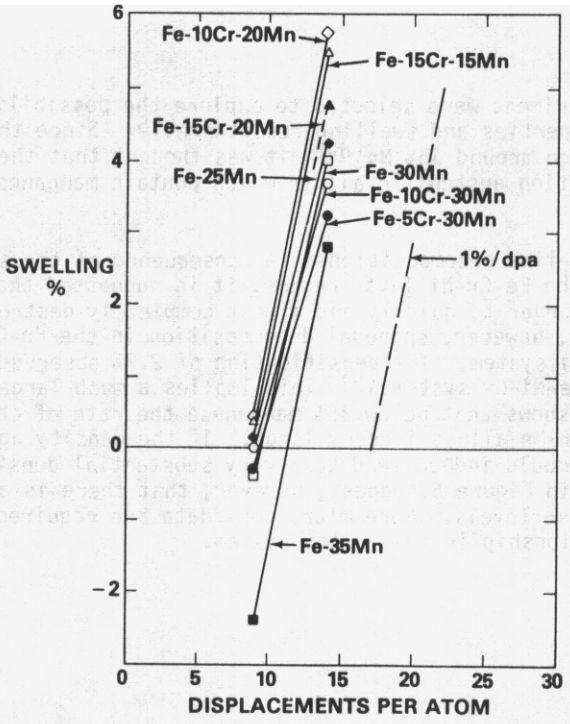

FIGURE 4. Plot of Fe-Cr-Mn swelling data assuming independence of swelling on temperature between temperatures of 420 and 520°C.

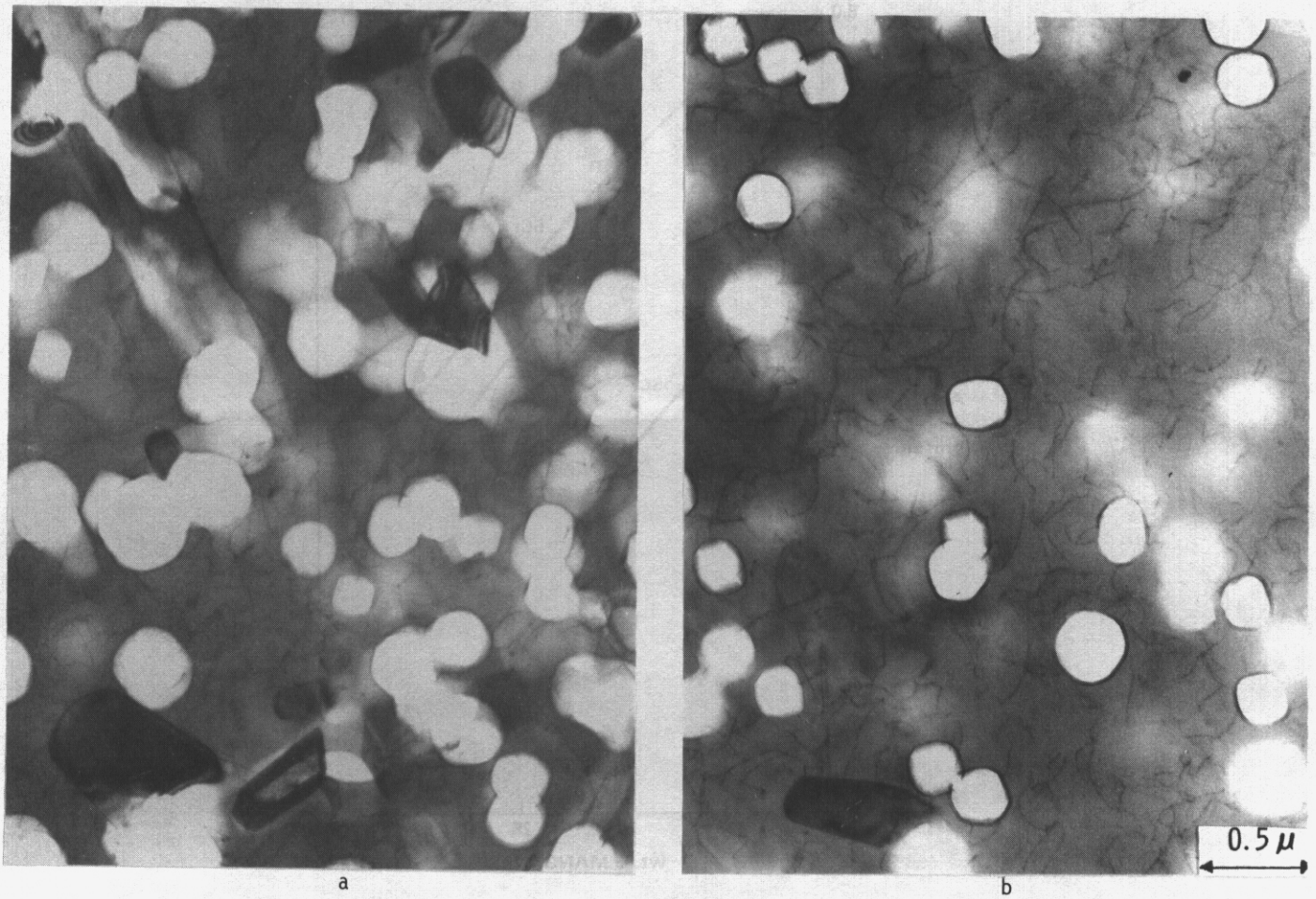

a b

FIGURE 5. Micrographs of (a) Fe-10Cr-20Mn, and (b) Fe-10Cr-30Mn, both irradiated to 14 dpa at 520°C in FFTF.

5.4 Discussion

The alloys irradiated in this experiment were selected to explore the possibility that a correlation exists between anomalous Invar properties and swelling resistance.[5] Since the Fe-Cr-Mn system also exhibits Invar behavior in the range around 35% Mn[6-8] it was thought that there might be some advantage to developing low activation austenitic alloys which contain manganese levels of this magnitude.

Just as radiation-induced spinodal-like decomposition is a consequence of the same metastability that produces anomalous properties in the Fe-Cr-Ni Invar regime, it is suggested that spinodaling also occurs in the Fe-Cr-Mn Invar regime. In order to quickly and almost completely destroy the compositional and temperature dependence of swelling, however, spinodal decomposition in the Fe-Cr-Mn system must occur faster than it does in the Fe-Cr-Ni system. The densification of 2.2% observed in Fe-35Mn is much larger than the 0.9% that occurs in the Fe-Ni-Cr system.[9] This implies a much larger driving force in the Fe-Cr-Mn system. Figure 6 indeed shows that below 35% manganese the rate of change with manganese content of pre-irradiation density of Fe-Cr-Mn alloys is very large. If the density again rises steeply above 35% manganese, spinodal decomposition could indeed lead to a very substantial densification and a large driving force. The micrographs shown in Figure 5 suggest, however, that there is another phase separation process occurring at lower manganese levels. More microscopy data are required to determine the nature of the swelling-phase stability relationship in this alloy system.

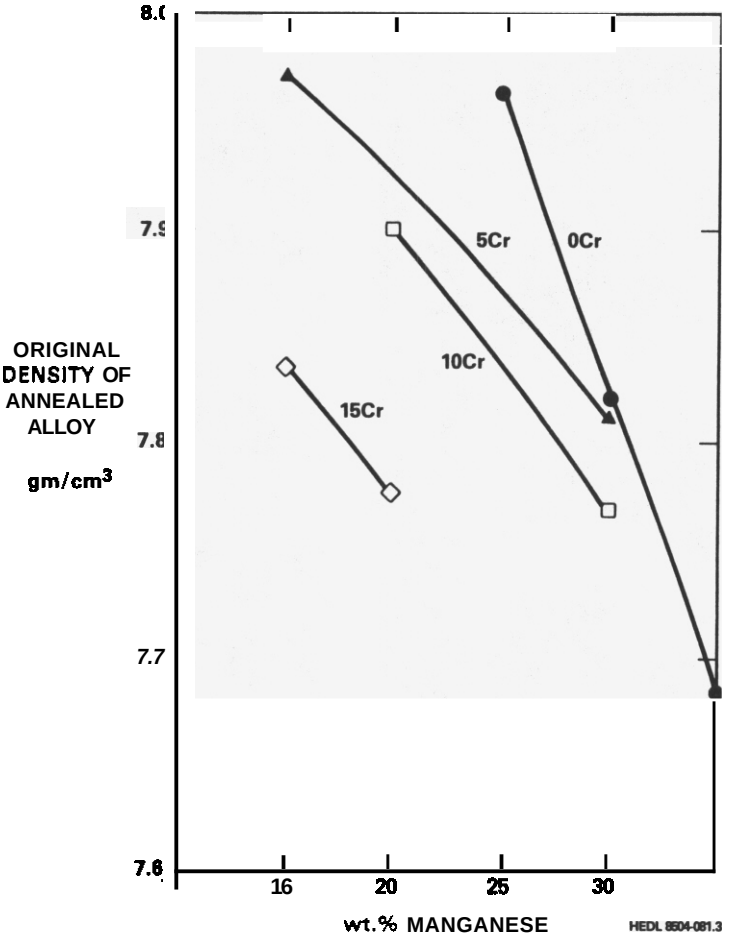

FIGURE 6. Dependence of pre-irradiation density on composition for annealed Fe-Cr-Mn alloys.

5.5 Conclusions

There does not appear to be any large advantage to be gained at higher (120%) manganese contents in terms of the intrinsic swelling resistance of simple Fe-Cr-Mn alloys. However, this conclusion may not apply to the solute-modified Fe-Cr-Mn alloys which have not yet been examined. If radiation-induced precipitation and/or spinodal-like decomposition is causing both a large densification and the destruction of the swelling resistance, then the study of the differences between Fe-Cr-Mn and Fe-Cr-Ni Invar alloys may lead to clues as to how to suppress the spinodal-like process and extend the incubation period of swelling. Therefore examination of the Fe-Cr-Mn Invar alloys will continue despite the initially unsuccessful application of the Invar-swelling resistance correlation to the simple Fe-Cr-Mn system.

6.0 References

1. H. R. Brager and F. A. Garner, "Swelling of Fe-Cr-Mn Ternary Alloys in FFTF," DAFS Quarterly Progress Report DOE/ER-0046/19, November 1984, 31-33.

2. F. A. Garner and H. R. Brager "Neutron-Induced Swelling of Fe-Cr-Mn Ternary Alloys," DAFS Quarterly Progress Report, DOE/ER-0046/19, May 1985, pp. 41-45.

3. F. A. Garner, J. Nucl. Mater., 122 & 123 (1984) 459-471.

4. F. A. Garner, "Application of High Fluence Fast Reactor Data to Fusion-Relevant Materials Problems," J. Nucl. Mater., 133 & 134 (1985) 113-118.

5. H. R. Brager and F. A. Garner, "Fundamental Alloy Studies," DAFS Quarterly Progress Report DOE/ER-0046/17, May 1984, 93-101.

6. Y. Endoh, Y. Noda and M. Iizumi, J. Phys. Soc. Japan, 50, No. 2 (1981) 469-475.

7. O. G. Sokolov and A. I. Mel'ker, Soviet Physics-Doklady, 9, No. 1 (1965) 1019-1021.

8. O. A. Khomenko and I. F. Khil'kevich, Met. Term. Obra. Met., 6 (1982) 42-44.

9. H. R. Brager and F. A. Garner, "Swelling of Fe-Ni-Cr Ternary Alloys at High Exposure," DAFS Quarterly Progress Report DOE/ER-0046/16, Feb. 1984, 38-45.

7.0 Future Work

Density change and microscopy data will continue to be accumulated on both simple and solute-modified Fe-Cr-Mn alloys.

8.0 Publications

None.

CHAPTER 4

FUNDAMENTAL MECHANICAL BEHAVIOR

A THIRD STAGE OF IRRADIATION CREEP INVOLVING ITS CESSATION AT HIGH NEUTRON EXPOSURES

F. A. Garner and B. J. Makenas (Hanford Engineering Development Laboratory) and D. L. Porter (Argonne National Laboratory, EBR-II Project)

1.0 Objective

The object of this effort is to determine the mechanism by which radiation affects the properties and dimensions of reactor components.

?.0 Summary

As swelling approaches 5-10% in AISI 316, the creep rate appears to rapidly decline and eventually vanish. There may be some correlation between this phenomena and changes in failure mode that also appear to be related to void swelling.

3.0 Program

Title: Irradiation Effects Analysis (AKJ)
Principal Investigator: D. G. Doran
Affiliation: Hanford Engineering Development Laboratory

4.0 Relevant OAFS Program Plan Task/Subtask

Subtask II.C.14 Models of Flow and Fracture Under Irradiation
Subtask II.C.16 Composite Correlation Models and Experiments

5.0 Accomplishments and Status

5.1 Introduction

It is generally accepted that in structural steels at fusion-relevant temperatures that there is one minor stage of irradiation creep followed by two major stages.[1-3] The minor stage is transient in nature and is found only in cold-worked steels very early in the irradiation. It results from an initial reduction in dislocation density. The first major stage is characterized by a steady-state creep rate which appears to be athermal in nature and which is independent of void swelling. In the second major stage the creep rate is accelerated and appears to be proportional to the swelling rate, at least for relatively low swelling levels (<5%). In this stage the creep rate therefore has the same parametric sensitivities as those associated with the swelling rate.

Analysis of creep data extracted from components with higher levels of swelling now shows that coincident with 5-10% swelling levels, a third major stage of creep evolves in which the creep rate begins to rapidly decline with further exposure and eventually vanish.

5.2 Fuel Pin Data

This third stage was first bought to light when the measured creep strains of highly irradiated 20% cold-worked fuel pin cladding fell substantially below the levels predicted by a correlation developed from

creep tube data at lower fluence.[4,5] An example is shown in Figure 1 for a pin with a high fluence to burn-up ratio and a very high neutron exposure.

It is important to note that the creep prediction shown in Figure 1 is that of an older correlation which did not include either of the insights of a swelling rate which approached 1%/dpa or creep rates proportional to swelling rates.[1] Thus the creep strains predicted by more recent correlations would be even larger. emphasizing once again the difference between measured and predicted creep strains.

Examination of the strains of other fuel pins at lower exposure levels provides some additional insight. Figure 2 shows the strains measured in a fuel pin at lower fluence and for which the fluence to burn-up ratio is relatively high but not as high as that of the pin shown in Figure 1. Note once again that the measured creep is significantly less than predicted. Figure 3 shows the strains of a pin in which the fluence to burn-up ratio is much lower but in this case the measured creep is comparable to or greater than the predictions. The agreement is best at temperatures where pressurized tube data were available in this fluence range. Otherwise an under-prediction of creep strains would be anticipated. In general the trends of these two pins are reproduced in other pins, with the difference between creep predictions and measurements being somehow dependent on the fluence to burn-up ratio.

The fluence to burn-up ratio is largely determined by the enrichment of the fuel. In pins where the fluence is large but the burn-up is low swelling gets started without the presence of significant stress. The stress arises from the generation of fission gases and therefore increases monotonically with neutron exposure. Thus when creep begins in such a pin swelling is already rather advanced. In pins which have higher enrichments and therefore higher burn-up rates creep gets a head start on swelling and the predictions based on pressurized tube data are comparable to that actually observed in the fuel pins. Thus it appears that the level of swelling may be related to the short-fall observed in creep.

Since fuel pins are subject to complex histories of stress, temperature and chemical environment, the possibility can not be ruled out that the unexpectedly low creep strains might have arisen as a result of some previously unsuspected history dependence of microstructural evolution.

5.3 Pressurized Tube Data

In order to investigate the sources of these sometime low creep strains it is better to analyze the deformation of non-fueled creep tubes at constant pressure. By comparing the strains of tubes at different internal pressures one can get some idea of the relationship between stress, swelling and creep. If one uses measurements along the length of relatively long pressurized tubes data at a given stress can also be obtained as a function of neutron flux and fluence.

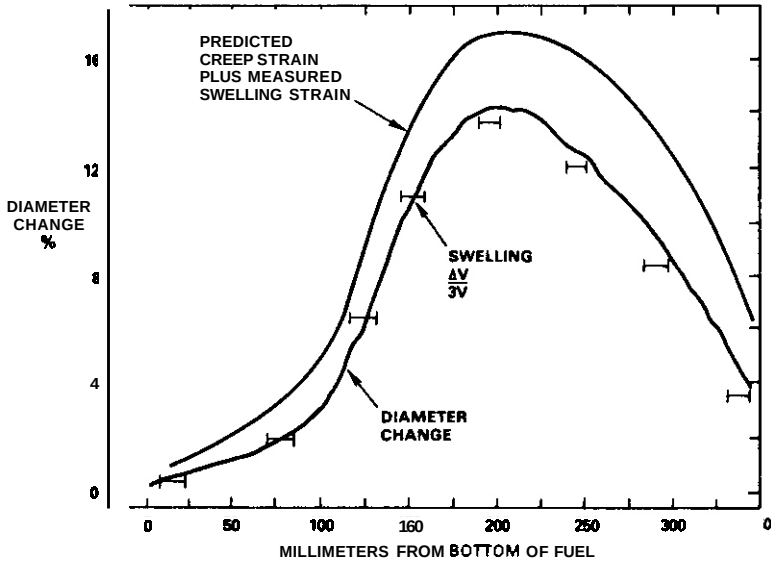

FIGURE 1. Comparison of predicted and measured diametral strains of 20% cold-worked AISI 316 FFTF Core-4 cladding for a fuel pin irradiated to a peak fluence of 1.7 x 10^{23} n/cm^2 (E >0.1 MeV).[4,5] Note that the measured diameter changes appear to arise primarily from the swelling-related strains.

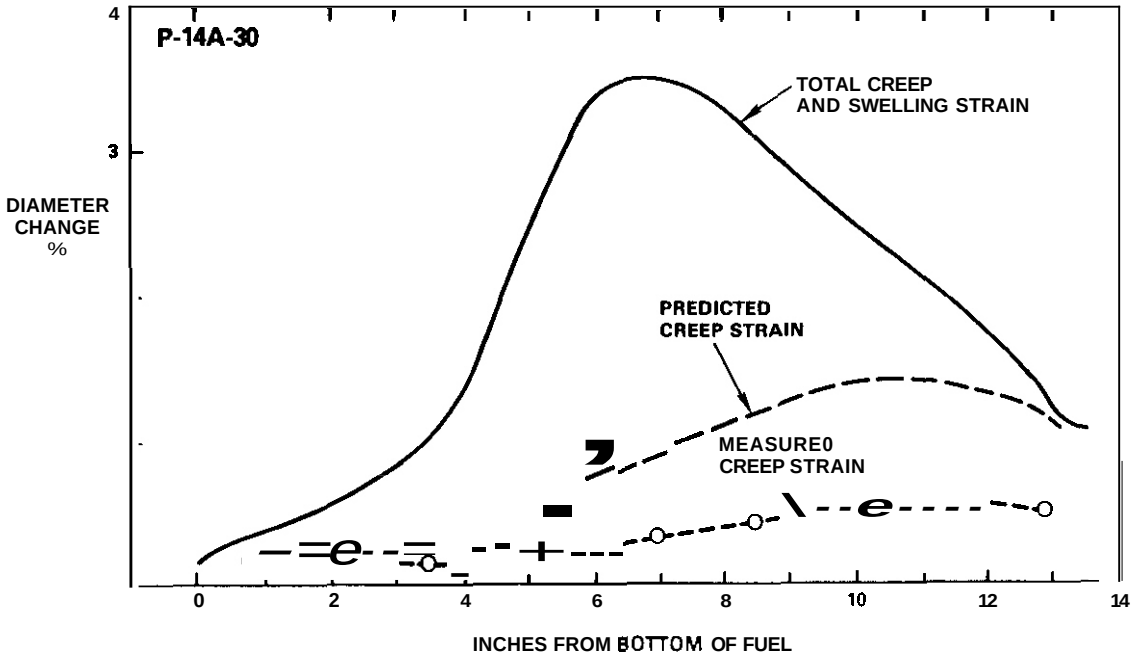

FIGURE 2. Comparison of measured strains and predictions for pin P-14A-30 clad with FFTF Core-1 20% cold-worked AISI 316. This high fluence to burn-up ratio pin reached a peak of 11 x 10^{22} n/cm^2 (E >0.1 MeV) and 9.0% burn-up. The volumetric swelling at the position of maximum strain is 9.4%.

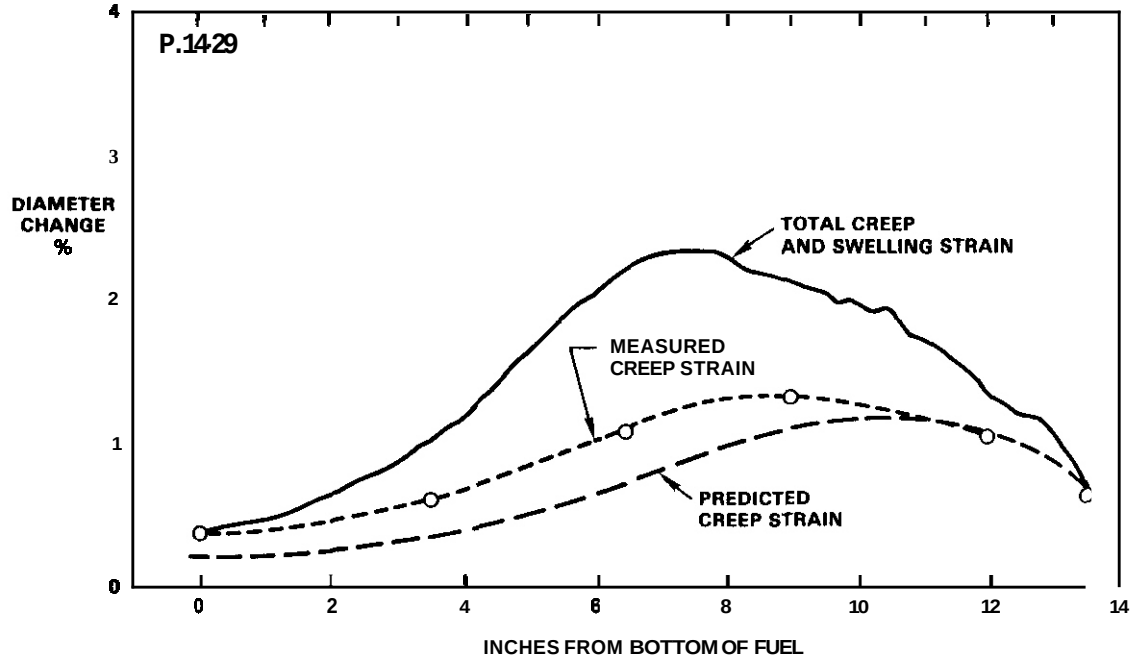

FIGURE 3. Comparison of measured and predicted strains for pin P-14-29 clad with FFTF Core-1 20% cold-worked AISI 316. The low fluence to burn-up ratio pin reached a peak of 8 x 10^{22} n/cm^2 (E > 0.1 MeV) and 11.5% burn-up.

Helium-filled tubes of this type have been irradiated in EBR-II for both AISI 304 and AISI 316 steels and data from these have been reported elsewhere.[6,7] In this study we will concentrate on tubes of AISI 316 (N-lot heat) irradiated at 550°C (±10°C) in each of the following conditions; annealed, 10% cold-worked, 20% cold-worked and a Garafolo-type cold-worked and aged condition (Heat Treat D, fully carbide precipitated). The latter condition is known to induce early swelling. It should be noted that the 10% cold-worked condition was achieved by first annealing a 20% cold-worked tube and then reworking it. Thus the two cold-work conditions do not have the same starting state since the original 20% cold-worked material was annealed using another technique in an industrial laboratory.

These tubes have a 10 inch (0.25 m) pressurized section located above the core centerline and the temperature was maintained by preheating the sodium coolant with a solid tantalum heater in that section of the tube which is below the core centerline. The end-of-life internal gas pressure of each tube was measured when the tube was removed from the reactor for the final examination. Creep strains were measured at both core center and other axial positions during interim examinations. Some tubes were sectioned into axial increments upon removal from the reactor and imnersion density measurements were performed on them.

Figure 4 shows the total diametral strains measured at core centerline for three 10% cold-worked tubes at different stress levels. As the stress increases the creep and swelling strains also increase but together they do not exceed the strain-rate (0.33%/dpa) that one would expect from steady-state swelling alone (1/3 of 1%/dpa). The increase in strain rate between tubes at 15 and 30 ksi is surprisingly small, however. Figure 5 shows the strain for the cold-worked and aged Heat Treat D condition which is known to swell sooner than cold-worked steel. Note that while the transient regime of diametral deformation decreases in duration with increasing stress, the post-transient deformation rate does not appear to change. Even more significantly, the total deformation rate does not exceed the 0.33%/dpa expected from steady-state swelling alone. Indeed it appears that the well-known stress dependence of creep rate has disappeared somewhere between hoop stress levels of 0 and 15 ksi. A similar behavior is shown in Figure 6a for the 20% cold-worked condition. Note that both the Heat Treat D and the 20% cold-worked condition swell sooner in the stress-free condition than does the 10% cold-worked condition. This is probably a reflection of the different starting conditions for the 10 and 20% cold-worked steels.

When the swelling and creep strains are separated, it becomes more obvious why the total strain rate appears to saturate at a level independent of the stress and starting condition. Figure 6b shows the results of density change measurements performed along the length of the 30 ksi tube. Comparison of the stress-affected swelling strains with those of the stress-free tube indicates a relatively small influence of stress in accelerating the onset of steady-state swelling. However, when the stress-affected swelling strains are subtracted from the total deformation at 30 ksi it can be seen that the creep strains indeed begin to saturate coincident with swelling levels of 7-10%. The stress-dependence of creep disappears because creep itself disappears.

Further insight can be obtained on this phenomenon by measuring the strains of three Heat Treat D tubes removed at a lower level of irradiation. Note that the strains of these tubes are compared in Figure 7 with those of the nominally identical tubes at higher fluence shown in Figure 5. These lower fluence pins were sectioned in axial increments and density change measurements made. Note in Figure 8 that if one uses the stress-free swelling strain, the onset of creep saturation is camouflaged somewhat. This may explain why this phenomenon has not yet been observed in the shorter pressurized tubes used for the U.S. breeder reactor studies. It is the practice in those studies to calculate creep using the stress-free strains in order to avoid sacrificing a valuable stress-free tube at low and intermediate fluence levels. Thus the stress-enhanced portion of the swelling strain is included as a creep contribution which thereby obscures the observation of the third stage of creep.

The annealed tubes from this experimental series were not used in this analysis because these tubes after removal from the reactor were found to have lost their gas pressure, indicating that they failed sometime during irradiation. These tubes start to swell sooner than do tubes in either the cold-worked or Heat Treat D conditions. Note in Figure 9 that the 30 ksi tube failed somewhere before a diametral strain of >2% was attained. Judging from the stress-free strain behavior, most of this strain is associated with swelling, indicating a swelling level probably on the order of 25%. While the annealed tubes cannot be confidently used to study the postulated third stage of creep, they do suggest another ramification of the swelling-creep interaction. In another recent paper it has been suggested that if large levels of void swelling tend to interfere with irradiation creep, it might be expected that ex-reactor deformation and failure modes may also be affected.[5] It was shown in that paper that large changes in fracture mode indeed occur for swelling levels on the order of 5-10%.[5] Perhaps then, the in-reactor failure modes are also affected by swelling. While the failure of the annealed tubes cannot be taken as proof of a causal relationship between the reduction of irradiation creep and the subsequent failure of the tube, it does signal that additional attention should be paid to the potential for such a relationship. It is difficult to imagine how the applied and swelling-generated stresses (particularly at stress risers and triple points) are being relieved when the macroscopic creep rate seems to disappear.

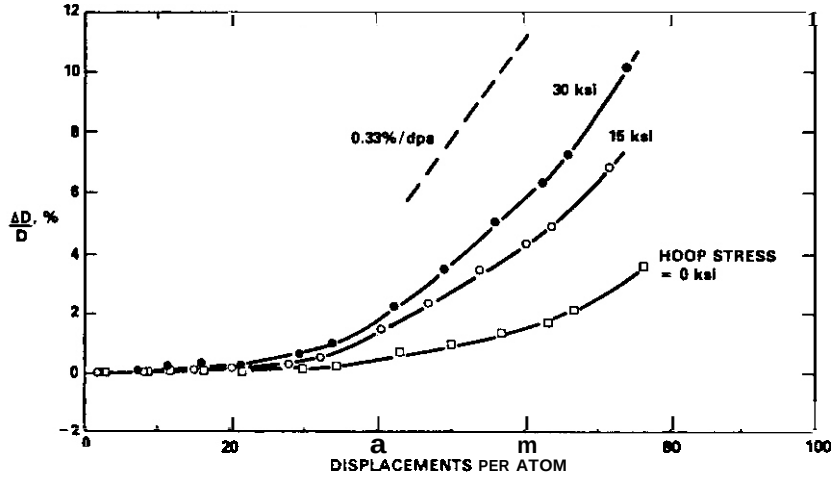

FIGURE 4. Diametral strain at 550°C observed at core centerline of EBR-II for three pressurized tubes of N-lot AISI 316 in the 10%cold-worked condition.

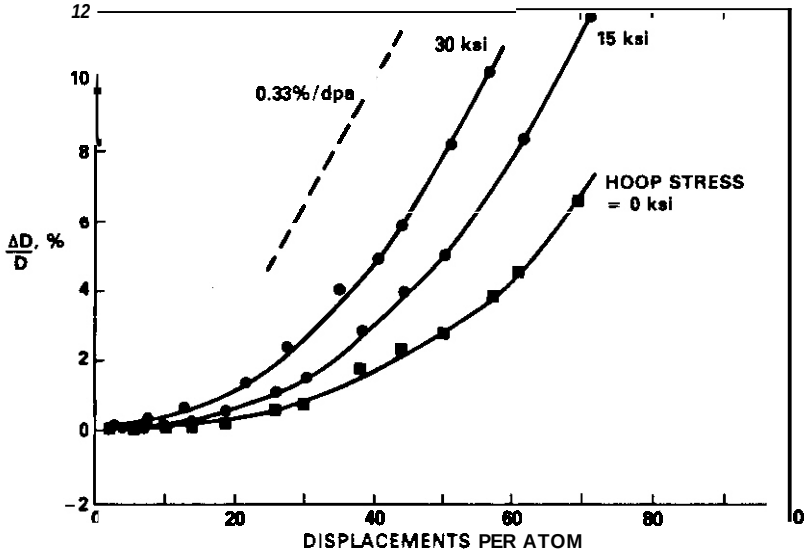

FIGURE 5. Diametral strains at 550°C observed at core centerline of EBR-II for three pressurized tubes of N-lot AISI 316 in the Heat Treat D condition.

5.4 Discussion

The microstructural origins of this phenomenon are not at all obvious and are currently under study. Some observations can be made, however, that may at least partially explain the observed results. First of all, at these swelling levels the overwhelming majority of dislocations terminate at void surfaces, a situation in which the climb rate of dislocations can be strongly affected by pipe diffusion of defects into the voids. This will tend to change the bias of the dislocation network. Second, the glide distance of dislocations will be decreased as the voids become the dominant obstacle. This will reduce the amount of creep that can occur for a given level of irradiation. Third, if the creep process is now restricted primarily to irradiation-induced climb of dislocations, one can envision a situation in which the SIPA creep mechanism[8] may no longer operate effectively. This mechanism requires that the climb of dislocations lying on some planes is enhanced by the applied stress state while other less favorably oriented dislocations are inhibited in their climb rate. In short, this mechanism requires that dislocations lie on different planes with different Burgers vectors. Gelles and coworkers have recently shown that large applied stresses lead to an anisotropy of dislocations such that unfavorably oriented dislocations exist at substanitally reduced densities while favorably oriented dislocations increase in density.[9,10] Similar stress-induced anisotropies have been observed in the Frank loop population.[11,12] Hence, the SIPA creep mechanism may not function very effectively after the stress state has substantially altered the dislocation and loop microstructure.

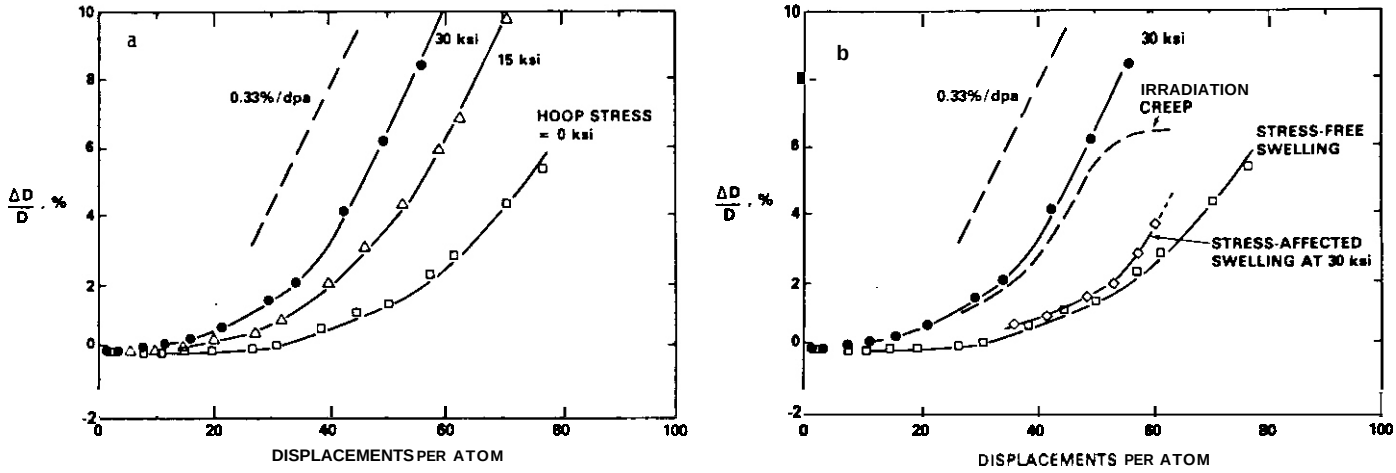

FIGURE 6. a) Deformation observed in pressurized tubes of 20% cold-worked AISI 316 irradiated in EBR-II at 550°C. Note that the total strain rate does not exceed 0.33%/dpa, even at very high stress levels. b) Density measurements on the 30 ksi pressurized tube show that stress accelerates the rate of swelling and its approach to 1%/dpa, but also causes the creep rate to approach zero at high swelling levels.

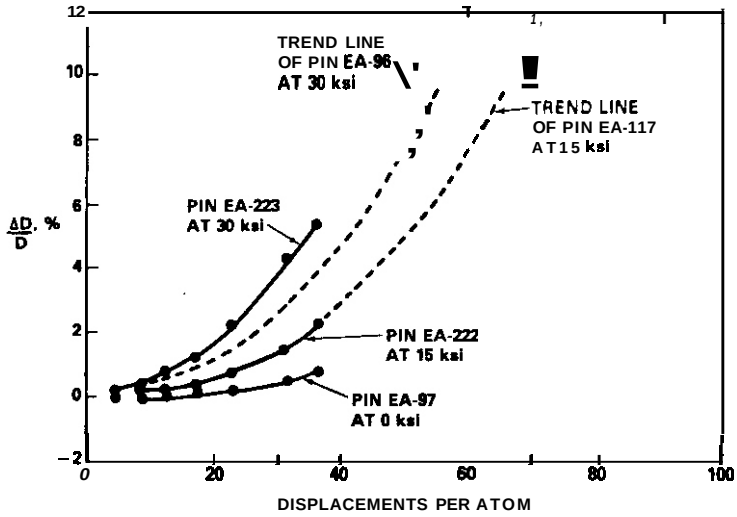

FIGURE 7. Comparison of the strains at 550°C of three pressurized tubes in the Heat Treat 0 condition with those at higher fluences shown in Figure 5.

Since the diametral creep rate does saturate at approximately one-third of 1%/dpa, the latter being the steady-state swelling rate, this implies that stress-affected swelling itself is isotropic. Increases in volume require dislocation motion but the apparent disappearance of creep implies greatly reduced mobility of dislocations, or at least a reduction in their ability to sense and react to the stress state. This apparent paradox awaits the acquisition of more data before it can be resolved.

5.5 Conclusions

Coincident with the attainment of swelling levels in the range 5-10%, irradiation creep in AISI 316 appears to decline in rate and eventually vanish. There may be some relationship between this phenomenon and that of changes in failure mode that also appear to be related to swelling.

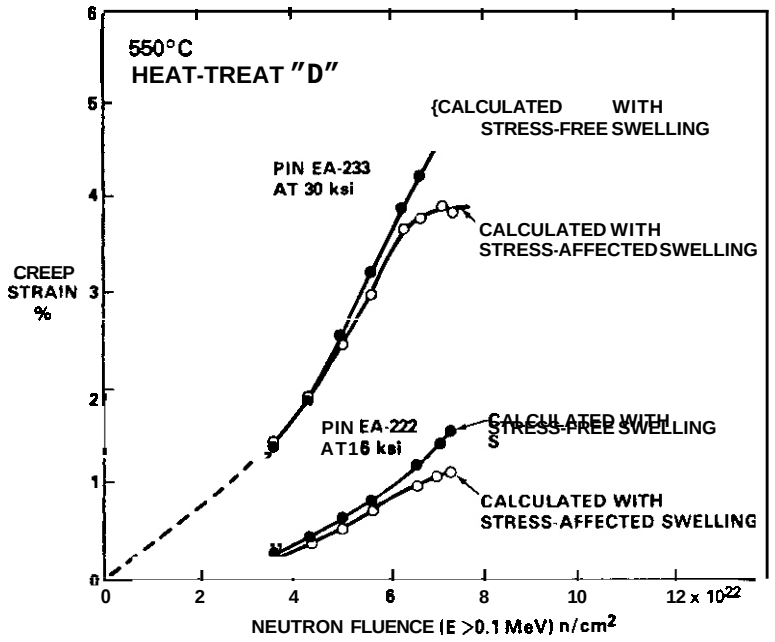

FIGUKE 8. Calculated creep strains for two pins shown in Figure 7, showing how the use of stress-free swelling camouflages the onset of the third major stage of creep.

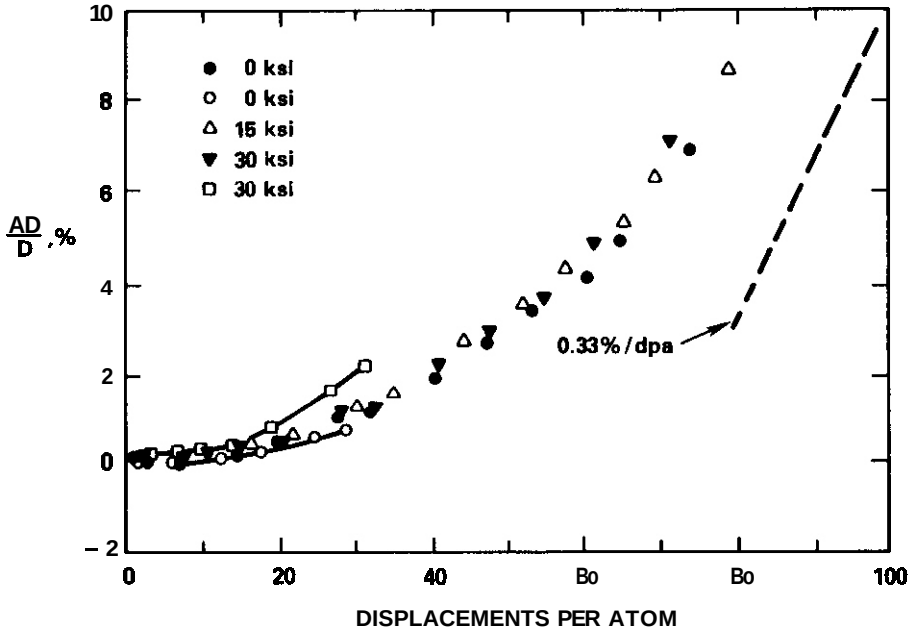

FIGURE 9. Creep Strains observed in annealed AISI 316 tubes irradiated at 550°C in EBR-II. All of these pins were found to have lost their gas pressure somewhere prior to their final examination.

6.0 References

1. F. A. Garner, J. Nucl. Mater. 122 & 123 (1984) 459.

2. K. Ehrlich, J. Nucl. Mater. 100 (1981) 149.

3. J. L. Boutard, Y. Carteret, R. Cauvin, Y. Guerin and A. Maillard, Proceedings of Conference on Dimensional Stability and Mechanical Behavior of Irradiated Metals and Alloys, Brighton, England (1983) Vol. I., 109.

4. B. J. Makenas, Effects of Radiation on Materials: Twelfth International Symposium, ASTM STP 870, F. A. Garner and J. S. Perrin, Eds., (1985) 202.

5. F. A. Garner, H. R. Brager, M. L. Hamilton, R.A. Oodd and 0. L. Porter, "New Oevelopments in Irradiation-Induced Microstructural Evolution of Austenitic Alloys and Their Consequences on Mechanical Properties," Hanford Engineering Development Laboratory Report HEOL-SA-3353, August 1985, submitted for publication in Radiation Effects.

6. F. A. Garner and D. L. Porter, Effects of Radiation on Materials: Eleventh Conference, ASTM STP 782, H. R. Brager and J. S. Perrin, Eds., (1982) 295.

7. 0. L. Porter and F. A. Garner, in ref. 4, pp. 212-220.

8. W. G. Wolfer, J. Nucl. Mater. 90 (1980) 175.

9. 0. S. Gelles, in ref. 4, pp. 98-112.

10. 0. S. Gelles, F. A. Garner and B. L. Adams, Damage Analysis and Fundamental Studies quarterly Progress Report, DOE/ER-0046/11 (August 1982) 81.

11. H. R. Brager, F. A. Garner and G. L. Guthrie, J. Nucl. Mater. 66 (1977) 301.

12. 0. S. Gelles, F. A. Garner and H. R. Brager, Effects of Radiation on Materials: Tenth Conference, ASTM STP 725, D. Kramer, H. R. Brager and J. S. Perrin, Eds., (1981) PP. 735-753.

7.0 Future Work

This effort will continue, particularly in the area of possible relationships between swelling, creep and ex-reactor deformation.

8.0 Publications

None

CHAPTER 5

RADIATION EFFECTS MECHANISMS AND CORRELATIONS

A COMPOSITE MODEL OF MICROSTRUCTURAL. EVOLUTION IN AUSTENITIC STAINLESS STEEL UNDER PAST NEUTRON IRRADIATION

R. E. Stoller (Oak Ridge National Laboratory) and G. R. Odette (university of California, Santa Barbara)

1.0 Objective

To develop a comprehensive model of the microstructural evolution of austenitic stainless steels under the irradiation conditions typical of a D-T fusion reactor first wall.

2.0 *Summary*

A rate-theory-based model has been developed which includes the simultaneous evolution of the dislocation and cavity components of the microstructure of irradiated stainless steels. Previous work has generally focused on developing models for void swelling while neglecting the time dependence of the dislocation structure. These models have broadened our understanding of the physical processes that give rise to swelling, e.g., the role of helium and void formation from critically-sized bubbles. That work has also demonstrated some predictive capability by successful calibration to fit the results of fast reactor swelling data. However, considerable uncertainty about the values of key parameters in these models limits their usefulness as predictive tools. Hence the use of such models to extrapolate fission reactor swelling data to fusion reactor conditions is compromised.

The present work represents an effort to remove some of these uncertainties by self-consistently generating the time dependence of the dislocation structure, both faulted loops and network dislocations. The model's predictions reveal the closely coupled nature of the evolution of the various microstructural components and generally track the available fast reactor data in the temperature range of 350–700°C for doses up to 100 dpa. As the theoretical model has become more complex, parameter choices began to be constrained to a more limited range of values in order to obtain this agreement between theory and experiment. While the model remains approximate in many respects, it should ultimately provide a more ueeful tool for understanding microstructural evolution under irradiation and permit more confident predictions of void swelling in future fusion reactors.

3.0 Program

Title: Radiation Effects Mechanisms
Principal Investigator: L. K. Mansur
Affiliation: Oak Ridge National Laboratory

Title: Damage Analysis and Fundamental Studies far Fusion Reactor Materials Development
Principal Investigators: G. R. Odette and G. E. Lucas
Affiliation: University of California, Santa Barbara

4.0 Relevant DAFS Program Plan/Subtask

Subtask II.C.1.2 Effects of Material Parameters on Microstructure — Modeling and Analysis
Subtask II.C.16.1 Composite Correlation Models and Experiments — Correlation Model Development
Subtask II.C.18.3 Relating Low and High Exposure Microstructures — Modeling and Analysis

5.0 Accomplishments and Status

5.1 Introduction

The task of predicting the observable effects of neutron irradiation of stainless steel is hindered by the complex interactions of numerous microscopic phenomena (I). A rigorous treatment requires that one consider the simultaneous evolution of the various microstructural features and microchemical effects such as

solute segregation and irradiation induced phase instabilities. Parameters such as effective pint defect biases are difficult to quantify precisely, yet they play a major role in determining the nucleation and growth rates of the various extended defects.

Development of theoretical models is further hindered by an incomplete data base and large heat-to-heat variations in microstructural data. Such variations may in part be related to effects such as reactor duty cycle differences during various experiments or uncertainties in the temperature, flux. and fluence at which the experiment was conducted. However, type 316 stainless steel has also shown a significant sensitivity to subtle changes in minor alloying elements (e.g, carbon, titanium, and silicon) (2) and details of thermo-mechanical treatment. Such sensitivity increases the uncertainty in determining values for certain critical physical parameters, such as "effective" diffusion coefficients and the recombination coefficient. Further, model predictions are not unique in that different sets of mechanisms and parametere can result in "reasonable" agreement with the data. This is particularly a problem if interpretation of limited data sets, containing intrinsic uncertainties. are interpreted in terms of single or few mechanisms. Unfortunately such interpretations are often further compromised by only qualitatively considering the underlying mechanisms and by failing to consider the statistical significance of so-called data trends. Single mechanism models can be very important in developing an understanding of individual processes; however, they can justifiably be applied in quantitative analysis only if both rigorous control over experimental variables is maintained and if it can be shown that the interaction of multiple mechanisms is not important. This is not often the case in practice. However, empirical approaches may still provide an engineering expedient for data correlation and some limited extrapolation of data.

More complex quantitative models allow for competition and interaction of mechanisms which have been identified, but they suffer from the proliferation of non-unique parameters as noted above. Hence, they are most effective as analytical tools only if the possible ranges of parameter combinations are identified and considered in any extrapolation. Two important components of any data analysis effort are the explicit recognition of the likely non-uniqueness of any single calibration and a quantitative effort to ascertain the consequences of this in extrapolated predictions. This general problem has been discussed In some detail previously (1).

The model described below is part of an overall effort to develop a quantitative understanding of microstructural evolution in irradiated alloys. The model focuses an the coupled evolution of the major microstructural features observed in irradiated austenitic stainless steels; bubbles, voids, faulted dislocation loops and network dislocations. The effects of second phase precipitate particles are included to a limited degree. The effects of microchemical evolution, which is known to occur and is likely to be of importance, are not explicitly treated. However, the influence of microchemical evolution is approximately accounted for in the various rate theory parameters. The major approximation here is in the use of material parameters (e.g, biases and diffusivities) which are not altered to reflect either spatial or temporal fluctuations in the alloy composition.

5.2 Description of the Model

The model developed here is an extension of previous work which examined primarily the evolution of the cavity wmponent of the irradiated microstructure (3-7). That work helped to establish the generally accepted sequence of events which lead to void swelling; viz., that bubbles nucleate and slowly grow by accumulating both vacancies and helium until they reach a critical size, r^*, which is determined by the vacancy supersaturation, S, the material parameters Y, the surface energy and Ω, the atomic volume and temperature, T.

$$r^* = f(\ell n\ S)\ \frac{\gamma\Omega}{kT\ \ell nS} \qquad (1)$$

The function $f(\ell n\ S)$ is a non-ideal gas correction factor (7); for an ideal gas f = 4/3. After reaching this critical size the bubbles are converted to voids and begin to grow primarily by vacancy accumulation. Similar work by others has also confirmed this general scenario (8-10). Since references b and 7 describe the cavity evolution model in detail, it will not be discussed further here.

5.2.1 Calculation of Point Defects

The approach used to calculate the point defect concentrations follows the familiar rate theory (6,11). The conventional rate equations which describe the vacancy and interstitial concentrations are slightly modified due to the dislocation evolution models. The following assumptions are implicit in the mathematical description:

1. The concentrations of vacancies and mono-, di-, tri-, and tetra-interstitials are calculated as if they were at steady state during a given time step.

2. Only the mono-defects are mobile. Mobility of small clusters has been shown to have no significant effect on the point defect calculations (12). A relatively high interstitial migration energy (0.85 eV) is used. This value is consistent with recent measurements of this parameter in austenitic steels (13,14). Solute-interstitial trapping could account for this value.

3. The tetra-interstitial is the stable nucleus for faulted loop growth. The di- and tri-interstitials may thermally dissociate by emitting single interstitials.

4. The point defect sinks included are bubbles, voids, subgrain structure, transient vacancy clusters in the form of microvoids as a result of cascade collapse, network dislocations and Frank faulted loops. The sink strengths are calculated using a first order effective medium approach as described previously (6). The faulted loop and network dislocations preferentially absorb interstitials; all other sinks are unbiased.

The rate equations then are:

$$\frac{dC_v}{dt} = G_v - \beta^2 C_2 - \beta^3 C_3 - \beta^4 C_4 - \alpha C_i C_v - D_v C_v (S_v^n + S_v^\ell + S_v^c + S_v^{vcl} + S_v^g) \tag{2}$$

$$\frac{dC_i}{dt} = \eta G_{dpa} + C_2(2r_d^2 + \beta_v^2 - \beta_i^2) + C_3^d(r_3 - \beta_i^3) - \beta_i^1 C_1 - \beta_i^4 C_4$$

$$- \alpha C_i C_v - D_i C_i (S_i^n + S_i^\ell + S_i^c + S_i^{vcl} + S_i^g) \tag{3}$$

$$\frac{dC_2}{dt} = \beta_i^1 \frac{C_i}{2} + C_3(\beta_v^3 + r_3^d) - C_2(\beta_v^2 + \beta_i^2 + r_2^d) \tag{4}$$

$$\frac{dC_3}{dt} = \beta_i^2 C_2 + \beta_v^4 C_4 - C_3(\beta_v^3 + \beta_i^3 + r_3^d) \tag{5}$$

$$\frac{dC_4}{dt} = \beta_i^3 C_3 - \beta_v^4 C_4 - C_4 \tau_4^{-1} \tag{6}$$

In Eqs. (2-6) C_2, C_3, and C_4 are concentrations of di-, tri-, and tetra-interstitials, the $\beta_{i,v}^j$ and $r_{2,3}^d$ are rate constants for the impingement of point defects on interstitial clusters of size j and the thermal dissociation of di- and tri-interstitials, respectively, $S_{i,v}^e$ is the faulted loop sink strength and τ_4 will be discussed below. The other terms have their normal meaning (see Table 1).

$$\beta_{i,v}^j = \frac{z_{i,v} D_{i,v} C_{i,v}}{a_o^2} \tag{7}$$

$$r_{2,3}^d = \frac{D_i}{a_o^2} \exp\left(-\frac{E_{2,3}^b}{kT}\right) \tag{8}$$

$$S_{i,v}^\ell = \frac{2\pi}{\ell n(r_o/r_c)} \sum_j 2\pi r_j N_j Z_{i,v}^\ell(r_j) \tag{9}$$

TABLE 1. VARIABLE DEFINITIONS

Parameter	Value/Units
Lattice parameter, a_o	3.58×10^{-10} m
Atomic volume, Ω	1.15×10^{-29} m^3 $(a_o^3/3)$
Network dislocation Burgers vector, b_d	2.53×10^{-10} m $(a_o/\sqrt{2})$
Faulted loop Burgers vector, b_ℓ	2.07×10^{-10} m $(a_o/\sqrt{3})$
vacancy diffusivity, D_v	m^2/sec
Interstitial diffusivity, D_i	m^2/sec
Vacancy concentration, C_v	#/atom
Thermal equilibrium vacancy concentration, C_v^e	#/atom
Interstitial concentration, C_i	#/atom
Di-interstitial concentration, C_2	#/atom
Tri-interstitial concentration, C_3	#/atom
Tetra-interstitial concentration, C_4	#/atom
Extended defect sink strengths, $S_{i,v}^j$	m^{-2}
Extended defect equilibrium vacancy concentrations, C_v^j	#/atom

where: j = c for cavities

= n for network dislocations

= ℓ for faulted loops

= g for subgrains

= vol for microvoids

The $z_{i,v}^{\ell}(r)$ are faulted loop bias factors for interstitials and vacancies and r_c and r_o are the dislocation core radius and the outer Cutoff radius. respectively. The Outer cutoff radius is taken as the mean dislocation spacing, $r_o = (\pi\rho_n)^{-1/2}$, and the core radius is twice the Burgers vector, $r_c = 2b_\ell$ (16,17). Values for the binding energy of the second and third interstitial in a cluster $(E_{\ell,3}^b)$ and for the combinatorial numbers $(z_{i,v}^j)$ in Eq. (10) are given in Table 2. The choice of these values will be discussed below.

The vacancy generation rate is computed by summing the contributions from each sink type (S_j),

$$G_v = nG_{dpa}(1 - \chi) + D_v \sum S_j C_v^j \qquad (10)$$

The C_v^j in Equation (10) are the vacancy concentrations in equilibrium with the appropriate sink. These have been given previously (6) with the exception of C_v^ℓ, the value for faulted loops.

$$C_v^{\ell}(r) = C_v^e \exp\left[-\frac{\Omega}{kT}\left(\frac{G_s b_\ell}{4\pi(1-\upsilon)r}\ln\left(\frac{4r}{b_\ell}\right) + \frac{\gamma_{sf}}{b_\ell}\right)\right] \qquad (11)$$

TABLE 2. TYPICAL MATERIAL AND INPUT PARAMETERS

Parameter	Value
vacancy migration energy, E_v^m	14 eV
Vacancy formation energy, E_V^f	16 eV
Interstitial migration energy, E_i^m	0.85 eV
Di-interstitial binding energy, E_2^b	1.35 eV
Tri-interstitial binding energy, E_3^b	1.75 eV
Helium-divacancy binding energy, E_H^b	0.5 eV
Vacancy diffusivity pre-exponential, D_V^o	8.0×10^{-5} m^2/sec
Interstitial diffusivity pre-exponential, D_i^o	8.0×10^{-6} m^2/sec
Recombination coefficient, α	2×10^{17} D_i sec^{-1}
Displacement rate, G_{dpa}	1×10^{-6} dpa/sec
Helium generation rate, G_{He}	3.50×10^{-13} He/atom/sec
Cascade efficiency, η	0.333
Fraction of cascade vacancies collapsed into microvoids, χ	0.6
Interstitial/vacancy combinatorial number	$Z_i^1 = 63$ $Z_v^2 = 33$
far interstitial clusters	$Z_i^2 = 90$ $Z^3 = 38$
	$Z_i^3 = 110$ $Z_v^4 = 42$
	$Z_i^4 = 130$
Surface free energy, γ	$3.24 - 1.4 \times 10^{-3}$ T(°C) J/m^2
Stacking fault energy, γ	1.5×10^{-2} J/m^2
Initial dislocation density, $\rho_n(0)$	3.0×10^{15} m^{-2} - 20% cold worked
Network dislocation/interstitial bias, Z_i^n	1.25
Faulted loop/interstitial bias, Z_i^a	1.50
Subgrain size, d_g	$T \leq 500$°C 1.0×10^{-6} m
	= 550 1.25×10^{-6} m
	= 600 3.0×10^{-6} m
	= 650 7.75×10^{-6} m
	= 700 1.70×10^{-5} m
Hicrovoid radius, r_{mv}	T = 350°C 7.0×10^{-10} m
	= 400°C 7.5×10^{-10} m
	$\geq$ 450°C 8.0×10^{-10} m
Total cavity density, N_c^t	2.53×10^{26} exp(-0.023 T(°C)) m^{-3}
Precipitate associated cavity fraction, f_p	0.1
Precipitate sink strength, S_p	4×10^{14} m^{-2}
Precipitate nucleation time, τ_P	0.16 (700 - T(°C)) dpa
	Matrix / Precipitate-associated
Cavity volume factor, $3F_V(\beta)/4\pi$	1.0 / 0.40
Cavity surface area factor, $F_s(\beta)/4\pi$	1.0 / 0.434
Lattice parameter, a_o	3.58×10^{-10} m
Atomic volume, Ω	1.15×10^{-29} m^3 ($a_o^3/3$)
Network dislocation Burgers vector, b_d	2.53×10^{-10} m ($a_o/\sqrt{2}$)
Faulted loop Burgers vector, b_ℓ	2.07×10^{-10} m ($a_o/\sqrt{3}$)
Thermal dislocation evolution parameters source density, S_D	$T \leq 550$°C 2.0×10^{21} m^{-3}
	= 600°C 9.7×10^{20} m^{-3}
	= 650°C 1.2×10^{20} m^{-3}
	= 700°C 2.0×10^{19} m^{-3}
Modified back stress term, A	0.05

The first term in the exponential in Eq. **(11)** is the elastic energy opposing loop growth due to the increasing dislocation line length while the second term is due to the stacking fault; G_s is the shear modulus **(15)**, υ is Poisson's ratio, γ_{sf} is the stacking fault energy and b_ℓ is the Burgers vector ($b_\ell = a_o/\sqrt{3}$).

5.2.2 Faulted Loop Evolution

The present model distinguishes between the small interstitial clusters and the larger faulted loops by treating their evolution differently. The τ_4 term in Eq. (6) is the lifetime of a tetra-interstitial against growth to the size of the first faulted loop size **class.** If r_4 is the radius of the tetra-interstitial and r_1^ℓ is the radius of loops in the first size class,

$$\tau_4 = \int_{r_4}^{r_1^\ell} \left(\frac{dr_\ell}{dt}\right)^{-1} dr \tag{12}$$

$$\frac{dr_\ell}{dt} = \frac{A}{b_\ell}\left[Z_i^\ell(r_\ell)D_iC_i - Z_v^\ell(r_\ell)D_v(C_v - (C_v^\ell(r_\ell))\right] \tag{13}$$

in which $A = 2\pi/\ell n(r_o/r_c)$ and C_v^a is given by Equation (11).

The use of the term $C_4\tau_4^{-1}$ in Eq. *(6)* permits a transition between regions in which alternate descriptions of interstitial loop evolution are used. As shown in Eqs. **(4-6),** a discrete clustering calculation is done for sizes up to the tetra-interstitial. However. this description would necessitate integrating greater than 10^4 rate equations if it were used for loops up to the maximum size observed experimentally. The evolution of the larger loops is instead given by equations of the form

$$\frac{dN_i^\ell}{dt} = N_{i-1}\tau_i^{-1} - N_i\tau_{i+1}^{-1} \tag{14}$$

where N_i^ℓ is the number of loops in a given size class with radius r_i^a and the τ_i are given by Eq. (12) with the appropriate **radii** used **as** the limits of the integration. The loop size distribution between r_4 and the maximum loop radius is divided into a histogram which preserves the essential features of the distribution. The number of size classes required can be determined numerically. Figure 1 is a plot of the loop density

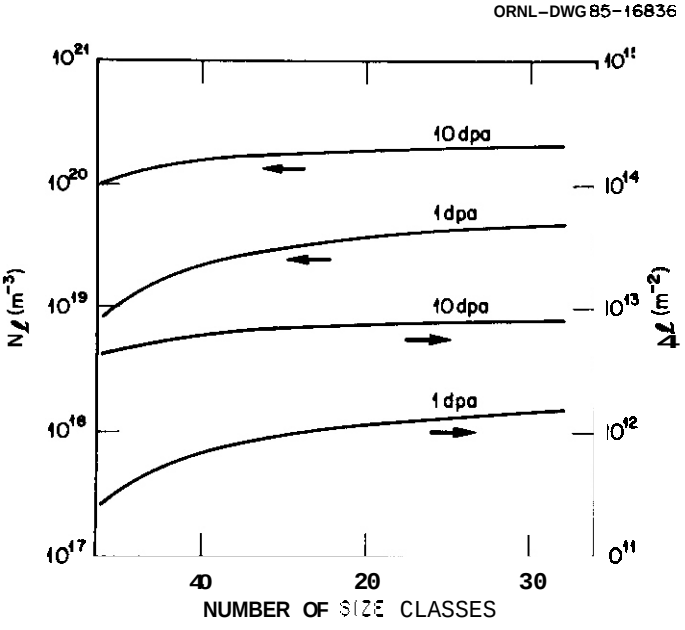

FIGURE 1. Faulted Loop Density (N_L) **and** Loop Line Length (ρ_L) as a Function of the Number of Loop Size Classes.

and loop line length at 450°C as a function of the number of size classes used. These parameters are essentially independent of the number of size classes when greater than about 15 are used.

It remains to be shown that Eq. *(6)* provides a numerically appropriate boundary condition between the two regions. This can be done by comparing the net forward current (J_+) from Eq. **(6)** with a more **rigorous** calculation based on the continuity equation. The continuity equation yields the following result:

$$\frac{\partial}{\partial t}(n(r)) = -\frac{\partial}{\partial r}(\dot{r}n(r)) \tag{15}$$

$$\frac{-\dot{r}(r + \delta r)n(r + \delta r) + \dot{r}(r)h(r)}{\delta r}$$

If $r = r_4$, $r + \delta r = r_5$, $n(r) = C_4$ and $n(r + \delta r) = C_\ell$; then Eq. (15) yields:

$$J_+ = \frac{\dot{r}(C_4)C_4}{\delta r} \tag{16}$$

$$J_+ = \frac{C_4 b_\ell}{A(r_5 - r_4)} [Z_i^\ell(r_4)D_i C_i - Z_v^\partial(r_4)D_v(C_v - C_v^\ell(r_4)] \tag{17}$$

where Eq. (13) bas been substituted for $\dot{r}(C_4)$. Alternately, J_+ from Eq. *(6)* is given by $C_4\tau_4^{-1}$.

$$C_4\tau^{-1} = C_4 / \frac{A}{b_\ell}\int_{r_4}^{r_1^\ell}[Z_i^\ell(r)D_i C_i - Z_v^\ell(r)D_v(C_v - C_v(r))]^{-1}\,dr \tag{18}$$

$$C_4\tau_4^{-1} = \frac{C_4 b_\ell}{A}\frac{1}{(r_1^\ell - r_4)}[Z_i^\ell(r_4)D_i C_i - Z_v^\ell(r_4)D_v(C_v - C_v^\ell(r_4)] \tag{19}$$

where the integral **has** been approximately evaluated by the values of the integrand at the lower limit times dr. In the limit as r_1^∂ approaches r_5 (the radius of the penta-interstitial), Eqs. (17) and (19) are equal by inspection. This equality is subject to the assumption that the integrand in Eq. (18) is only a weak function of r. This condition is met by noting that $D_V C_V^\partial(r) = 0$ for small loops and that in the present model the biases are not size dependent for the smallest loops. Finally, it is worth noting that the values in Fig. 1 for **32** size classes correspond to the **case** where $r_1^\ell = r5$.

5.2.3 Network Dislocation Evolution

The model for the evolution of the dislocation structure includes four components, two of which are solely due to the irradiation and two of which are thermal. The thermal components are a high temperature climb source term (Bardeen-Herring sources) and a thermal annihilation term due to stress-assisted directional diffusion of vacancies. Models of this type have been developed for the study of creep processes **(18,19).** Network dislocations can be recovered by climb and glide processes leading to annihilation. The present model assumes that climb is the rate controlling process. The climb velocity of an edge dislocation subject to a stress, a, is given by Nix et. al, (20) as

$$v_{cl} = \frac{2\pi}{\ell n(r_o/r_c)}\frac{\Omega}{bKT}D_V C_V^e \sigma \,. \tag{20}$$

Adopting the model of Gibbs (21), the stress is assumed to be an internal (back) stress due to **a** population of immobilized dislocations

$$\sigma = AGb\rho_i^{1/2} \tag{21}$$

where A is nominally 0.4 and ρ_i is the density of pinned dislocations. The average climb distance is taken as the mean dislocation spacing

$$d_{cl} = (\pi\rho_n)^{-1/2} \quad . \tag{22}$$

Using Eqe. (20—22) one obtains a lifetime against annihilations due to this climb-glide process as

$$\tau_{th} = \frac{d_{cl}}{v_{cl}} = \left[A' \frac{2\pi^{3/2}}{\ell n(r_o/r_c)} \frac{\Omega G D_v C_v^e}{kT} \rho_n\right]^{-1} \quad . \tag{23}$$

In Eq. (23) $A\rho_i^{1/2}$ has been set to $A'\rho_n^{1/2}$ and the parameter A' was used to fit thermal recovery data.

The Bardeen-Herring sources for network dislocations are similar to the Frank-Read source except that the former are climb driven while the later are glide driven *(22)*. The source is shown schematically in Fig. *2* in which a pinned dislocation segment is bowed due to an applied stress. After climbing a sufficient distance, the source will collapse leaving a dislocation loop and the original line segment once again able to generate succeeding loops. For simplicity, the source may be assumed to generate $2\pi L$ of new dislocation line length after climbing a distance L. The climb velocity is given by Eq. (20) and the generation rate is then

$$R_{th}^{\rho_n} = \frac{2\pi L}{\tau_{gen}} S_D = \frac{2\pi L v_{th}}{L} S_D \tag{24}$$

$$R_{th}^{\rho_n} = 2\pi v_{th} S_D \tag{25}$$

in which S_D is the source density. In cold worked materials potential sources of this type include not only the dislocation network but also the subgrain structure. The parameter S_D was also used as a fitting parameter.

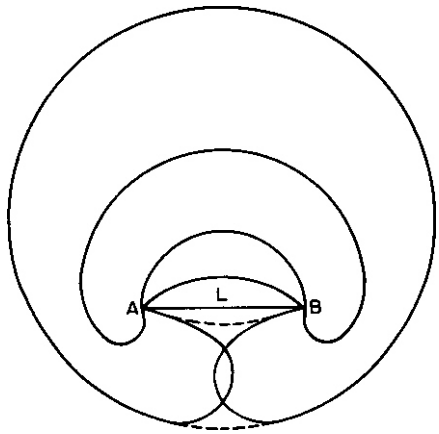

FIGURE 2. Schematic Drawing of Bardeen-Herring Dislocation Source (After Ref. 22).

The thermal dislocation source and annihilation terms Were calibrated using tensile data obtained at 450°, 550°, and 650°C for AISI 316 stainless steel. This data included yield strength measurements *(2%* offset) for both 20% cold-worked and solution annealed material a8 well as *20%* cold worked material aged for *4000* hours at the test temperature (23). Assuming that the hardening increment due to network dislocations varies as $(\rho_n)^{1/2}$ *(24)* and that this is the primary cause of the increased yield strength of the wld-worked material relative to the solution annealed material. the ratios shown in Table 3 are obtained from the data. The model's predictions far these same ratios are also listed. These were obtained by computing the dislocation evolution with $G_{dpa} = \Theta$ in the model.

TABLE 3. RESULTS OF THERMAL DISLOCATION EVOLUTION CALIBRATION.

Dislocation Density Ratio: $\frac{\text{Cold Worked + } 4000 \text{ h at T}}{\text{As Cold Worked}}$

Test Temperature T (°C)	Data	Model
450	0.73	0.99
550	0.41	0.41
650	0.054	0.053

The parameters used to obtain these results are listed below in Table *4*. They are discussed further in the section on Model Predictions.

Under irradiation, the growth and unfaulting of Frank loops provides an additional source of dislocations. The mdel assumes that the maximum loop size is governed by the geometrical constraint that the loop unfaults upon wntacting another loop or network dislocation, hence

TABLE 4. THERMAL DISLOCATION EVOLUTION PARAMETERS

Modified back stress term, A'	0.05	
Source density, s_D	$T \leq 550°C$	2.0×10^{21} m^{-3}
	$= 600°C$	9.7×10^{20} m^{-3}
	$= 650°C$	1.2×10^{20} m^{-3}
	$= 700°C$	2.0×10^{19} m^{-3}

$$r_{unf}^{\ell} = (\pi\rho_t)^{-1/2} \tag{26}$$

where ρ_t is the total dislocation density (25). As the loops grow into this size class, they ace no longer considered Frank loops and a dislocation line length $2\pi r_{unf}^{\ell} N_{unf}^{\ell}$ is added to the dislocation network. The time constant for this process is given by Eq. (12) with the appropriate limits of integration. The rate at which new dislocation line length is generated by this mechanism is:

$$R_{irr}^{\rho n} = 2\pi r_{unf}^{\ell} N_{unf}^{\ell} \tau^{-1} \quad . \tag{27}$$

Network dislocations can also be annihilated by bias driven climb of point defects generated by irradiation. The climb velocity for this process is

$$v_{cl}^{irr} = \frac{1}{b_d} [Z_i^n D_i C_i - Z_v^n D_v (C_v - C_v^n)] \ , \tag{28}$$

where the superscript n denotes the relevant parameter for network dislocations. By similar reasoning which leads to Eq. (23), the dislocation lifetime for this process is

$$\tau_{irr} = \frac{(\pi\rho_n)^{1/2}}{b_d} [Z_i^n D_i C_i - Z_v^n D_v (C_v - C_v^n)] \quad . \tag{29}$$

The lifetimes given in Eqs. (23) and (29) are added using an electrical resistance analog to yield the total lifetime of network dislocations.

$$\tau_T = (\tau_{irr}^{-1} + \tau_{th}^{-1})^{-1} \quad . \tag{30}$$

This finally leads to a rate equation describing the evolution of the dislocation network as

$$\frac{d\rho_n}{dt} = 2\pi(v_{th} S_D + r_{unf}^{\ell} N_{unf}^{\ell}) - \rho_n \tau_T^{-1} \tag{31}$$

5.3 Kodel Predictions and Comparison with Data

5.3.1 Parameter Choices

There are at least two general goals in developing models such as have just been described. One is to try to develop an understanding of the important physical processes which lead to microstructural evolution under irradiation and the other is to ultimately provide some predictive capability. The satisfaction of both of these goals is frustrated by a lack of well known material parameters for austenitic stainless steel. In some cases, measurements made on pure metals can be used to provide initial estimates, but key parameters are known to be sensitive to alloy composition and perhaps impurities (11,12,26–29). Although simple void swelling models have been successfully used to explain much of the available swelling data and have provided considerable insight into the mechanisms responsible for this phenomenon (3–9), the ability to do predictive work with these models is compromised by uncertainty about parameter values. For example, when bulk recombination is ignored and dislocations are the major point defect sink, the vacancy supersaturation takes the following simple form (5).

$$S = \frac{\eta G_{dpa}}{S_i D_v C_v^n}(Z_i^n - 1) \qquad (32)$$

Values of the cascade efficiency (η) between 0.1 and 1.0 have been used by various workers (6,9,30) and values of the interstitial/dislocation bias (Z_i) have varied between -1.02 to > 1.5 (6,31,32). Depending on the values chosen for these two parameters, the computed supersaturation can vary significantly.

The parameters which have been used to compute the results given below are listed in Tables 2 and 4. The initial choice for most of these parameters was the value used previously (6); these values generally fall within the range of what might be termed "typical" for the void swelling models which have been referred to above. A notable exception is the relatively high activation energy for interstitial diffusion. Measurements of E_i^m in pure metals have indicated a lower value, <0.5 eV (30). Such a value has normally been used in void swelling models already discussed; however, the results obtained from these models are not sensitive to the value of E_i^m (34). The results obtained with the present model are dependent on E_i^m via its influence on the predicted faulted loop population and their subsequent effect on network dislocation density. The value of E_i^m given in Table 3 is in agreement with recent measurements of this parameter in austenitic steels (13,14). The fact that the model requires such a value is encouraging. As the model became more complex, through the introduction of additional physical mechanisms, more parameters were introduced as a result. However, the model also became somewhat "stiffer" with respect to arbitrary parameter choices. The example, reference to Eq. 32 indicates that relative changes in Z_i^n and η can be used to offset one another in a simple model. This is no longer the case in the present model since the various sinks have different dependencies on these parameters. The cavity and dislocation evolution are not independent but are coupled in a complex way via their mutual effect on the point defect concentrations.

There are several parameters used in the present work which have not been included previously. These include the thermal dislocation evolution parameters in Equations 21–25 and the parameters used in the rate equations for interstitial clusters. Equations (2–6, 9–11). The choice of the values for interstitial clustering parameters was guided by the results of more detailed nucleation calculations (12,35,36). The model's predictions are not too sensitive to the values of the combinatorial numbers while the di- and tri-interstitial binding energies affect primarily the temperature dependence of the faulted loop density. The predicted dislocation density is sensitive to the thermal dislocation evolution parameters (Table 2) only for temperatures above about 550°C when faulted loops cease to contribute significantly to the dislocation network. To a first approximation, the source density, S_D, should be about equal to L^{-3} where L is the mean spacing of dislocation pinning points. If other dislocations provide the primary pinning sites, then L should be roughly proportional to ρ_n^{-2}. In this case, the maximum and minimum values of S_D given in Table 3 would correspond to pinned dislocation densities of 1.6×10^{14} and 7.4×10^{12} m^{-2}.

5.3.2 Model Predictions

The results given here were obtained using the parameter values given in Tables 1,2 and 4 and using a computational method discussed previously (6). The parameters have not been thoroughly optimized to date but the overall behavior of the model is very encouraging.

Predicted values for void swelling, network dislocation density and faulted loop density are shown in Figure 3, a-c as a function of temperature at two doses for 20% cold-worked material. A comparison with fast reactor data is provided in Figs. 4–6. Values of these key microstructural features are well tracked by the model over this fairly broad temperature ranges. The swelling data shown in Fig. 4 is from the RS-I experiment in the Experimental Breeder Reactor-II (EBR-II) (37,38). This experiment included several heats of AISI 316 stainless steel which had been developed to meet the specifications for components in the first core of the Fast Flux Test Facility (FFTF). The temperatures shown in Fig. 4 reflect a downward revision from the original design temperatures (39). The model predicts both incubation times and peak swelling rates (~1%/dpa in the peak swelling region) which are similar to the data. The model predictions of swelling at temperatures greater than 650°C in Fig. 3a are also consistent with recent observations (38).

There is much less data with which to compare the model's predictions of dislocation and faulted loop densities. Figure 5 compares dislocation densities at 30–40 dpa for M316 stainless steel irradiated in the Dounreay Fast Reactor (DFR) in Great Britain (40) with those from the model at 40 dpa. The agreement is quite good. The results are also consistent with reported values far AISI 316 stainless steel irradiated

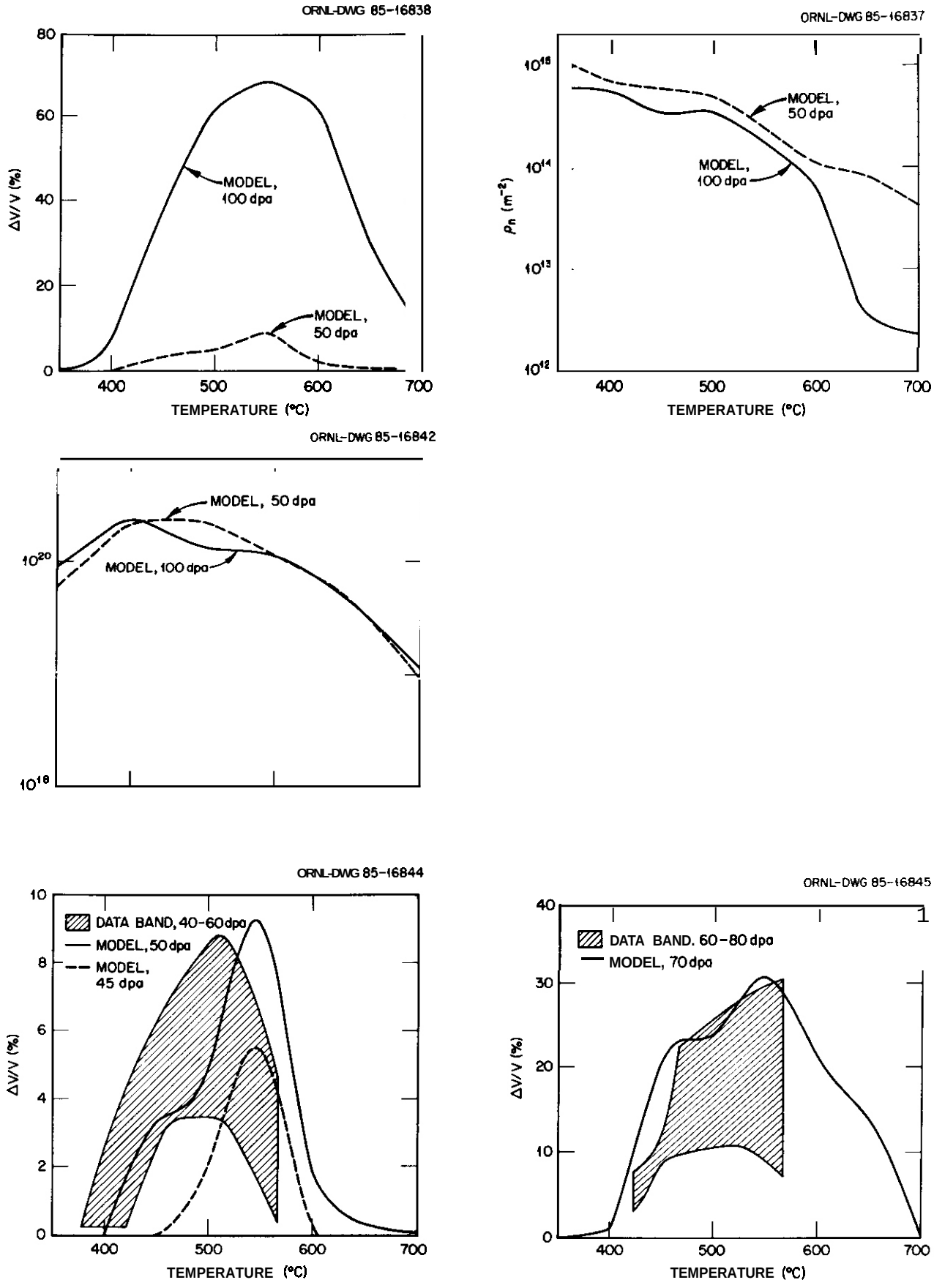

FIGURE 4. Comparison of Predicted Swelling and Fast Reactor Data at an Intermediate and High Fluence (37,38).

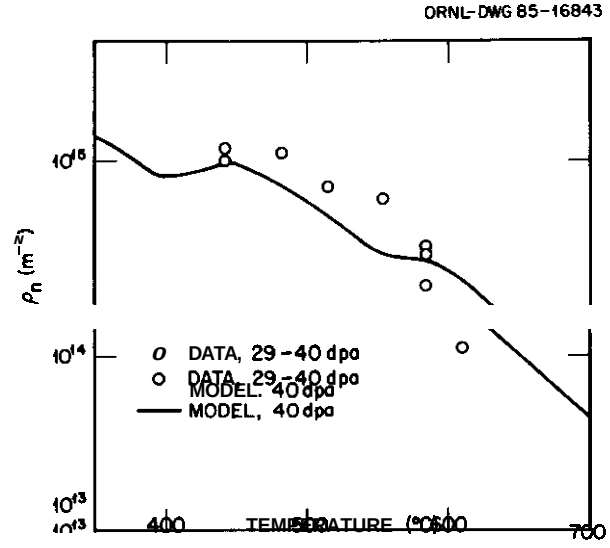

FIGURE 5. Comparison of Predicted Network Dislocation Density and Fast Reactor Data at 40 dpa (Ref. 40).

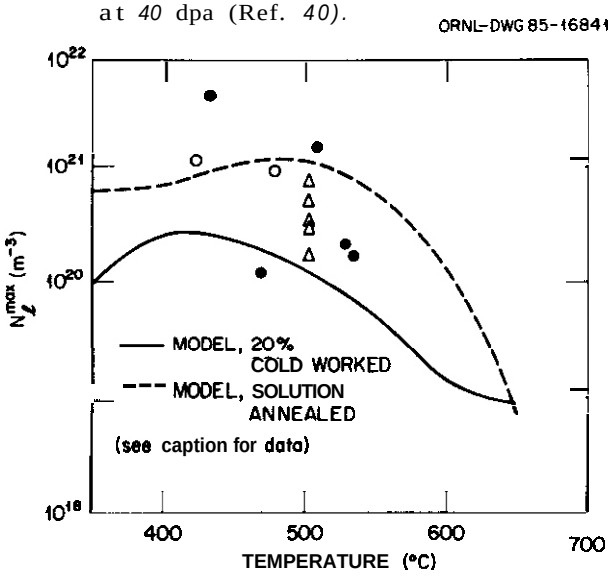

FIGURE 6. Comparison of Predicted Faulted Loop Density and Low Fluence Fast Reactor Data. (Δ Ref. 25, ● Ref. 42, o Ref. 43).

in the EBR-II (41). Predicted faulted loop densities are compared with data from several sources in Fig. 6. The data are for AISI 316 stainless steel irradiated in both the solution annealed and cold-worked conditions at doses between about 6 and 16 dpa (25,42-43). The data from Ref. 25 also reflect varying stress levels. The predicted curves reflect the peak faulted loop density far both solution annealed and 20% cold worked starting conditions. The data is reasonably well fitted by the predictions except at low temperatures where the loop density is somewhat low.

The fluence dependence of the mdel predictions at 500°C is shown in Fig. 1a and 7b for 20% cold worked and solution annealed material, respectively. The coupling of the evolution of the various microstructural features is clearly seen. After an initial transient the microstructure reaches a state which is independent of the initial condition. The incubation time for swelling is not primarily associated with the dislocation transient but rather with the time required for the cavities to accumulate the critical number of helium atoms (3-6). Following the initiation of void swelling, the dislocation structure undergoes some additional recovery as the cavity sink Strengths begins to increase. Although it is not shown in Fig. 7, at high doses the swelling rate begins to decrease at the cavity sink strength exceeds the dislocation sink strength (44). The precise coincidence of the values for the solution annealed and cold-worked material at such low doses may be somewhat artificial. The model does not include an explicit cavity nucleation calculation and the same initial cavity densities were used far both materials. Some data indicates that void densities at low doses are higher for solution annealed material (43) and neglecting this difference may influence the model's predictions at low doses.

The evolution towards a saturation microstructure has been observed (45,46) and has been discussed elsewhere (1). The predicted low dose peak in the faulted loop number density in solution annealed material has also been observed (43); however, Brager and Straalsund have reported similar high values at low doses in 20% cold worked stainless steel (47) in conflict with the predictions shown in Fig. 7. While the initial recovery of the network dislocation density in the 20% cold-worked material appears to be in agreement with the available data (45,47), the initial transient appears to occur too quickly in the solution annealed material (45). The thermal dislocation source term may be the cause of the too rapid buildup of the network dislocation density for the solution annealed simulation. The source density (S_D) values were developed for 20% cold-worked material and implicitly reflect a near steady state value far the network dislocation density as discussed above. Hence for the solution annealed material, the values of S_D may be too high at low doses. Explicit dislocation density dependence in S_D may be required to improve the agreement with the solution annealed data.

5.4 Summary

The theoretical model described herein provides a vehicle for studying the evolution of the important microstructural features in fast neutron irradiated stainless steel. A prominent feature of the model is a new description of dislocation evolution in which Frank faulted loops nucleate, grow, and unfault to provide a source for network dislocations while network dislocations are simultaneously annihilated by climb/glide processes. Faulted loop evolution is simulated using a novel scheme in which discrete cluster equations are used to describe the smallest loops and a discretized continuum distribution is used to describe the larger loops. This scheme greatly reduces the number of equations necessary to describe the loop distribution. The model also includes components which describe the evolution of the dislocation

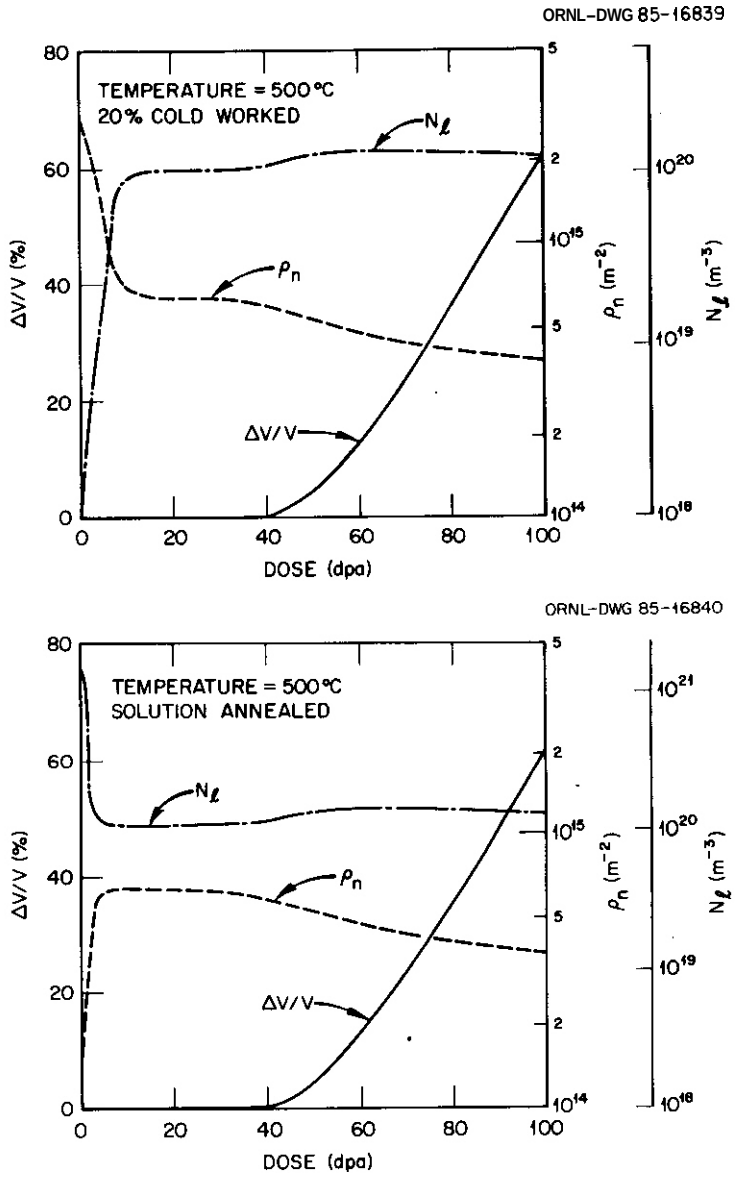

FIGURE 7. Dose Dependence of Predicted Swelling, Network Dislocation Density, and Faulted Loop Density at 500°C for 20% Cold Worked and Solution Annealed Material.

network in the absence of irradiation. This dislocation evolution model has been linked With a previously developed model of cavity evolution which had been used to analyze the problem of void swelling (4,6).

The predictions of the model indicate that the individual features do not evolve independently but are coupled via their mutual influences on the point defect concentrations. Although the model incorporates the time dependence of only three major microstructural components (cavities, faulted loops, and network dislocations), good agreeoent has been obtained with a variety of experimental data. It was encouraging to note that as more microstructural features were added to the current model, the parameter space in which one could obtain "reasonable" results became more limited. Even fairly small changes in parameters such as certain of the activation energies could not be accommodated without significantly altering the predictions. This appears to indicate the robustness of the rate theory as a tool for investigating radiation effects and suggests that the relative importance of microstructural evolution may he greater than that of effects such as microchemistry (48). While microchemical changes are known to occur. their effect may he obscured globally by the use of the various rate theory parameters which are effective averages over times and distances greater than the scale of the microchemical variations. In such a case the role of microchemistry may be primarily to influence microstructural evolution.

6.0 References

1. G. R. odette, J. Nucl. Hater. 85&86 (1979) 533—545.

2. H. R. Rrager and F. A Garner, "Dependence of Void Formation in Phase Stability in Neutron Irradiated Stainless Steel," Effects of Radiation on Structural Materials: Ninth Int. Symp., ASTM STP 683, ASTM, 1979, 207–232.

3. G. Q. Odette and S. C. Langley, Radiation Effects and Tritium Technology for Fusion Reactors, CONF-750989. 1975, I: 395—416.

4. R. E. Stoller and G. R. Odette, J. Nucl. Mater. 103—104 (1981) 1361–1365.

5. G. Q. odette and R. E. Stoller, J. Nucl. Mater. 122&123 (1984) 514—519.

6. R E. Stoller and G. R. odette, "The Effect of Helium on Swelling in Stainless Steel: Influence of Cavity Density and Morphology," Effects of Radiation an Materials: Eleventh Int. Symp., ASTM STP 782, ASTY, 1982, 275—294.

7. R. E. Stoller and G. R. Odette, J. Nucl. Mater. 131 (1985) 118-125.

8. L. K. Mansur and W. A Coghlan, J. Nucl. Mater. 119 (1983) 1–25.

9. M. R. Hayns, The Transition From Gas Bubble to Void Growth, AERE-R8806, U.K.A.E.A., 1977.

10. K. C. Russell, Acta Ket. 26 (1978) 1615–1630.

11. A. D. Brailsford and R. Bullough, The Theory of Sink Strengths, AERE Harwell Report TP.854, 1980.

12. R. A. .Johnson, J. Nucl. Mater. 83 (1979) 147–159.

13. O. Dimitrov and C. Dimitrov, J. Nucl. Mater, 105 (1982) 39-47.

14. J. T. Stanley and J. R. Cost, J. Phys. F: Met. Phys. 14 (1984) 1801—1810.

15. Materials Handbook for Fusion Energy Systems. DOE/TIC-10122, U.S. Department of Energy, Office of Fusion Energy.

16. H. Saka, Phil. Mag. 42 (1980) 185—194.

17. J. P. Hirth, and J. Lothe, Theory of Dislocations, McGraw-Hill, New York, 1968.

18. F. K. N. Nabarro, Phil. Mag. 16 (1967) 231–237.

19. J. Gittus, Creep, Viscoelasticity and Creep Fracture in Solids, John Wiley and Sons, New York, 1975.

20. W. D. Nix, R. Gasca-Neri, and J. P. Hirth, Phil. Mag. 23 (1971) 1339—1349.

21. G. B. Gibbs, Phil. Mag, 23 (1971) 771–780.

22 J. Bardeen and C. Herring, Imperfections in Nearly Perfect Crystals, W. Schockley (Ed.), John Wiley and Sons, New York, 1952.

23. D. Fahr, E. E. Bloom, and J. O. Stiegler, "Irradiation Embrittlement and Creep in Fuel Cladding and Care Components." Proc. of BNES Conf., London, 1972, 167–177.

24. G. D. Johnson, F. A Garner, H. R. Brager, and R. L. Fish, "A Microstructural Interpretation of the Fluence and Temperature Dependence of the Mechanical Propertles of Irradiated AISI 316," Effects of Radiation on Materials: Tenth Int. Symp., ASTM STP 725, ASTM, 1981, 393-412.

25. H. R. Brager, F. A. Garner, and G. L. Guthrie, J. Nucl. Hater. 66 (1977) 181–197.

26. W. Assassa and Guialdenq, Met. Sci. 12 (1978) 123—128.

27. S. J. Rothman, L. J. Nowicki, and G. E. Murch, J. Physics. F: Metal Phys. 10 (1980) 383—398.

28. L. E. Murr, G. I. Wong, and R. J. Horylev, Acta Met. 21 (1973) 593—603.

29. R. E. Schramm and R. P. Reed. Met. Trans. A 6A (1975) 1343—1418.

30. J. J. Sniegowski and W. G. Wolfer, "On the Physical Basis for the Swelling Resistance of Ferritic Steels," Ferritic Alloys for Use in Nuclear Energy Technologies, Proc. of Topical Conf., TMS AIME, New York, 1984.

31. M. R. Hayns, J. Gallagher, and R. Bullough. "The Derivation of a Simple Void Swelling Equation for Cold Worked 316 Austenitic Stainless Steel." AERE Harwell Report TP.739, 1978.

32. P. T. Heald, Phil. Mag. 31 (1975) 551–558.

33. F. W Young, J. Nucl. Mater. 69&70 (1978) 310–370.

34. L. K. Mansur, J. Nucl. Mater. 83 (1979) 109–127.

35. N. M. Ghoniem and D. D. Cho, "The Influence of Vacancy Clustering on the Early Stages of Interstitial Loop Formation and Growth," UCLA-ENC-7845, School of Engineering and Applied Science, University of California, Los Angeles, 1978.

36. M. R. Hayns, J. Nucl. Mater. 56 (1975) 267–274.

37. J. F. Bates and M. K. Korenko. Nucl. Tech. 48 (1980) 303–314.

38. F. A. Garner, "Overview of the Swelling Behavior of 316 Stainless Steel," Optimizing Materials for Nuclear Applications, Symp. Proc., TMS AIME, New Yark, 1985.

39. R. W. Clark, "Dimensional Change Correlations for 20% Cold-Worked AISI 316 Stainless Steel for Fusion Applications," Master's Degree Thesis, University of Missouri, Rolla, 1985.

40. J. I. Bramman, C. Brow, J. S. Watkin, C. Cawthorne, E. J. Fulton, P. J. Barton, and E. A Little, "Void Swelling and Microstructural Changes in Fuel Pin Cladding and Unstressed Specimens Irradiated in DFR," Radiation Effects in Breeder Reactor Structural Materials. Int. Conf. TMS AIME, New York, 1977, 479–507.

41. H. R. Brager and J. L. Straalsund, J. Nucl. Mater. 46 (1973) 124–158.

42. P. J. Barton, B. L. Eyre, and D. A Stow, J. Nucl. Mater. 67 (1977) 181–197.

43. H. R. Brager, J. Nucl. Mater. 57 (1975) 103–118.

44. L. K. Mansur, Nucl. Tech. 40 (1978) 5–34.

45. H. R. Brager, F. A Garner, E. R. Gilbert, J. E. Flinn, and W. G. Wolfer, J. Nucl. Mater. 46 (1973) 727–756.

46. N. H. Packan and K. Ferrell, "Ion Damage in 316 Stainless Steel Over a Broad Dose Range," Effects of of Radiation on Materials: Eleventh Int. Symp. ASTM STP 782, 1982, 885–894.

47. H. R. Brager and J. L. Straalsund, J. Nucl. Mater. 47 (1973) 105–109.

48. F. A Garner, "The Microchemical Evolution of Irradiated Stainless Steel," Phase Stability During Irradiation, Symp. Proc., TMS AIME, New York, 1981, 165–190.

7.0 Acknowledgment

This work was also supported in part hy the Division of Materials Sciences, U.S. Department of Energy, under contract DE-AC05-840R21400 with Martin Marietta Energy Systems, Inc.

8.0 Future Work

This modeling work will continue and in a future report a more detailed examination of parametric dependencies will be reported. An analysis will be made of the effect of using alternate descriptions for the faulted loop bias factors.

ION-INDUCED SPINOOAL-LIYE DECOMPOSITION OF Fe-Ni-Cr INVAR ALLOYS

F. A. Garner and H. R. Brager (Westinghouse Hanford Co.), R. A. Oodd (University of Wisconsin) and T. Lauritzen (General Electric Co.)

1.0 Objective

The object of this effort is to identify the mechanisms by which radiation affects the properties and dimensions of structural materials.

?.0 Summary

It was recently discovered that Fe-Cr-Ni alloys with 35 ± 10 wt% nickel decompose in a spinodal-like manner when irradiated with fast neutrons. This unexpected decomposition has many consequences. Not only do the anomalous properties characteristic of the Invar compositional regime disappear, but pronounced changes occur in both tensile properties and void swelling. Ion bombardment experiments have also been used to study void swelling and are now being used to study the decomposition. Microscopy and EDX examination of specimens employed in earlier void swelling studies confirm that ion irradiation induces spinodal-like decomposition in these alloys. The period and amplitude of the compositional fluctuations induced by radiation are sensitive to temperature, nickel content and crystallographic direction, but are not very sensitive to chromium content or displacement rate.

3.0 Program

Title: Irradiation Effects Analysis (AKJ)
Principal Investigator: O. G. Ooran
Affiliation: Hanford Engineering Oevelopment Laboratory

4.0 Relevant OAFS Program Plan Task/Subtask

Task II.C.2.1 Effects of Material Parameters on Microstructure
Task II.C.16 Composite Correlation Models and Experiments

5.0 Accomplishments and Status

5.1 Introduction

In several earlier papers it was reported that Fe-7.5Cr-35.5Ni (wt%) decomposes by a previously unexpected mechanism during neutron irradiation at ~1 x 10^{-6} dpa/sec and temperatures in the range 550-600°C.[1,2] This decomposition manifests itself in compositional oscillations with periods on the order of hundreds of nanometers at ~600°C. Iron and chromium appear to behave as one species, while nickel behaves in the opposite manner. In general the nickel profiles are mirror images of that of iron and chromium. The local composition appears to oscillate between Fe_3Ni and FeNi, with chromium substituting for iron. These oscillations cannot be correlated with any currently existing microstructural components.

There is a densification of ~1% that occurs upon decomposition of this alloy and postirradiation density change measurements on other alloys have been used to infer that similar spinodal-like decomposition occurs throughout the near-Invar compositional range.

If this decomposition is in fact spinodal-like in nature, one would expect that the period of oscillation would be sensitive to temperature and crystallographic direction and would also lead to changes in mechanical properties.[3] Hardening has been predicted to result from spinodal decomposition[3] and this has been verified experimentally in several copper-base alloys.[4,5] It now appears that a similar hardening may occur in the Fe-Ni-Cr system during irradiation.

Figure 1 shows the results of tensile studies in which the neutron-induced change in yield strength was determined for three Fe-XNi-15Cr alloys (X = 25, 35, 45) and two Fe-35Ni-YCr alloys (Y = 7.5, 22) after irradiation at 450°C to 12.5 dpa in the EBR-II reactor.[6] The sizes and densities of neutron-induced microstructural components of these alloys were also determined by electron microscopy and predictions were made of the anticipated changes in strength based on the observed microstructures. No precipitates or ordered domains were observed; only voids, Frank loops and network dislocations. Figure 1 shows that an increasing disparity was observed between measured and predicted strength changes with increasing nickel content in the Invar compositional regime, but also shows that the strength change was insensitive to chromium content at 35% nickel.

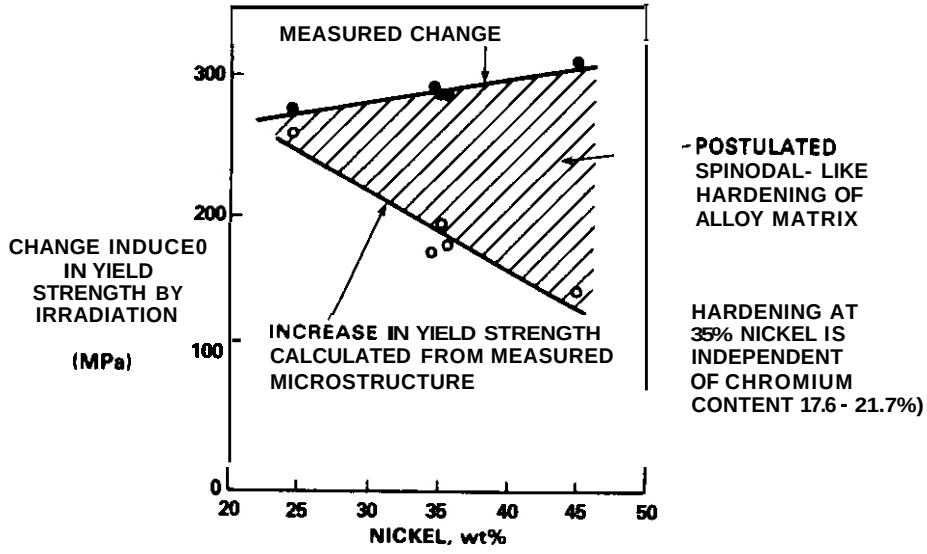

FIGURE 1. Comparison of measured yield strength changes and microstructurally-based predictions in five Fe-Ni-Cr alloys after irradiation at 450°C to 12.5 dpa in EBR-II.[6]

The additional hardening component observed in this experiment was postulated to arise from the presence of spinodal-like micro-oscillations of magnitude less than 100 nm. Unfortunately, the resolution limit of the energy dispersive x-ray technique (EDX) employed in these studies lies in the range 60-100 nm. This limit is defined by the volume sampled by the focused electron probe. This volume in turn is defined by the width of the incident beam (~30 nm), the thickness of the foil (50-70 nm), the angle between the beam axis and the foil normal (45°) and the tendency of the beam to spread out as it traverses the foil. The relationship between the beam, specimen and detector is shown in Figure 2.

It has also been proposed, however, that the dependence of swelling on nickel content at relatively high irradiation temperatures arises from the strong effect of nickel on two competing processes, both of which increase in importance as the temperature rises.[2,7,8,9] The first is the effect of nickel on the effective vacancy diffusion coefficient and thereby on void nucleation. The second is the tendency of Fe-Ni-Cr alloys to undergo spinodal-like decomposition. As shown in Figure 3 these two processes are thought to produce the minimum in swelling observed in the Invar regime. The swelling resistance is proposed to be gradually destroyed in this compositional range as voids nucleate in the relatively large volumes whose nickel levels are relatively low and whose chromium levels are relatively high. It was earlier shown that at these higher irradiation temperatures, decreasing nickel and increasing chromium were both equally effective ways of speeding up the onset of void swelling during neutron irradiation.[7,10]

Since the minimum in swelling with nickel content was observed not only in neutron irradiated but also ion irradiated[11] Fe-Ni-Cr alloys, it therefore followed from this hypothesis that compositional micro-oscillations must be also be generated during ion bombardment. Since the Fe-Cr-Ni specimens used by Johnston and coworkers to define the compositional dependence of swelling (Figure 4) were still available

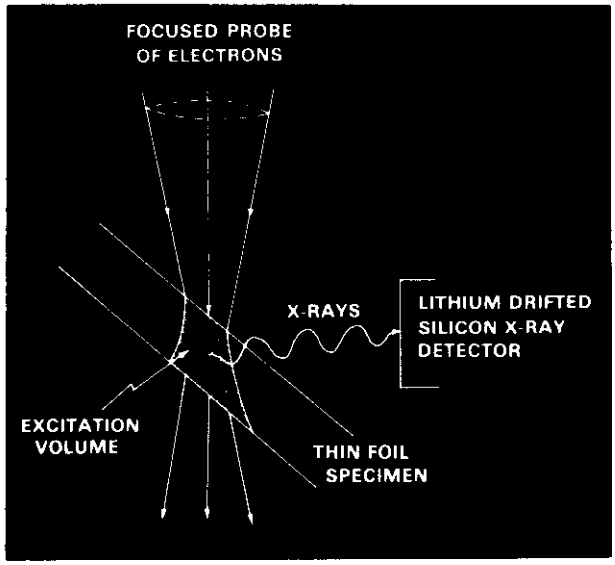

FIGURE 2. Schematic representation of beam, foil and detector relationships during EDX analysis of irradiated specimens.

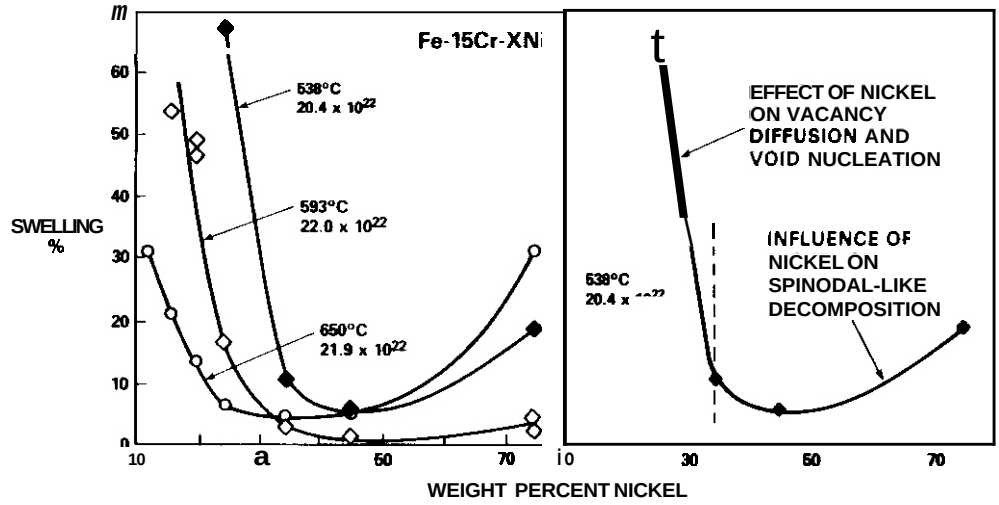

FIGURE 3. (a) Dependence of swelling of Fe-15Cr-XNi alloys on temperature, neutron fluence and nickel content. (b) Swelling behavior is postulated to arise from competition between two mechanisms operating at high temperatures.

in the post-irradiation thinned condition, they are now being examined by the current authors using EOX analysis. The irradiations were conducted ten years prior to this time and yet the specimens generally were found to be in excellent shape.

The regions available for examination are 850-1050 nm from the original specimen surface and accumulated exposures up to 117 dpa at temperatures of either 625 or 675°C. The displacement rate was 2 x 10-2 dpafsec. The EOX procedures used in the analysis are identical to those used for the neutron irradiated specimens,[1,2] and involve the use of a single tilt specimen stage in either a JEOL 1200 or JEOL 200CX electron microscope. Each microscope was used for a separate series of experiments.

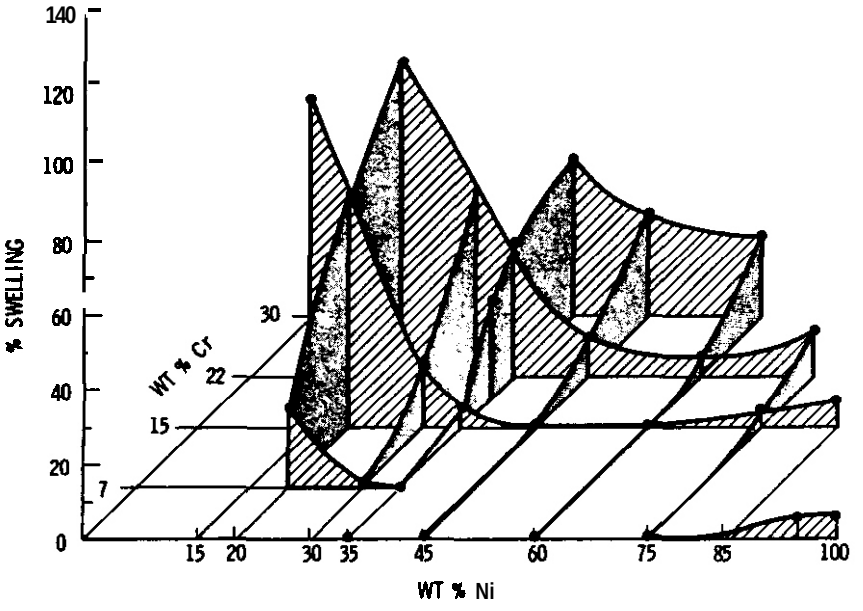

FIGURE 4. Swelling induced in Fe-Cr-Ni alloys by irradiation with 5 MeV Ni+ ions to 117 dpa at 675°C.[11]

5.2 Results

In the first series of experiments the specimen examined was chosen to be comparable to the Fe-35.5Ni-7.5Cr specimen which developed micro-oscillations during neutron irradiation[1,2]. Johnston and coworkers had irradiated this Fe-35.0Ni-7.0Cr specimen to 117 dpa at 625°C. In the original study very little void swelling (<0.01%) was found by Johnston to have occurred. This specimen was examined in the current study on the JEOL 1200 microscope at Westinghouse Hanford Company.

Although there were very few microstructural features observed within suitably thin areas (50-80 nm thick) of the specimen, straight-line compositional traces were obtained starting at features which appeared to be surface contamination particles. Figure 5 shows four such sets of measurements and confirms that micro-oscillations have been generated by ion irradiation. Note that the period of the oscillations is on the order of 200-400 nm and that once again the chromium and iron traces tend to be mirror images of that of nickel.

In Figure 6 each of the chromium and nickel levels shown in Figure 5 has been plotted to show that these elements indeed segregate in opposite directions. Similar data points for the (593°C, 38 dpa) neutron-irradiated Fe-35.5Ni-7.5Cr specimen[1] are also shown. Note that in addition to the similar trend of the two groups of data that there is also an offset between the two groups. Although a small offset arises from the slight difference in composition in the two alloys, this factor alone is insufficient to account for the difference. It is thought that the offset arises primarily from an ion-induced modification of the average composition at the depth examined. Johnston,[12] as well as others,[13,14] have shown that the elemental distribution is changed along the ion path in Fe-Ni-Cr alloys. This is due to the combined influence of the foil surface and the gradient in displacement rate, operating in conjunction with the inverse Kirkendall effect and possibly other diffusion mechanisms. Large-area compositional scans (compiled in Table 1) confirm that the average composition at this depth was indeed shifted from the original bulk-averaged level.

It should be noted that the limitations imposed by the single tilt stage normally used for EDX analysis do not allow an easy determination of the crystallographic vector along which the compositional trace is taken. Additional experiments now in progress are directed toward obtaining the dependence of the oscillations on crystallographic direction.

The second series of experiments were performed on a JEOL 200CX microscope at the University of Wisconsin-Madison involving Ni+ ion irradiated Fe-Ni binaries at 35, 45, 60 and 75Ni as well as Fe-15Cr-Ni tenaries containing the same nickel levels. Each alloy had been irradiated at two temperatures, 625 and 675°C. Although the measurements were performed in thicker foils (150-200 nm) in this experimental series, micro-

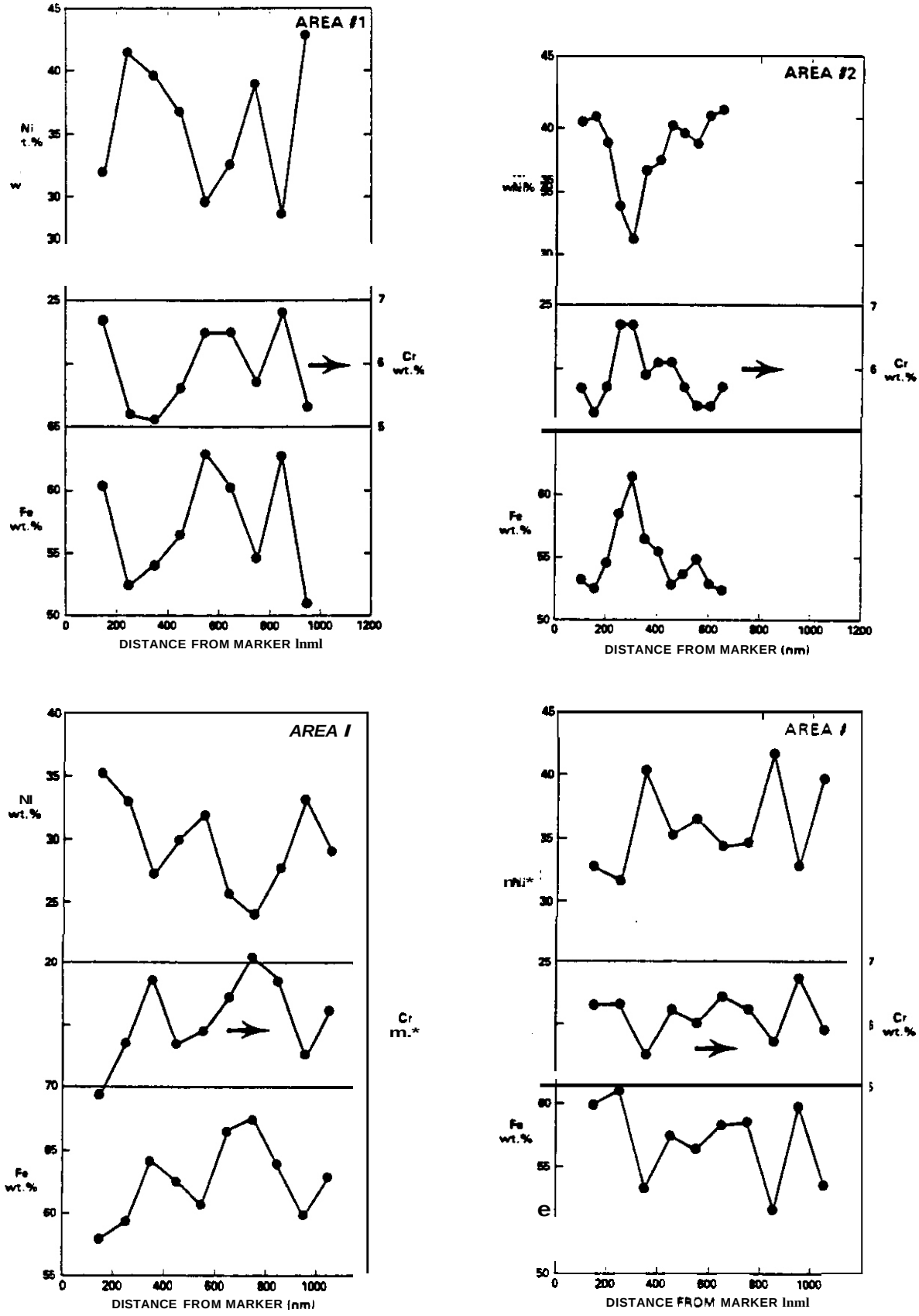

FIGURE 5. Compositional oscillations observed in **Fe-35.0Ni-7.0Cr** irradiated to 117 dpa with 5 MeV **Ni+** ions at **625°C.**

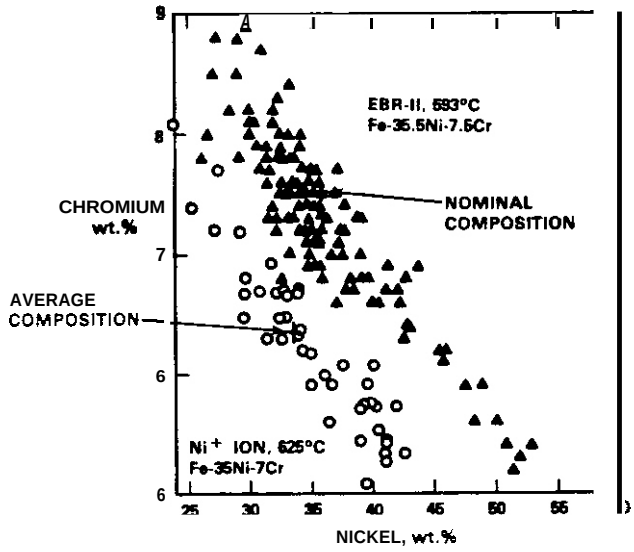

FIGURE 6. Compilation of ion-induced decomposition data from Figure 5. The neutron-induced compositional data from ref. 1 is also shown for comparison.

TABLE 1

LARGE AREA MEASUREMENTS OF AVERAGE COMPOSITION AT 850-1050 nm DEPTH IN AN ION-BOMBARDED SPECIMEN OF Fe-35.0Ni-7.0Cr AT 625°C AND 117 dpa

Area	Cr (wt%)	Ni (wt%)
#1	6.1	33.9
#2	5.8	33.6
#3	6.3	34.5
#4	6.6	34.8
#5	6.6	33.4
#6	6.3	33.9
Average	6.3	34.0

oscillations were observed in all specimens at both temperatures. In general the amplitude and period of the oscillations was largest in the mid-range of nickel levels (35-45%).

These measurements are now being repeated on thinner foils, using both the JEOL 200CX and HB501 microscopes. The latter microscope has a much smaller electron probe (<10 nm) and will yield better resolution of the oscillations when thinner foil sections are studied.

For the purposes of this paper it is sufficient to present from this second series only three results, all of which show that chromium is not a necessary participant in the decomposition process. Figure 7 shows a random-direction straight-line compositional trace along a Fe-45Ni specimen irradiated to 102 dpa at 675°C. The observed changes in nickel level are quite large, even though in foils of this thickness such variations tend to be averaged back toward the nominal alloy composition. The period of the oscillations at 675°C appear to be comparable but somewhat larger (200-400 nm) than those observed in neutron-irradiated specimens at 550-600°C.[1,2]

Occasionally, some composition traces tended to be very regular and almost sinusoidal, as shown in Figure 8, while other traces in the same specimen exhibit the irregularity observed in earlier studies. In Figure 8 the Fe-35Ni specimen irradiated at 625°C to 117 dpa possessed a wavelength of ~400 nm in the near-sinusoidal trace shown. A similar example is shown in Figure 9 where the same alloy at 117 dpa but 675°C also exhibited a period in the 300-400 nm range. It is thought that the regular oscillations shown in Figures 8 and 9 represent traces taken near <100> directions while that in Figure 7 was taken along some vector which was not low-index. Spinodal development in fcc alloys should exhibit its longest oscillation period along <100> directions.[3] Soon-to-be published data on neutron-irradiated specimens tend to confirm this hypothesis.

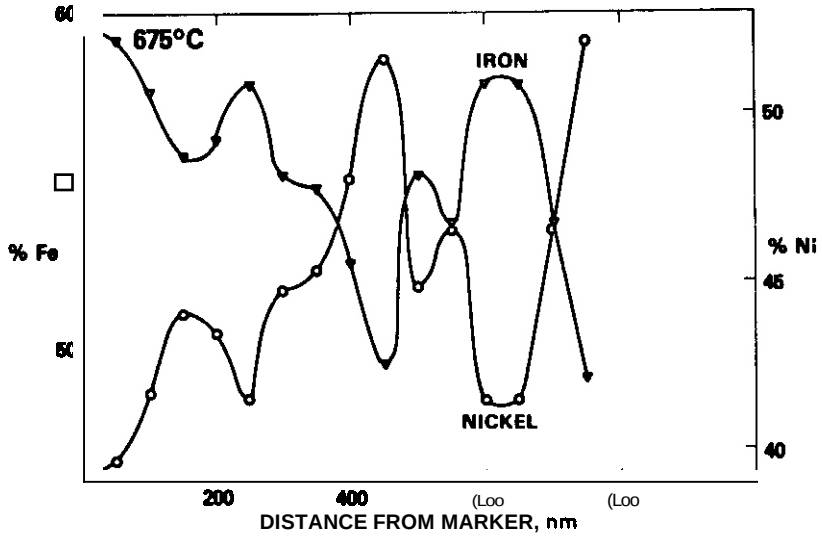

FIGURE 7. Decomposition observed in Fe-45Ni irradiated to 102 dpa with 5 MeV Ni^+ ions at 675°C.

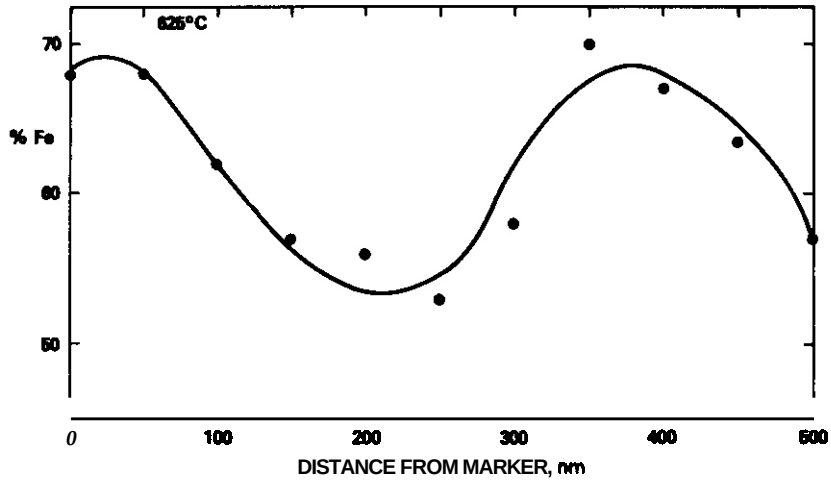

FIGURE 8. Oscillation of iron level in Fe-35Ni irradiated to 117 dpa by 5 MeV Ni+ ions at 625°C.

5.3 Discussion

In an earlier paper the potential causes of this decomposition phenomenon were discussed in detail.(2) It was shown that other studies conducted at lower irradiation temperatures found alloys in the Invar regime to break down into ordered FeNi and another disordered fcc phase with composition near Fe_3Ni. These are the same compositional limitations observed in the neutron irradiated specimens.

If we assume that this decomposition requires first a long range segregation process and second a local ordering process, it is not unreasonable to assume that the first stage segregation process continues to operate at temperatures above the critical ordering temperature of the second-stage ordering process. The segregation process is obviously rather sluggish even during irradiation and requires large levels of atomic displacements for its initiation.(1,2) It may be that the decomposition process requires not only the enhanced diffusion inherent in the radiation environment but also some feature unique to irradiation. The Inverse Kirkendall effect is such a feature and is known to segregate nickel at the expense of chromium and iron at any sink where there is a strong vacancy gradient. The presence of radiation-generated interstitials may also play a role.

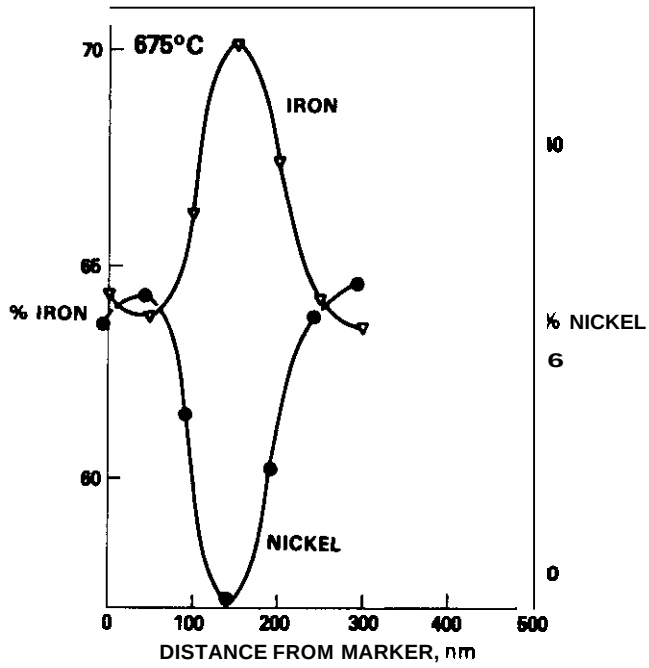

FIGURE 9. Oscillation of iron level in Fe-35Ni irradiated to 117 dpa by 5 MeV Ni^+ ions at 675°C.

There are several features of these results that run counter to the established perception of spinodal decomposition. First, the wavelengths are much larger than would be observed during spinodal decomposition in a non-radiation environment. A model currently being explored by the lead author and G. Martin may explain the large wavelengths in terms of the relaxation distance of the point defect profiles generated near microstructural sinks during irradiation at high temperatures and low sink densities. This radiation-altered spinodal-like model must also confront the fact that the established perception is that the Fe-Ni and Fe-Ni-Cr systems do not decompose spinodally in the Invar regime during thermal aging. In recent years, however, a number of authors have independently reached the conclusion that a very sluggish spinodal decomposition should occur in the Fe-Ni system in the Invar composition range.[15-17]

More recently, however, Chuang and coworkers have shown that when recently measured magnetic contributions to various thermodynamic functions are employed, the calculated phase diagram for the Fe-Ni system contains a miscibility gap in which a two phase fcc regime exists in the Invar regime and which is associated with a spinodal.[18] The peak of the calculated miscibility gap reaches only to ~450°C, however, and not to the 625-675°C range employed in this study. Based on a variety of experimental studies, however, Tanji and coworkers assert that a very sluggishly-developing spinodal lies below a miscibility gap that extends as high as ~1000°C.[17,19] It therefore appears that spinodal-like behavior during irradiation is not totally unexpected in the Invar regime.

It should also be noted that the neutron and ion irradiations discussed in this paper were conducted at displacement rates that were more than four orders of magnitude in difference and yet there were not large changes in wavelength observed. If the displacement rate is ignored the wavelengths increase slowly with temperature, although this trend is somewhat obscured by the irregularity associated with the unknown crystallographic vectors employed in each EDX trace. This implies that the spinodal-like decomposition is not very sensitive to displacement rate and that the small range of variation observed in oscillation wavelength may be due mostly to differences in irradiation temperature. This conclusion also supported the concept of a radiation-enhanced spinodal process rather than a compositional instability that requires radiation for its continued existence. Post-irradiation annealing studies are planned to resolve which of these two is the more correct interpretation.

The hardening of these alloys associated with spinodal-like decomposition during ion irradiation will also lead to a surface layer that is harder than the underlying material while not retaining its original Invar properties. This development may have a pronounced influence of the behavior of Invar alloys whose surfaces have been irradiated with ions, particularly at lower irradiation temperatures not covered in this study.

5.4 Conclusions

At temperatures above ~450°C Fe-Ni and Fe-Ni-Cr alloys in the Invar compositional range decompose by an unexpected spinodal-like mechanism when irradiated by either neutrons at ~1 x 10^{-6} dpa/sec or 5 MeV Ni^{+} ions at 2 x 10^{-2} dpa/sec. This decomposition appears to be somewhat sensitive to irradiation temperature, not very sensitive to displacement rate and not at all sensitive to the chromium level. There is some evidence that the process may be dependent on crystallographic direction and that it may induce an eventual loss of resistance to void swelling.

6.0 References

1. H. R. Erager and F. A. Garner, Effects of Radiation on Materials: Twelfth Conference, ASM STP 870, F. A. Garner and J. S. Perrin. eds. American Society for Testing and Materials, Philadelphia, PA (1985), pp. 139-150.

2. H. R. Brager and F. A. Garner, Optimizing Materials for Nuclear Applications. TMS-AIME, Warrendale, PA, 1985, pp. 141-166.

3. J. W. Cahn, Acta. Met., 11 (1963) 1275.

4. A. Datta and W. A. Soffa, Acta Met., 24 (1976) 987.

5. L. H. Schwartz, S. Mahajan and J. T. Plewes, Acta Met., 22 (1974) 601; also p. 111.

6. H. R. Brager, F. A. Garner and M. L. Hamilton. J. Nucl. Mater., 133 & 134 (1985) 594.

7. F. A. Garner, J. Nucl. Mater., 122 & 123 (1984) 459.

8. F. A. Garner, J. Nucl. Mater., 133 & 134 (1985) 113.

9. F. A. Garner and W. G. Wolfer, J. Nucl. Mater., 122 & 123 (1984) 201.

10. F. A. Garner and H. R. Brager, pp. 187-201 in Ref. 1.

11. W. G. Johnston, J. H. Rosolowski, A. M. Turkalo and T. Lauritzen, J. Nucl. Mater., 54 (1974) 24.

12. W. G. Johnston, W. G. Morris and A. M. Turkalo, Proc. of Inter. Conf. on Radiation Effects on Breeder Reactor Materials, M. L. Eleiberg and J. W. Bennett, eds; AIME, New York, NY. (1977) pp. 421-430.

13. N. W. Lam, J. Nucl. Mater. 117, (1984) 106.

14. A. D. Marwick, R. C. Pillar and M. E. Horten, Dimensional Stability and Mechanical Behavior of Irradiated Metals and Alloys, Vol. I, British Nuclear Energy Society, London (1983) pp. 11-15.

15. J. R. C. Guimaraes, J. Danon, R. B. Scorzelli and I. Souza Azevedo, J. Physics F: Metal Physics, 10 (1980) pp. L197-L202.

16. P. L. Rossiter and P. J. Lawrence, Phil. Mag. A, 49 (4) (1984) 535.

17. Y. Tanji, Y. Nakagawa, Y. Saito, K. Nishimura and K. Nakatsuka, Phys. Stat. Sol. A, 56 (1979) 513.

18. Y. Chuang, Y. A. Chang, R. Schmid. J. Lin, to be published in Met. Trans.

19. Y. Tanji, Y. Nakagawa and S. Steinemann, Physica, 119 B+C (1983) 109.

7.0 Future Work

Examination of ion bombarded specimens will continue to determine both the compositional and crystallographic dependence of the micro-oscillations.

8.0 Publications

This report will be submitted for publication in a special volume of Nuclear Instruments and Methods in Nuclear Research. This volume will contain the proceedings of a TMS-AIME Symposium on Irradiation Effects associated with Ion Implantation, held in Toronto, Canada on October 14-15, 1985.

OWR/RTNS-II LOW EXPOSURE SPECTRAL EFFECTS EXPERIMENT

H. L. Heinisch (Hanford Engineering Development Laboratory)

1.0 Objective

The objective of this experiment is to determine the effect of the neutron spectrum on radiation-induced changes in mechanical properties for metals irradiated with fusion and fission neutrons.

2.0 Summary

The status of the OWR/RTNS-II Low Exposure Spectral Effects Experiment is reviewed. Several irradiations have been completed or are in progress. Tensile specimens from the first elevated temperature RTNS-II irradiation for this experiment have been tested. Some specimens irradiated at room temperature have also been tested. Yield stress and ultimate tensile strength as a function of 14 MeV neutron fluence are reported here for pure copper and 316 stainless steel. Both annealed copper and solution annealed 316 stainless steel exhibit a definite temperature dependence in their response to 14 MeV neutron irradiation.

3.0 Program

Title: Irradiation Effects Analysis
Principal Investigator: D. G. Ooran
Affiliation: Westinghouse Hanford Company

4.0 Relevant DAFS Program Plan Task/Subtask

Subtask II.B.3.2	Experimental Characterization of Primary Damage State; Studies of Metals
Subtask II.C.6.3	Effects of Damage Rate and Cascade Structure on Microstructure; Low-Energy1 High Energy Neutron Correlations
Subtask II.C.16.1	14-MeV Neutron Damage Correlation

5.0 Accomplishments and Status

5.1 RTNS-II Irradiations

The OWR/RTNS-II Spectral Effects Experiment (HEDL-SEX), described in detail elsewhere,[1] calls for three RTNS-II irradiations to be performed using the HEDL Dual-Temperature, Vacuum-Insulated (DTVI) furnace operating at 90°C and 290°C. The first RTNS-II irradiation was completed in September, 1984, to a peak fluence of 2.4×10^{18} n/cm^2. The second irradiation, to a peak fluence of approximately 1×10^{19} n/cm^2, will be completed November 2, 1985. This is the highest fluence ever achieved in a continuous irradiation at the RTNS-II, and it is the highest dose of D-T (14 MeV) neutrons ever received by metal specimens.

Both HEDL-SEX irradiations at RTNS-II have been joint U.S./Japan irradiations, with the United States having the primary responsibility. As an adjunct to the fusion neutron portion of the experiment, some HEDL-SEX tensile specimens were also included in a Japanese-sponsored room temperature irradiation at RTNS-II. Also, HEOL-SEX specimens are included in the joint Japan/U.S. long-term irradiation now in progress using the Japanese DTVI furnace. Temperatures for this irradiation are 200°C and 450°C, and the target peak fluence is also 1×10^{19} n/cm^2.

5.2 Omega West Reactor Irradiations

HEDL-SEX calls for eight companion irradiations in the Omega West Reactor (OWR) at Los Alamos National Laboratory to four fluences at each of the temperatures, 90°C and 290°C. The fluences span the range of the fluences received in RTNS-II. At this time, there are no plans to do any further OWR irradiations.

Three OWR irradiations have been completed at 90°C, and the fourth at this temperature is in progress. The four irradiations at 290°C will immediately follow the 90°C irradiations.

The OWR irradiations use the In-Core Reactor Furnace developed at Lawrence Livermore National Laboratory for OWR irradiations. Temperatures of the specimens are maintained by balancing nuclear heating, coolant flow through the furnace, and resistance heating near the specimens. In the lower irradiation temperature region (including 90°C), the furnace utilizes the reactor coolant water to maintain the required temperature, while at the higher temperatures a flow of helium gas is used. A resistance heater within the furnace provides precise control of the temperatures.

The tensile specimens are contained in capsules developed at HEDL that were designed to provide well-controlled specimen temperatures by minimizing temperature gradients caused by nuclear heating. One capsule contained thermocouples directly welded to specimens so that a correlation among the furnace, capsule, and specimen temperatures could be determined. Measurements with this capsule in the reactor showed that temperatures can be controlled during a run to within 2°C, and the absolute specimen temperatures can be determined to within five degrees at both temperatures.

5.3 Tensile Testing

Tensile tests have been done on specimens irradiated at room temperature in RTNS-II and on those from the first elevated-temperature RTNS-II run.

The tensile tests were performed at room temperature using a tensile frame designed specifically for miniature specimens.[2] Control specimens are tested periodically, and results fall within a 20 band of ±6% for yield stress and ultimate tensile strength. The largest source of error is in measuring the variation in the specimen dimensions, which becomes more important with increasing specimen size.

The changes in 0.2% offset yield stress and the ultimate tensile strengths are plotted as functions of neutron fluence in Figures 1 and 2 for copper and Figures 3 and 4 for solution annealed AISI 316 stainless steel. Straight line segments connect the set of data points for each irradiation temperature. Neutron fluences for each specimen are known within about ±3%, based on dosimetry methods described earlier.[3]

The change in yield stress of copper shows an expected temperature effect, which is reflected to a lesser extent in the ultimate tensile strength. Within this fluence range there is no discernable effect of 14 MeV neutron irradiation in copper at 290°C. The increasing defect mobility at higher temperatures evidently results in more defect pair recombination and perhaps coarsening of the surviving radiation-induced defect cluster distribution.

Temperature effects are also seen in the radiation-induced changes in yield stress of solution annealed 316 stainless steel. Even though the data at 290°C has considerable scatter, there is a clear difference in the behavior at this temperature. There is no apparent effect of 14 MeV neutrons on the ultimate tensile strength of 316 stainless steel at these fluences and temperatures.

6.0 References

1. H. L. Heinisch and S. D. Atkin, OAFS Quarterly Progress Report, January-March, 1984, DOE/ER-0046/17, 76 (1984).
2. N. F. Panayotou, S. O. Atkin and R. J. Puigh, Proceedings of the ASTM Symposium on Use of Non-standard, Sub-Sized Specimens for Irradiation Testing. Albuquerque, NM, September, 1983.
3. H. L. Heinisch, OAFS Quarterly Progress Report, January-March, 1985, DOE/ER-0046/21, 99 (1985).

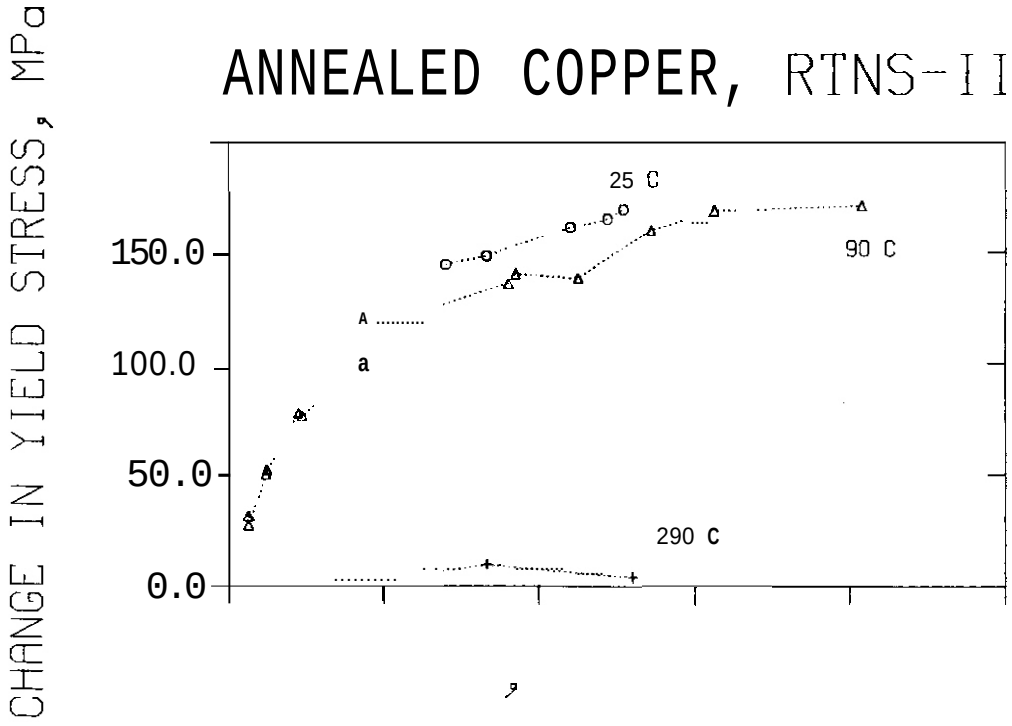

FIGURE 1. Change in Yield Stress as a Function of 14 MeV Neutron Fluence for Annealed Copper at Three Irradiation Temperatures..

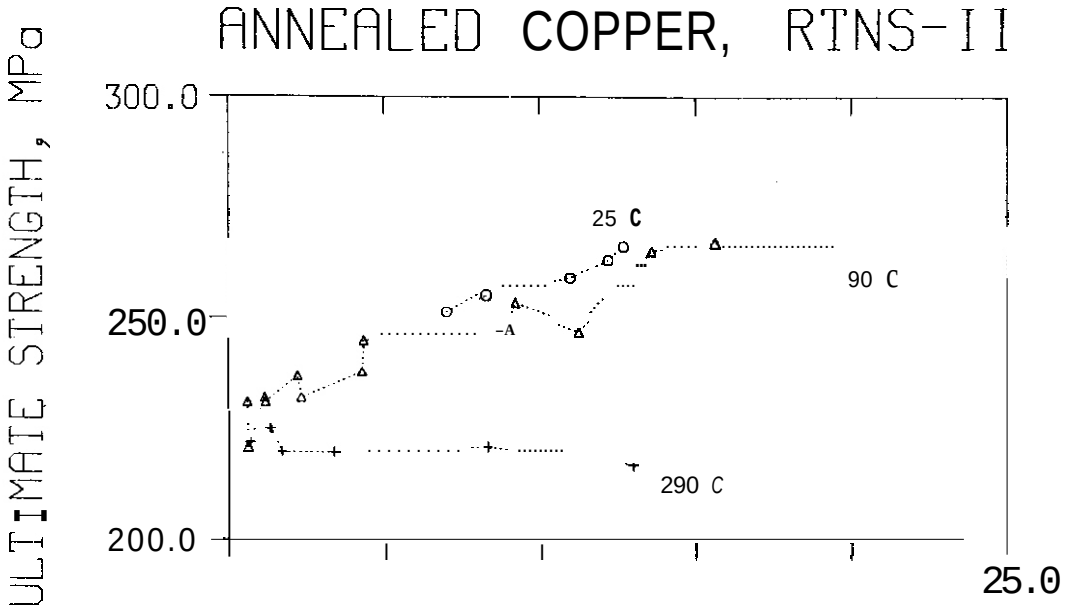

FIGURE **2. Ultimate Tensile Strength as a Function** of **14 MeV Neutron Fluence for Annealed Copper at Three Irradiation Temperatures.**

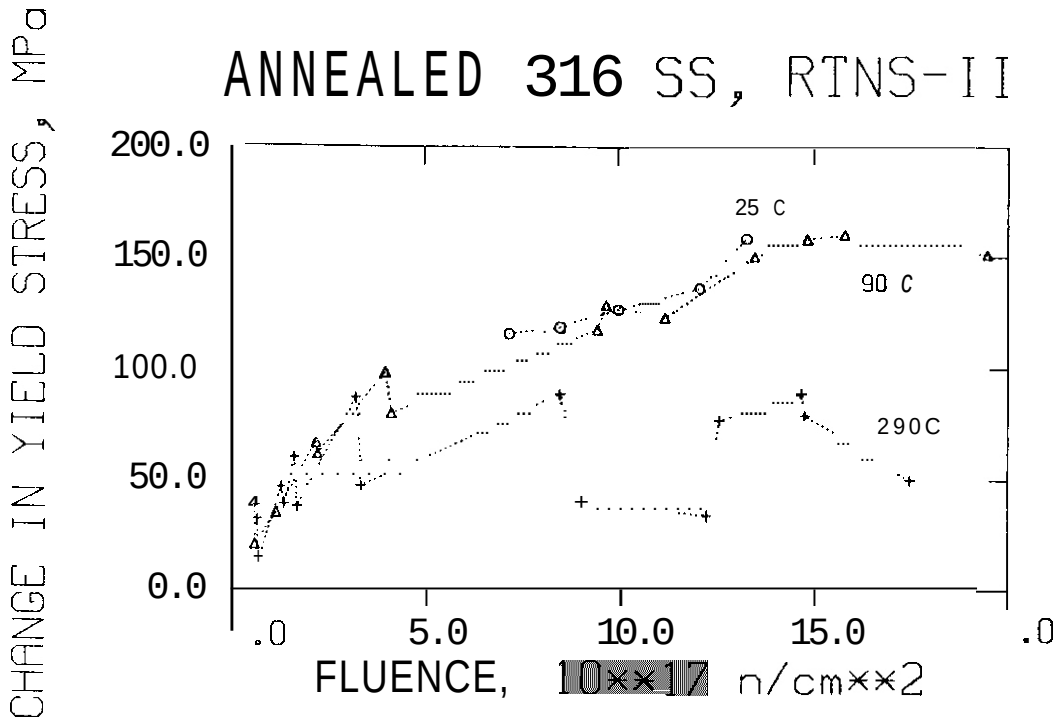

FIGURE 3. Change in Yield Stress as a Function of 14 MeV Neutron Fluence for Solution Annealed AISI 316 Stainless Steel at Three Irradiation Temperatures.

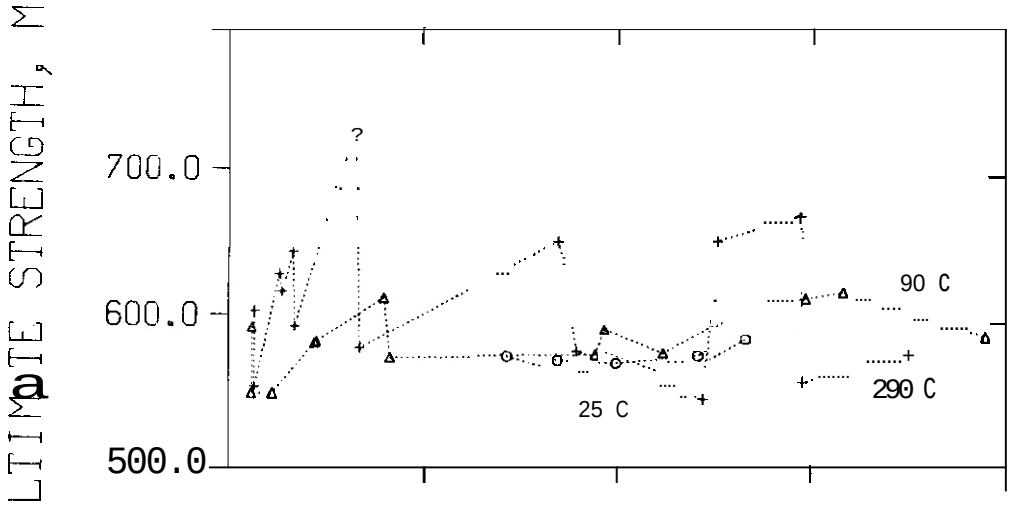

FIGURE 4. Ultimate Tensile Strength as a Function of 14 MeV Neutron Fluence for Solution Annealed AISI 316 Stainless Steel at Three Irradiation Temperatures.

CHAPTER 6

FUNDAMENTAL STUDIES OF SPECIAL PURPOSE MATERIALS

MICR'ISTRUCTURAL EXAMINATION OF PURE COPPER AND THREE COPPER ALLOYS IRRADIATED IN FFTF

H. R. Brager and F. A. Garner (Hanford Engineering Development Laboratory)

1.0 Objective

The object of this effort is to determine the origin of radiation-induced alterations of the properties of copper alloys anticipated for use in fusion environments.

2.0 *Summary*

Electron microscopy of pure copper irradiated at ~450°C to 16 dpa revealed no unexpected behavior, showing both dislocation and void development. In the same experiment, however, the dispersion-hardened alloy A125 exhibited a remarkable insensitivity to irradiation. The precipitation-hardened alloy MZC also had no voids present but the precipitate microstructure was changed such that an apparent swelling of 1.03% occurred. Dependent on the heat-treatment employed the alloy CuBeNi showed various levels of voidage, particularly in those areas which suffered recrystallization and alteration of the precipitate structure.

3.0 Program

Title: Irradiation Effects Analysis (AKJ)
Principal Investigator: D. G. Doran
Affiliation: Hanford Engineering Development Laboratory

4.0 Relevant DAFS Program Plan Task/Subtask

II.C.1. Effects of Material Parameters on Microstructure

5.0 Accomplishments and Status

5.1 Introduction

In an earlier report the neutron-induced changes in electrical conductivity, tensile properties and density were measured for high purity copper and eight copper alloys after irradiation at 450°C to ~16 dpa in FFTF-MOTA.[1] In this report the microstructures induced in pure copper and three of the copper alloys are described after examination by transmission electron microscopy. The composition, heat treatment and bulk density change of these alloys are shown in Table 1.

5.2 MARZ Copper

This alloy was irradiated in the annealed condition using zone-refined 99.999% pure MARZ copper. The irradiation was conducted at ~450°C which represents a homologous temperature of 0.53.

Thus one would expect a significant level of vacancy mobility at this temperature and a relatively low void density. Figure 1 shows that only a moderate density ($\sim 1 \times 10^{14}$ cm^{-3}) of quite large voids were observed. The average diameter of these voids was 90 nm and their shape was that of the usual truncated octahedra. The local swelling in the region shown in Figure 1 is ~4% compared to the measured change in bulk density of 6.5%. The difference probably reflects the region-to-region variability normally exhibited in foils with low to moderate void densities.

TABLE I

SWELLING OF VARIOUS COMMERCIAL COPPER ALLOYS IN MOTA-1B
AT ~450°C and 2.5 x 10^{22} n/cm^2 (E >0.1 MeV)

	Alloy Composition (wt.%)	Condition	% Swelling
Cu (MARZ)	cu (99.999%)	Annealed	6.5
CuNiBe (1/2 HT)*	Cu-1.8 Ni-0.3 Be	20% CW & Aged (3 hr at 480°C)	1.70
CuNiBE (AT)*	Cu-1.8 Ni-0.3 Be	Annealed & Aged (3 hr at 480°C)	0.29
MZC	Cu-0.9 Cr-0.1 Zr-0.05 Mg	90% CW, Aged 1/2 hr at 470°C	1.03
Cu-A125	Cu-0.25 Al_2O_3	20% CW	0.13

* 1/2 HT and AT are industry designations for half-hard and tempered, and annealed and tempered, respectively.

The dislocation density in this region was also relatively low (~3 X 10^{-9} cm^{-2}) and reflects both the purity of the copper and the high homologous temperature at which the irradiation was conducted. Also shown in Figure 1 is a low density (~10^{14}/cm^3) of small unidentified defect clusters. These clusters are not anticipated to have a significant effect on the electrical or mechanical properties when compared to the effect of the other microstructural components.

5.3 Dispersion-Strengthened Copper

The commercial alloy A125 was irradiated in the 20% cold-worked condition and is essentially pure copper strengthened with very small alumina particles formed by internal oxidation of a small amount of aluminum solute. In contrast to the pure copper which had large grains on the order of tens of microns, A125 contains grains and subgrains of micron and submicron sizes. In this particular alloy the Al_2O_3 is 0.25 percent by weight and is dispersed in particles ranging from 3 to 20 nm in size at a density of ~3 X 10^{16} cm^{-3}. As shown in Figure 2 both the particles and cold-worked dislocation density are relatively stable, not Only after aging for 1000 hours at 700°C, but also after irradiation to 16 dpa at ~450°C.

A very careful examination of the microstructure after irradiation showed that this alloy was remarkably insensitive to irradiation, with no voids or bubbles observed and very few Frank loops, but only at small sizes (<10 nm). Examples of the void-free matrix and precipitate microstructure are shown in Figure 3. Figure 4 shows when different diffraction vectors are used to image the precipitates after irradiation, the black-white contrast vector is always parallel to the diffraction vector. This indicates that the precipitates have a radially-symmetric strain field.

5.4 **Precipitation-Strenqthened** Cold-Worked Alloy

The MZC copper-base alloy contains small amounts of magnesium, zirconium and chromium which provide both solid solution strengthening and precipitation hardening. When combined with work hardening this alloy provides a good combination of high strength and high conductivity. The properties of the alloy are somewhat dependent on thermal-mechanical treatment. The recommended treatments are directed toward production of a high concentration of small precipitates which are rich in copper and zirconium. The purpose of introducing these precipitates is to stabilize the dislocation network at high temperatures. As shown in Figure 5 these precipitates were observed to be stable after aging for 1000 hours out-of-reactor at 400°C.

After a less detailed examination than that employed for the A125 alloy, it appeared that no voids had formed in the irradiated alloy. This is inconsistent with the reported density change of -1.03%. It is suspected that the apparent swelling is a consequence of a lattice parameter change of the matrix arising from precipitation. While Figure 6 shows that ~5 X 10^{16} cm^{-3} precipitates with sizes in the range 2-10 nm

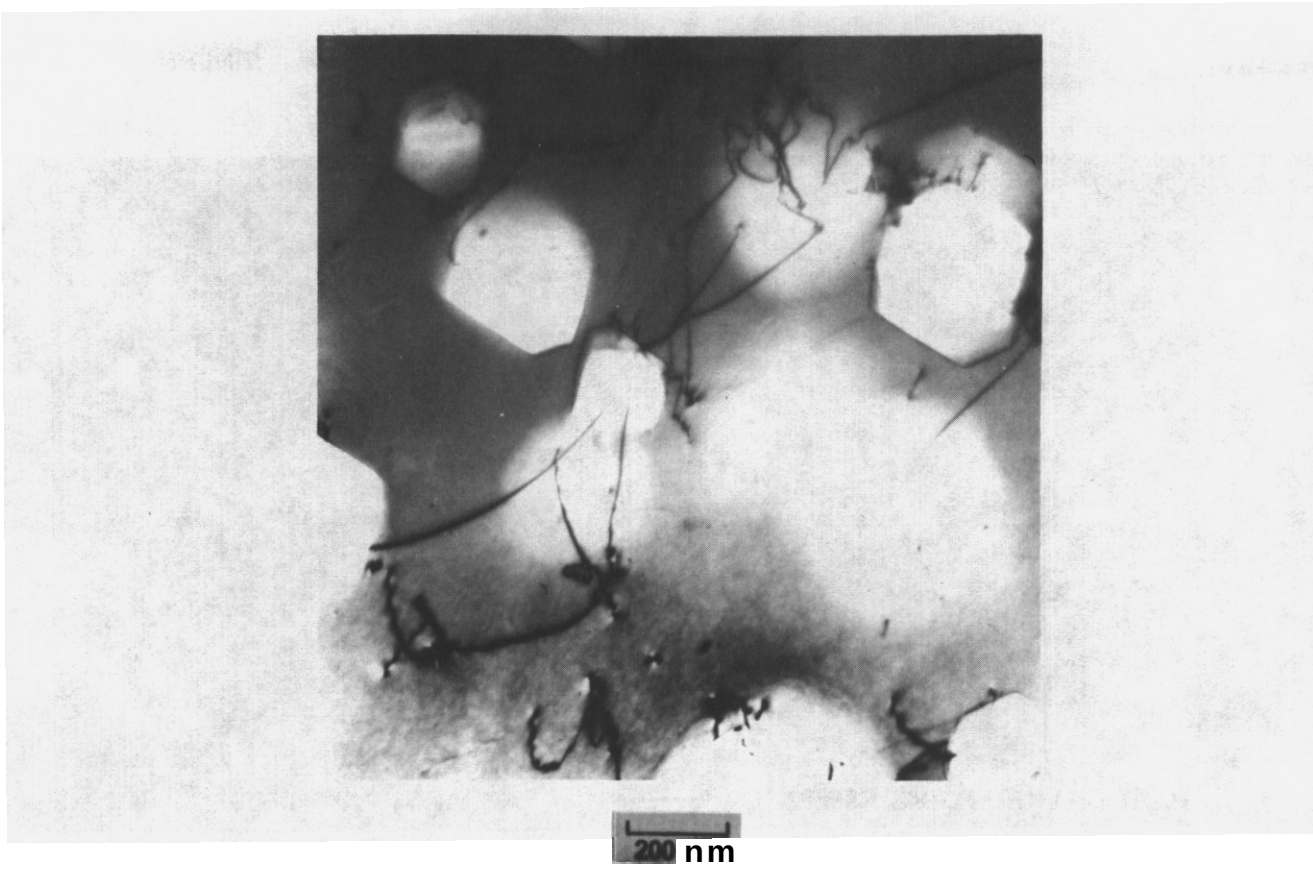

FIGURE 1. Large voids observed in MARZ copper after irradiation to 16 dpa at ~450°C.

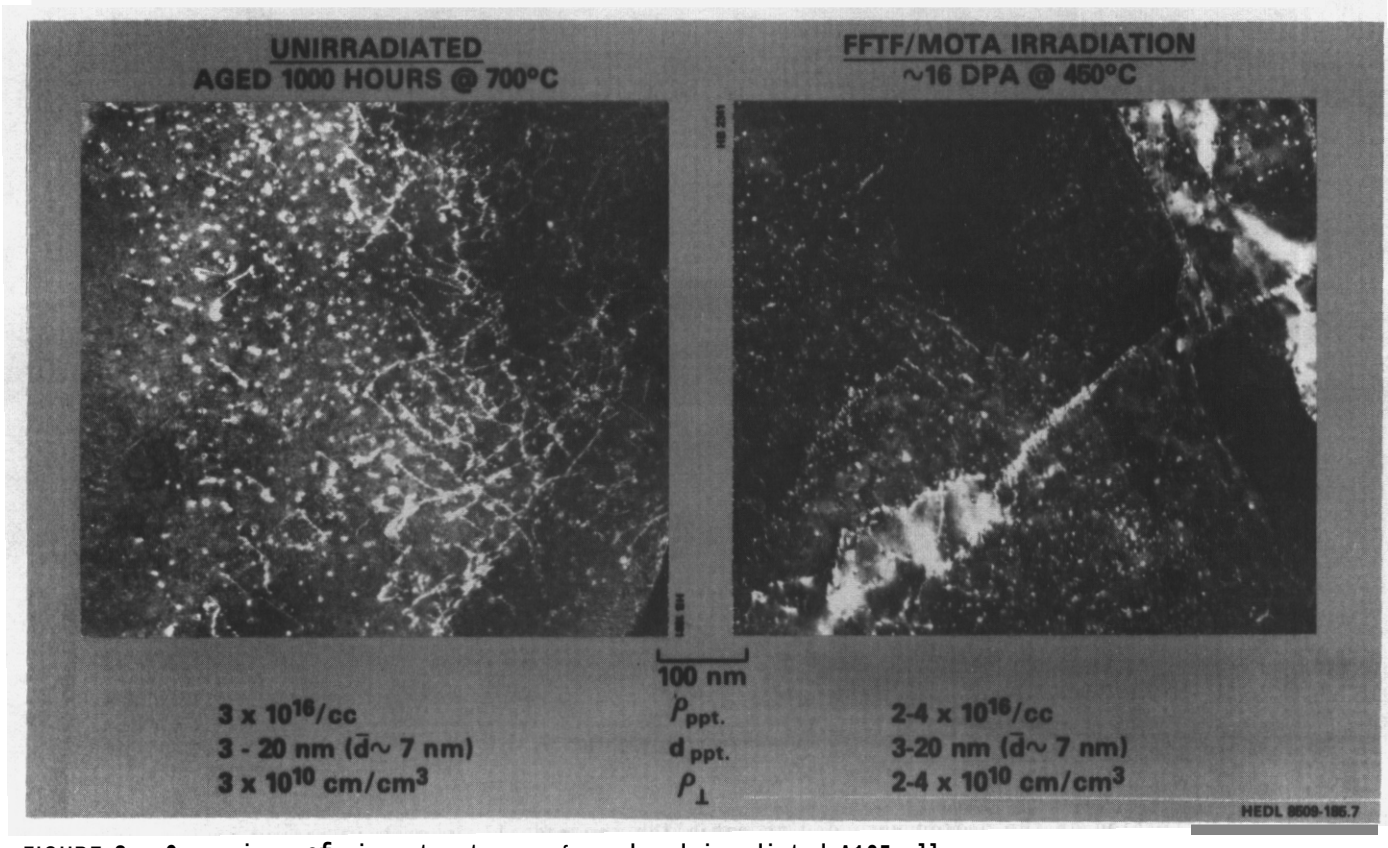

FIGURE 2. Comparison of microstructures of aged and irradiated A125 alloy.

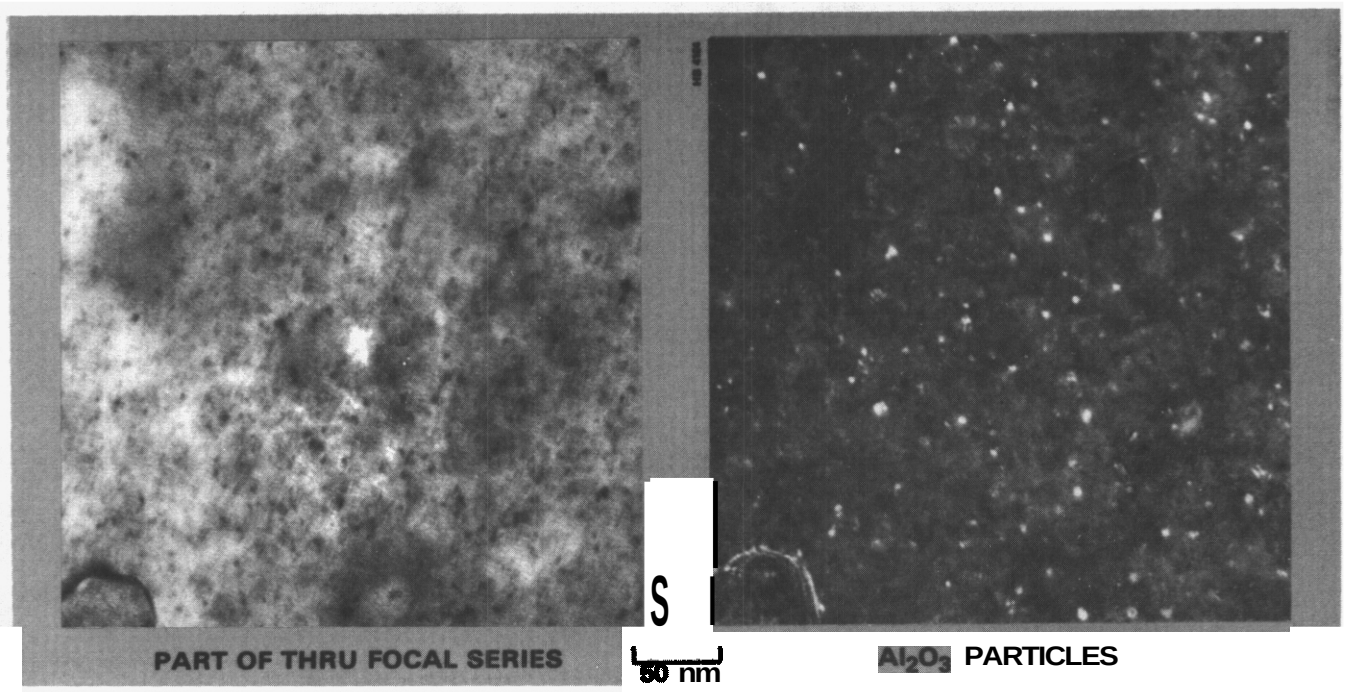

FIGURE 3. Illustration of absence of voids in irradiated A125 during careful thru-focal series of microscopy. Also shown is the fineness and distribution of Al_2O_3 dispersoids.

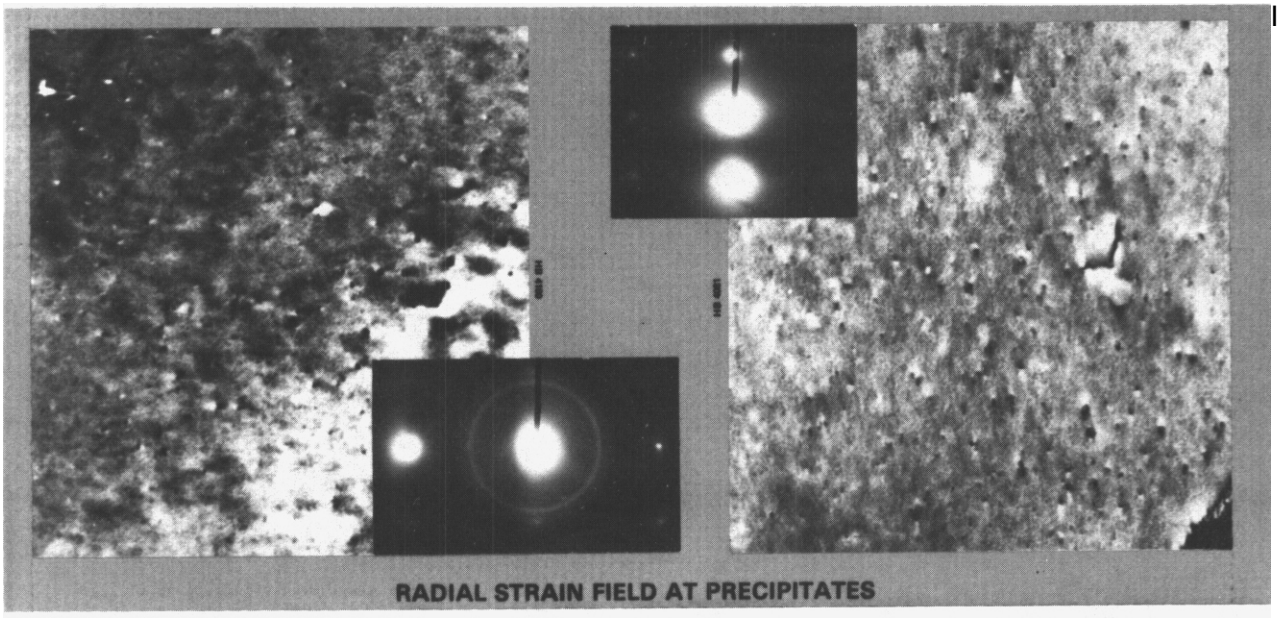

FIGURE 4. Illustration of the procedures used to establish the radially symmetric nature of the dispersoid particles in irradiated A125.

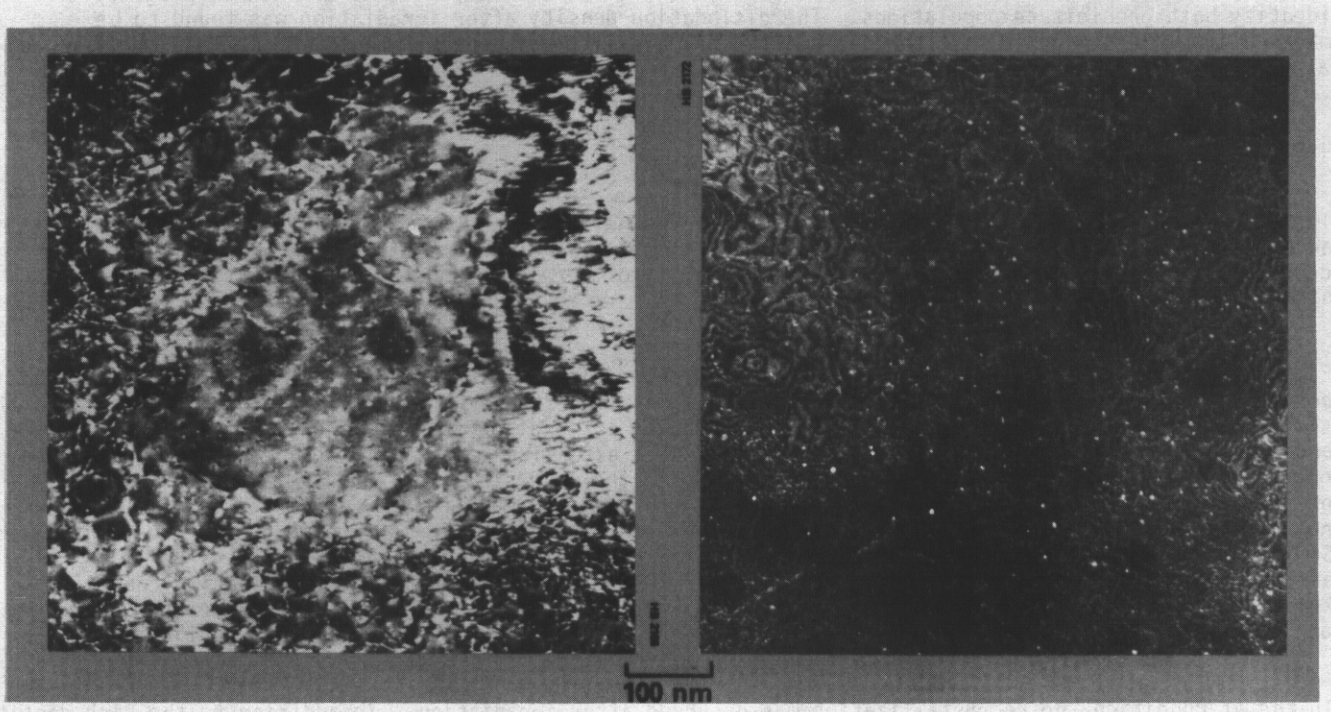

FIGURE 5. Micrographs demonstrating stability of small precipitates in MZC aged 1000 hours at 400°C.

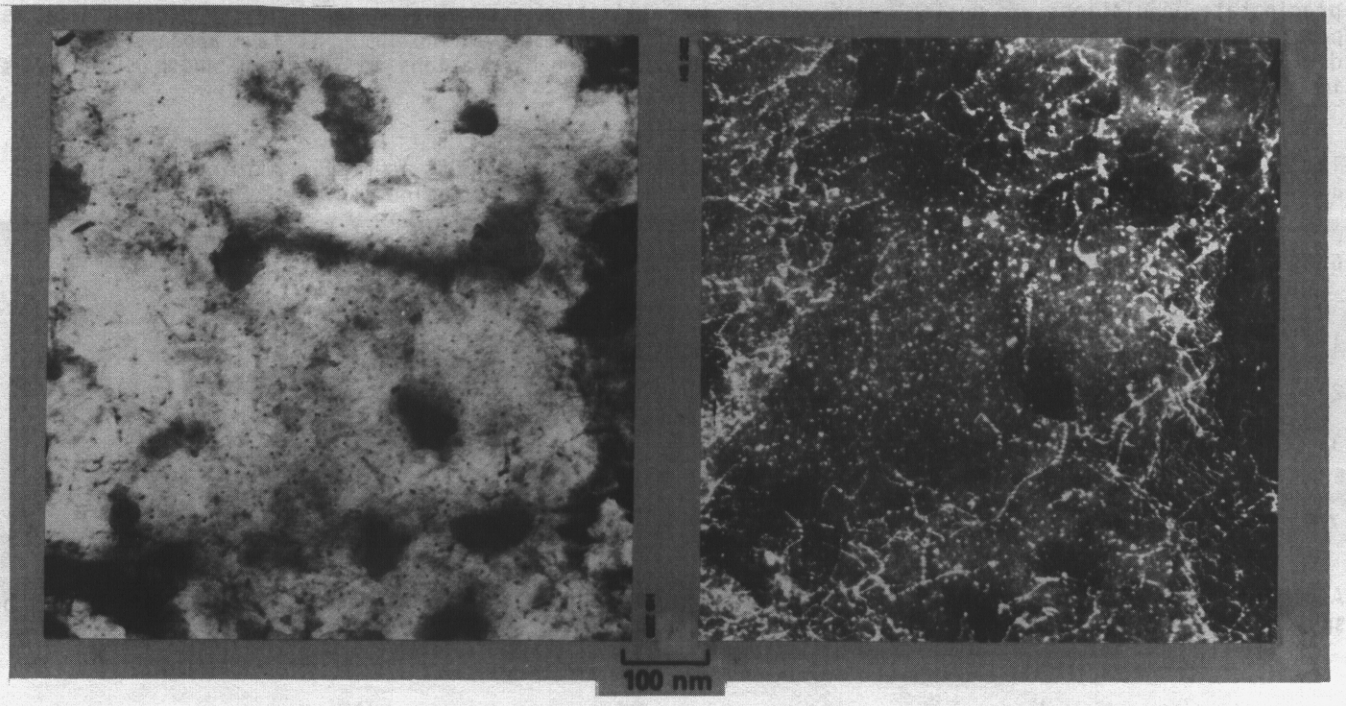

FIGURE 6. Bright-field and dark-field micrographs showing both large and small precipitates found in irradiated MZC.

still exist after irradiation, there is a second population of precipitates at $\sim 10^{14}$ cm^{-3} which have much larger sizes (~50 nm). These were found to be rich in chromium. Experiments are now in progress to identify both precipitate populations. The dislocation density after irradiation was found to be marsinally higher ($\sim 10^{11}$ cm^{-2}) than that of typical austenitic stainless steels (3-6 X 10^{10} cm^{-2}) irradiated at comparable homologous temperatures.

5.5 Precipitation-Strengthened Alloy

The CuBeNi alloy was irradiated in two conditions; the half-hard and tempered (1/2 HT) condition and the annealed and tempered condition (AT). Since beryllium in solution strongly reduces electrical conductivity. nickel is added to reduce the solubility of beryllium and induce precipitation of nickel-beryllium precipitates.

Figures 7 and 8 show that after aging of the 1/2 HT condition for 1000 hours at 400°C that the precipitates are quite stable but after aging at 700°C for the same time extensive recrystallization occurs along with strong coarsening of the precipitate structure. During irradiation at 450°C, however, recrystallization and coarsening also occurs. Figures 9 and 10 show that extensive recrystallization (~75% of grains) has occurred, with large precipitates and voids forming in the recrystallized zones. The unrecrystallized grains are largely free of voids and contain 1.5 X 10^{16} cm^{-2} of small (1.5 nm) precipitates of undetermined nature. There is some evidence that envelopes or halos of voids are formed around the large precipitates. Similar behavior has been observed in other alloys containing boron-rich precipitates.[2,3] It is assumed that these are a consequence of the $^{9}Be(n,2n)B^{8}e \rightarrow {}^{4}He + 4He$ reaction. The reaction energy is known to be broader in energy range and not as well defined as that of typical (n,σ) reactions, however. and the halo's are therefore broader and less distinct than that generated by $(n.\ \sigma)$ reactions.

In the at condition, no recrystallization was observed after irradiation. In addition to the high density of small precipitates there were a very low density ($\sim 10^{12}$ cm^{-3}) of large voids, with sizes comparable to that observed in the pure copper.

5.6 Conclusions

Pure copper swells rather easily at 450°C but swelling can be delayed by solute additions. particularly when dense precipitate populations are introduced which are stable during irradiation. When the precipitate populations are unstable and when recrystallization occurs, then swelling can occur. This is particularly true in alloys which contain beryllium that transmutes to helium. It also appears that density change information must be supplemented by microscopy observations to determine whether decreases in density arise from voids and/or precipitation sequences.

The behavior of MZC and particularly of A125 during irradiation at 450°C is most promising and provides additional incentive for development of high-conductivity alloys for fusion service.

6.0 References

1. H R. Brager. H. L. Heinisch and F. A Garner, J. Nucl. Mater. 133 & 134 (1985) 675.

2. D. S. Gelles and F. A. Garner, J. Nucl. Mater.. 85 & 86 (1979) 689.

3. A Kumar and F. A. Garner. Radiation Effects. 82 (1984) 61.

7.0 Future Work

Additional microscopy will be performed on specimens irradiated at 16 dpa. Density change measurements on specimens irradiated to higher exposures will also be performed.

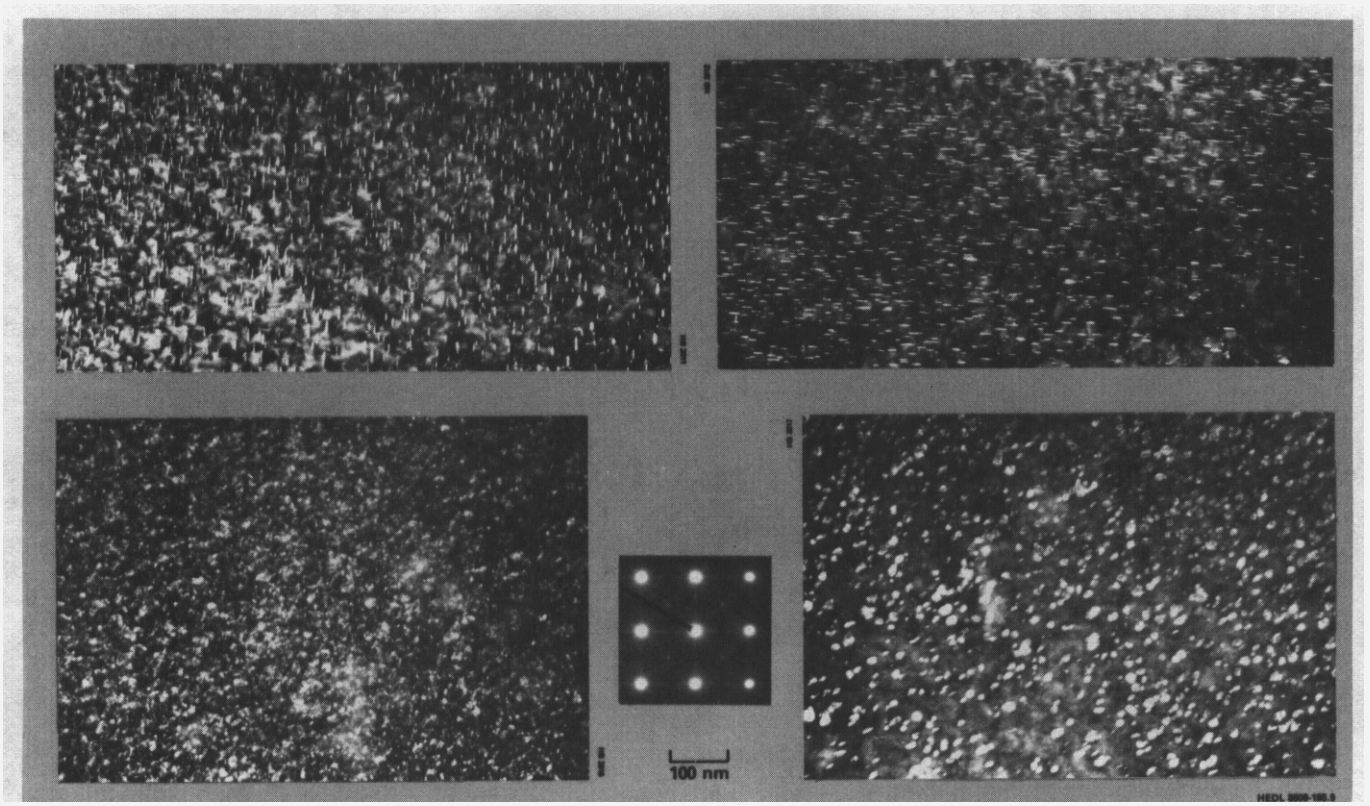

FIGURE 7. High density of small precipitates observed in CuBeNi (1/2 HT) after aging 1000 hours at 400°C, using different diffraction vectors.

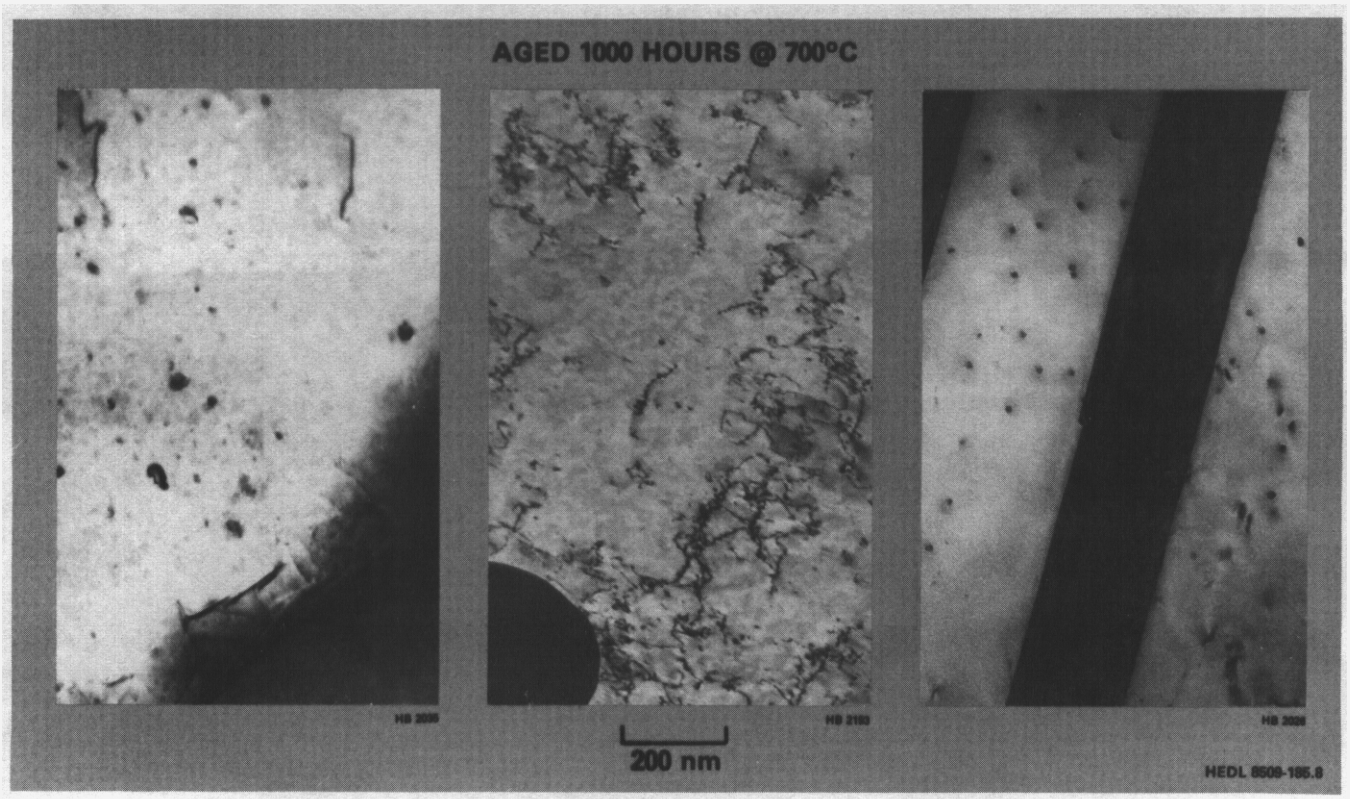

FIGURE 8. Recrystallized microstructures observed in CuBeNi (1/2 HT) after aging 1000 hours at 700°C.

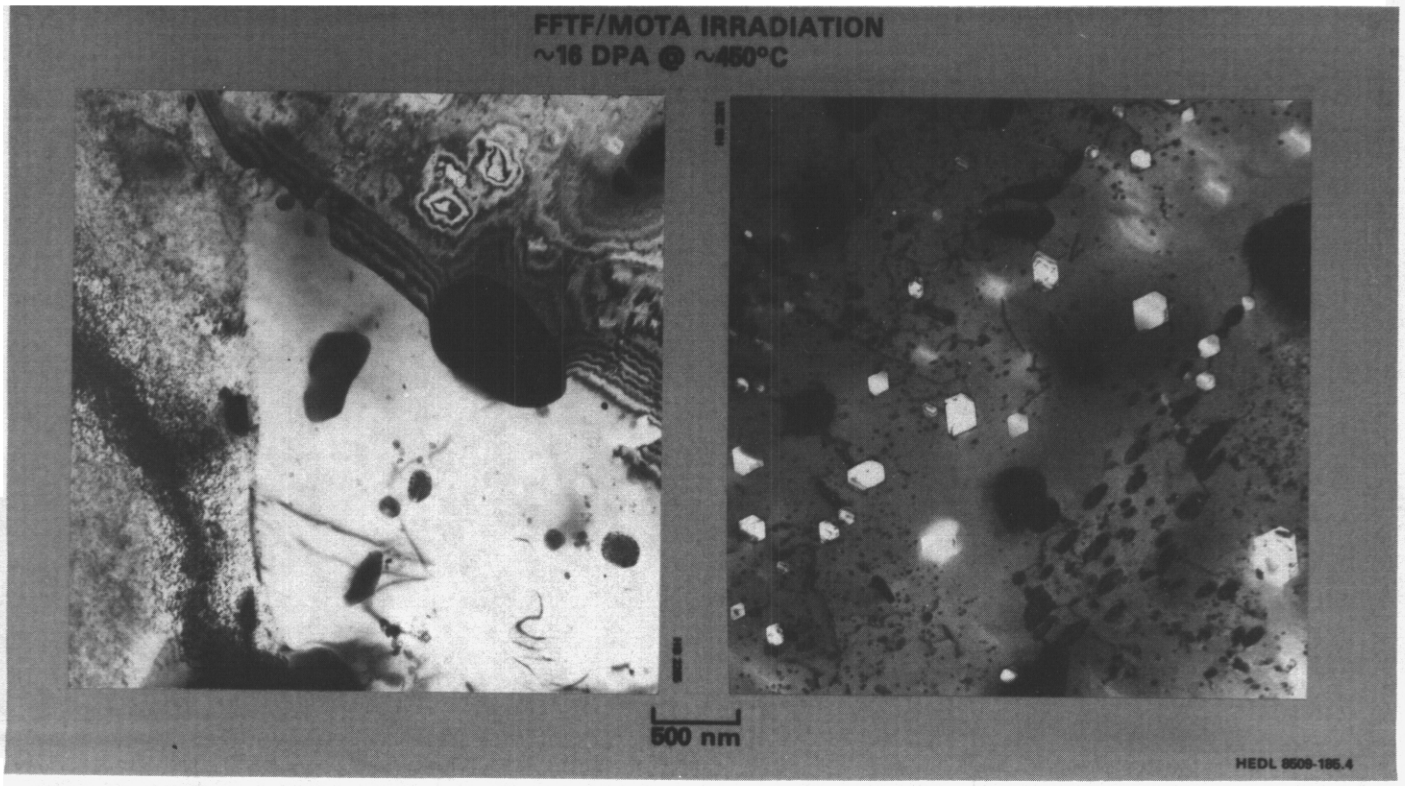

FIGURE 9. Adjacent grains in CuBeNi (1/2 HT) after irradiation, showing both recrystallized and unrecrystallized grains. Large precipitates and voids are found in in recrystallized areas.

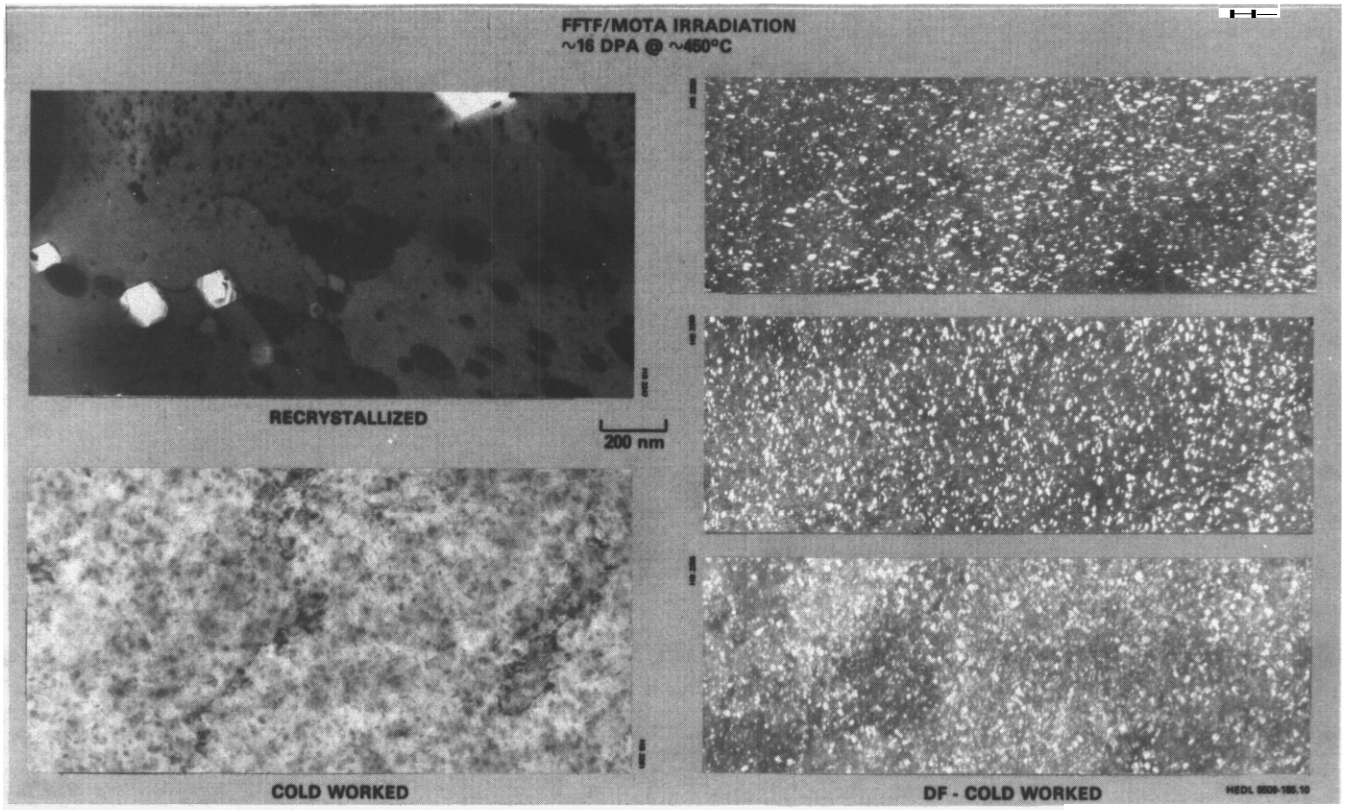

FIGURE 10. While the recrystallized areas of CuBeNi (1/2 HT) exhibit large voids and precipitates, the uncrystallized areas retain their original cold-work character.

EXTERNAL DISTRIBUTION

UC-20 (108), 20c (59)

DOE-HQ/Office of Fusion Energy
ER-62
Washington, DC 20545

SE Parket

DOE-HQ/Office of
International Security Affairs
DP-33, Mail Stop 4C-024
Washington, DC 20585

DW Dorn

Argonne National Laboratory (3)
9700 South Cass Avenue
Argonne, IL 60439

LR Greenwood, CMT-205
A. Taylor, MST-212
BA Loomis, MST-212

Argonne National Laboratory
EBR-II Division
Reactor Materials Section
P.O. Box 2528
Idaho Falls, ID 83403-2528

DL Porter

Battelle
Pacific Northwest Laboratory (2)
P.O. Box 999
Richland, WA 99352

JL Brimhall 306W/210
TD Chikalla PSL/1277

Carnegie-Mellon University
Metallurgical Engineering
3325 Science Hall
Pittsburgh, PA 15213

WM Garrison Jr

Centre d'Etudes de Chimie Metallurgique
15, Rue Georges-Urbain
Vitry-sur-Seine
94400 Vitry, France

G. Martin

Columbia University
School of Engineering & Applied Science
New York, NY 10027

RA Gross

Commission of the European Communities
Rue de la Loi 200
B-1049 Bruxelles, Belgium

J. Darvas

Commission of the European Communities (2)
Joint Research Center
I-21020 Ispra, Varese, Italia

R. Dierckx, Physics Division
P. Schiller, Materials Science Division

Department of the Navy
Naval Research Laboratory (2)
Washington, DC 20375

JA Sprague, Code 6395
LE Steele, Code 6390

Energieonderzoek Centrum Nederland (2)
Netherlands Energy Research Foundation
Westerduinweg 3, Postbus 1
NL-1755 ZG, Petten (NH), The Netherlands

B. vanderSchaaf
W. vanWitzenburg, Materials Dept

GA Technologies Inc (3)
P.O. Box 85608
San Diego, CA 92138

JR Gilleland
GR Hopkins
T. Lechtenberg

General Dynamics/Convair
P.D. Box 85377
San Diego, CA 92138

H. Gurol, MZ 92-1072

General Electric
Advanced Nuclear Technology Operation (2)
310 DeGuign Drive
Sunnyvale, CA 94088

ANTD Library, M/C F-02
S. Vaidyanathan, M/C 5-53

Hahn-Meitner Institiit fur Kernforschung Berlin GmbH
Arbeitsgruppe C2
Glienickerstrasse 100
D-1000 Berlin 39, Federal Republic of Germany

H. Wollenberger

Hokkaido University (2)
Facility of Engineering
Kita-hu, Sapporo, 060 japan

Michio Kiritani, Precision Engineering
Taro Takeyama, Metals Research Institute

Institiit fur Festkoroerforschung der
Kernforschungsanlage Jülich GmbH
Postfach 1913
D-5170 Jiilich 1, Federal Republic of Germany

P. Jung

EXTERNAL DISTRIBUTION (Cont'd)

Japan Atomic Energy Research Institute (2)
Physical Metallurgy Laboratorv
Tokai Research Establishment
Tokai-mura, Naka-gun, Ibaraki-ken, 319-11 Japan

Tadao Iwata, Physics
Kensuke Shiraishi, Fuels Materials Research

Kernforschungszentrum Karlsruhe GmbH
Institüt fur Material und Festkorperforschung II
Postfach 3640
0-7500 Karlsruhe 1, Federal Republic of Germany

K. Ehrlich

Kyushu University
Research Institute for Applied Mechanics
6 Kasuga-Koen, Kasuga-shi
Fukuoka, 816 Japan

Kazunori Kitajima

Lawrence Livermore National Laboratory *(2)*
P.O. Box 808
Livermore, CA 94550

MW Guinan, L-396
DW Heikkinen, L-397

Lawrence Livermore National Laboratory
P.O. Box 5511
Livermore, CA 94550

EC Oalder, L-643

Los Alamos National Laboratory
P.O. Box 1663
Los Alamos, NM 87544

DJ Oudziak, S-41F611

Massachusetts Institute of Technology *(2)*
77 Massachusetts Avenue
Cambridge, MA 02139

I-Wei Chen, 13-5118
NJ Grant, 8-407

Massachusetts Institute of Technology
Nuclear Reactor Laboratory
138 Albany St
Cambridge, MA 02139

OK Harling, NW12-204

Max-Planck-Institut fur Plasma Physik (2)
The NET Team, IPP/NET
D-8046 Garching bei München,
Federal Republic of Germany

DR Harries
R. Toschi

McDonnell-Douglas Astronautics Co
P.O. Box 516
St. Louis, MO 63166

JW Davis

Nagoya University
Institute of Plasma Phvsics
Furo-chyo, Chikusa-ku,
Nagoya, 464 Japan

Taijiro Uchida

National Research Institute for Metals
Tsukuba Laboratories
1-2-1 Sengen, Sakura-mura,
Nihari-gun, Ibaraki, 305 Japan

H. Shiraishi

North Carolina State University
Box 7907
Materials Engineering Department
Raleigh, NC 27695-7907

JR Beeler Jr

Oak Ridge National Laboratory (7)
P.O. BOX X
Oak Ridge, TN 37831

ML Grossbeck
MCG Hall
LK Mansur
PJ Maziasz
NH Packan
RE Stoller
SJ Zinkle

Oak Ridge National L a b o r - *(2)*
P.O. BOX Y
Oak Ridge, TN 37831

LA Berry
RW Wiffen, FEOC Bldg

Osaka University
2-1 Yamada-oka, Suita,
Osaka, 565 Japan

Kenji Sumita, Nuclear Engineering

Osaka University
8-1 Mihogaoka
Ibaraki, Osaka, 567 Japan

Toichi Okada, Institute of
Scientific & Industrial Research

Pacific Sierra Research Corp
1104B Camino Del Mar
Del Mar, CA 92014

RO Stevenson

EXTERNAL DISTRIBUTION (Cont'd)

Princeton University (2)
Plasma Physics Laboratory
Forrestal Campus
P.O. Box 451
Princeton, NJ 08544

JPF Conrads
Long-poe Ku

Rism National Laboratory
Postfach 49
OK-4000 Roskilde, Denmark

BN Singh

Rockwell International Corp
Rocketdyne Division
6633 Canoga Avenue
Canoga Park, CA 91304

DW Kneff, NA02

Sandia National Laboratories
Livermore, CA 94550

WG Wolfer

Science University of Tokyo
Faculty of Engineering
Kagurazaka, Shinjuku-ku,
Tokyo, 162 Japan

RR Hasiguti

Studiecentrum voor Kernenergie
Centre d'Etude de l'Energie Nucleaire
Boeretang 200
B-2400 Mol, Belgium

J. Nihoul

Swiss Federal Institute
for Reactor Research (2)
CH-5303 Würenlingen, Switzerland

WV Green
M. Victoria

Tohoku University (2)
Research Institute for Iron,
Steel and Other Metals
2-1-1 Katahira, Sendai, 980 Japan

Katunori Abe
Hideki Matsui

Tokyo Institute of Technology
Research Laboratory for Nuclear Reactors
12-1, 2-chome, O-Okayama
Meguro-ku, Tokyo, 152 Japan

Kazutaka Kawamura

United Kingdom Atomic Energy Authority
Atomic Energy Research Establishment (2)
Oxfordshire OX11 ORA, UK

R. Bullough, Theoretical Physics

United Kingdom Atomic Energy Authority
Culham Laboratory
Applied Physics & Technology Division
Abingdon, Oxfordshire OX14 3DB, UK

GJ Butterworth

University of California (2)
School of Engineering and Applied Science
Boelter Hall
Los Angeles, CA 90024

RW Conn, KL-98
NM Ghoniem, KH-01

University of Michigan
Nuclear Engineering
Ann Arbor, MI 48109

T. Kammash

University of Missouri
Dept of Nuclear Engineering
Rolla, MO 65401

A. Kumar

University of Tokyo (3)
3-1, Hongo 7-chome,
Bunkyo-ku, Tokyo, 113 Japan

Naohira Igata, Met & Materials Science
Shiori Ishino, Nuclear Engineering
Shuichi Iwata, Nuclear Engineering

University of Virginia
Dept of Materials Science
Thornton Hall
Charlottesville. VA 22901

WA Jesser

Westinghouse
Advanced Energy Systems Division
Fuels Materials Technology
P.D. Box 10864
Pittsburgh, PA 15236

A Boltax, Manager

Westinghouse
Research and Development Center
1310 Beulah Road
Pittsburgh, PA 15235

JA Spitznagel

INTERNAL DISTRIBUTION

DOE-RL/AMF
Site & Laboratory Management Division (SMD)
Laboratory Management & Technology
Services Branch
FED/210-B

KR Absher, Chief

HEDL (26)

HR Brager	W/A-58	C. Martinez	W/A-58
LL Carter	W/B-47	WN McElroy	W/C-39
DG Doran (5)	W/A-57	EK Opperman	W/A-58
FA Garner	W/A-58	RW Powell	W/A-58
DS Gelles	W/A-58	RJ Puigh	W/A-58
R. Gold	W/C-39	FA Schrnittroth	WIA-58
HL Heinisch	W/A-58	VF Sheely	W/C-20
DL Johnson	W/B-41	RL Simons	W/A-65
GD Johnson	W/A-65	HH Yoshikawa/MJ Korenko	W/C-44
NE Kenny	W/C-115	Central Files	W/C-110
RM Mann	W/A-58	Documentation Services	W/C-123